RSC Advances

REVIEW

View Article Online
View Journal | View Issue

Cite this: *RSC Adv.*, 2025, **15**, 43446

Advances in perovskite-based scintillation materials for gamma-ray spectroscopy: issues and opportunities

Md. Helal Miah, [ab] Mayeen Uddin Khandaker, [*acd] Phannee Saengkaew, [e] Arshid Numan[f] and Mohammad Aminul Islam[gh]

The accurate detection of radiation is crucial for assessing health risks, ensuring safety, and optimizing its use in various fields including medicine, industry, security, space exploration, and scientific research. As part of the exploration of novel detectors, this review considers the recent progress in halide perovskite scintillators derived from alkali and alkaline earth metal halides, covering high-to low-dimensional configurations. This review begins with the key figures of merit for scintillation and physics of radiation detection, followed by crystal growth techniques. Moreover, it provides a comprehensive overview of various energy ranges in gamma-ray spectroscopy research, emphasizing strategies including dimensional tuning, compositional engineering and use of activators to enhance the scintillator performance. This study reveals that low-dimensional perovskite scintillators generally outperform their higher-dimensional counterparts. Notably, 2D $CsBa_2I_5$:4% Eu demonstrated exceptional results with a light yield (LY) of 198 000 photons per MeV and an energy resolution (ER) of 1.8% at 1332 keV, which are much better than the values obtained for conventional scintillators. In addition, fine-tuning of the composition in the host structure and incorporating suitable dopants significantly contribute to improving the performance of scintillators. Finally, this investigation identifies certain limitations such as the challenges in crystal growth, limited structural and dopant variety, underreported stability and radiation hardness, and a predominant focus on specific gamma energies, particularly 662 keV. In addition, despite the long decay times of some scintillators, research has yet to fully utilize this advantageous property in imaging systems. Moreover, standardized testing protocols are essential to ensure the authentication of their performance all over the world. Future research should focus on addressing existing challenges to ease the transition of perovskite-based scintillators from laboratory to commercial use.

Received 15th July 2025
Accepted 3rd October 2025

DOI: 10.1039/d5ra04980f

rsc.li/rsc-advances

1. Introduction

In November 1895, a significant discovery was made by Wilhelm Conrad Roentgen when he noticed the glow of a barium platino-cyanide screen located next to his operating discharge tube.[1] This led to the discovery of a new form of invisible and penetrating radiation, which came to be known as X-ray or 'Roentgen radiation', with barium platino-cyanide regarded as the first radiation detector by the scientific community.[1,2] Following his discovery of radioactivity, Becquerel looked for methods to quantify and monitor the radiation emitted by radioactive materials.[3] A photographic plate was one of the first tools used to record any type of information from radioactivity. However, the high energy radiation (X-rays and γ-rays) registration process revealed that a basic photographic film was quite ineffective, prompting an immediate exploration for materials capable of converting high energy radiations into visible light to enhance their compatibility with sensitive photographic film-based detectors.[4] Pupin introduced a $CaWO_4$ powder, which

[a]*Applied Physics and Radiation Technologies Group, CCDCU, Faculty of Engineering and Technology, Sunway University, 47500 Bandar Sunway, Selangor, Malaysia. E-mail: mayeenk@diu.edu.bd; mu_khandaker@yahoo.com*

[b]*Department of Physics, Gopalganj Science and Technology University, Gopalganj-8100, Bangladesh*

[c]*Faculty of Graduate Studies, Daffodil International University, Daffodil Smart City, Birulia, Savar, Dhaka-1216, Bangladesh*

[d]*Department of Physics, College of Science, Korea University, 145 Anam-ro, Seongbuk-gu, Seoul, 02841, Republic of Korea*

[e]*Department of Nuclear Engineering, Faculty of Engineering, Chulalongkorn University, Bangkok 10330, Thailand*

[f]*Sunway Centre for Electrochemical Energy and Sustainable Technology, Faculty of Engineering and Technology, Sunway University, 47500 Bandar Sunway, Selangor, Malaysia*

[g]*Miyan Research Institute, International University of Business Agriculture and Technology, Dhaka, 1230, Bangladesh*

[h]*Department of Electrical Engineering, Faculty of Engineering, Universiti Malaya, Jalan Universiti, 50603 Kuala Lumpur, Selangor, Malaysia*

served this purpose for over 75 years.[5] Alongside the ZnS-based powders introduced a few years later, the $CaWO_4$ powder represents the most surviving material utilized for high energy radiation detection.[4] In 1897, Braun invented the cathode ray tube, a device that converts the energy of an accelerated electron beam into visible light through a phosphor material, which was also a fascinating development in technology.[6,7] The process of this transformation of particle energy into visible light is notably akin to that observed in the scenario of X-rays or γ-rays conversion. At the end of the nineteenth century, two dynamic types of radiation including photons and particles have emerged, and their vast potential for application significantly propelled the advancement of phosphor and scintillator materials for their utilization. Along with the development of scintillator materials, the scientific community has placed emphasis on counting the converted visible photons. During World War II, Samuel Curran and W. Baker developed the first electronic scintillation counter as part of the Manhattan Project.[8] They utilized an RCA Type 1P21 photomultiplier tube to capture the scintillations induced by alpha particles striking on a silver-activated ZnS screen. The credit for the first electronic alpha scintillation detector is sometimes given to Marietta Blau and B. Dreyfus (1945) or John Coltman and Hugh Marshall (1947) due to the delay in publication of the Manhattan Project.[2]

In addition, Blau and Dreyfus measured the intensity of alpha radiation using PMT current, whereas Coltman and Marshall recorded pulses.[14,15] Ruby Sherr made the first use of a PMT in an alpha survey meter in 1947.[16] It is impossible to say enough about how important the photomultiplier tube was. It was necessary for many of the scientific methods we use today, such as gamma scintillation spectroscopy, liquid scintillation counting, and thermo-luminescent dosimetry. The advent of the photomultiplier tube catalyzed the emergence of an extensive array of scintillating materials including naphthalene, anthracene, stilbene phenanthrene, NaI, CaF, KI, fluoranthene, fluorine, $CaWO_4$, and $CdWO_4$. The chronological history of the research and development of various scintillators is listed in Fig. 1. These scintillators are classified as organic scintillators, inorganic scintillators, and composite scintillators. The latter is produced by combining organic and inorganic materials to harness the advantages of both and produce synergistic effects. Although organic scintillators offer advantages such as chemical versatility, ease of modification and cost-effectiveness, it has a lot of issues including non-linearity of light output, dependence of LY on gas pressure and magnetic field, decrease in LY with time, and vulnerability to foreign elements and radiation damage.[17–20] To overcome the limitations of organic scintillators, the scientific community has adopted inorganic scintillators owing to their high stopping power, hardness to high energy, relatively high LYs and fast response times.[21] The most used inorganic scintillator is thallium-doped sodium iodide (NaI:Tl) due to its high LY and efficiency in detecting gamma rays and X-rays.[22,23] In addition, cesium iodide (CsI:Tl or Na) is often used in medical imaging and high-energy physics experiments due to its improved scintillation properties.[24,25] Moreover, bismuth germanate (BGO) is also known for its high density and effective atomic number and is used in positron emission tomography.[26–28] Furthermore, zinc sulfide (ZnS) is commonly used in alpha particle detection and in some neutron detectors.[29,30] Finally, gadolinium oxysulfide (Gd_2O_2S) is employed in X-ray imaging and computed tomography scanners.[31,32] Despite being widely used, classic inorganic scintillators have a number of drawbacks that limit their practical applications. For instance, some have low LY (such as $CdWO_4$), others have significant afterglow (such as CsI:Tl), and many are hygroscopic (such as NaI:Tl). Additionally, although semiconductor detectors have a higher energy resolution (ER) than scintillation-based detectors, they are quite expensive.[33] This emphasizes how important it is to develop or explore new materials with better scintillation qualities to replace conventional materials for ionizing radiation detection.

The application of perovskite materials for ionizing radiation spectroscopy with the scintillation technique has been investigated because of their advantageous properties including high average atomic number, tunable bandgaps, high density, significant LY, and fast response time.[10,34] However, the best scintillator detector with a perovskite material can distinguish between two gamma-ray peaks that are separated by 15.226 keV at 662 keV,[35] while HPGe exhibits 1.8 keV at the same energy of 662 keV.[36] Thus, it is imperative to focus on tailoring the chemical composition, doping elements, and crystal structure of perovskites to enhance their performance for ionizing radiation sensing.

According to the research and development of scintillation, alkali halides and alkaline earth metal halides have demonstrated excellent performances in gamma-ray spectroscopy as commercial scintillators namely CsI, NaI, and SrI_2. When combined in stoichiometric ratios, these halides form perovskite structures that can integrate the advantageous properties of both compounds. The objective of this review is to present the recent progress in halide perovskite scintillators, which encompasses a variety of structural configurations ranging from higher-to lower-dimensional frameworks. Additionally, this study explores key figures of merits for scintillation performance, fundamental principles of radiation detection, and techniques for synthesizing high-quality single crystals. Moreover, a comprehensive overview of gamma-ray spectroscopy research is provided, highlighting the strategies and approaches employed to enhance the performance of scintillators. Furthermore, the comparative performance of perovskites with varying dimensionalities, as well as with conventional commercial scintillators, is discussed. Finally, this review addresses the current drawbacks in the development of perovskite-based detectors for gamma-ray spectroscopy and outlines potential directions for future research. The essence of our investigation is depicted in Fig. 2.

2. Material and structural layout

In 1839, German mineralogist Gustav Rose identified $CaTiO_3$, which he named perovskite in honor of Russian mineralogist Count Lev Alekseyevich von Perovski.[37] Over time, any compound following the stoichiometric ratio of ABX_3 came to

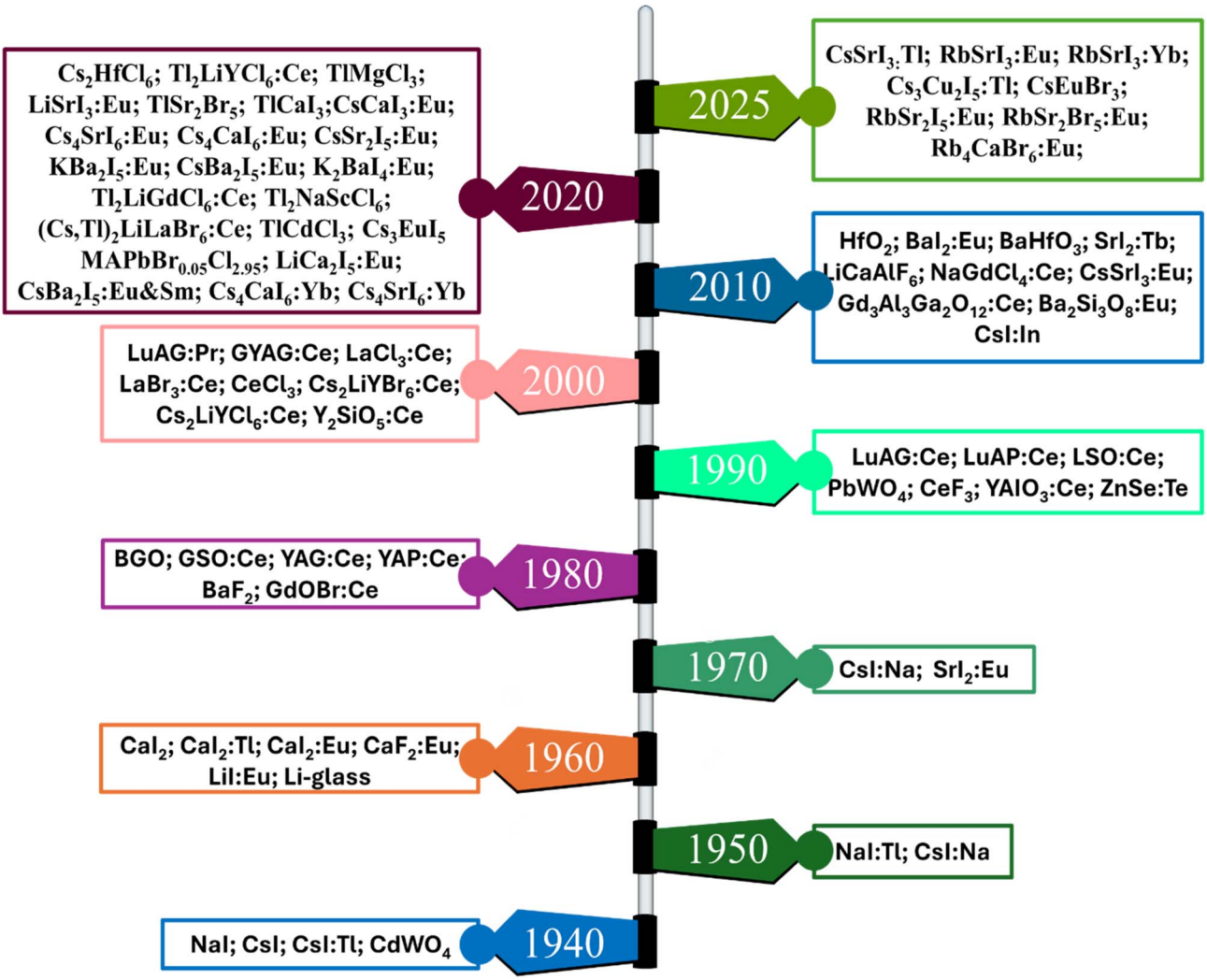

Fig. 1 Timeline of the discovery of various scintillators.[4,9–13]

be known as a perovskite. In this formula, the symbol A recommends a monovalent inorganic/organic cation/mixed of both cations, B represents a divalent cation, and X generally implies a halide anion.[38] Additionally, multiple cations and anions with different valences can be incorporated into the ABX_3 formula. For example, chalcogenides, nitrogen, oxygen, or carbon can be placed at the X-site to develop ABX_3 perovskites, where the valences of the A and B cations are adjusted accordingly to attain charge neutrality. Structurally, cubic perovskites are composed of corner-sharing BX_6^{4-} octahedra that form a 3D network, with the A-site cations occupying 12-fold coordinated cuboctahedral voids to preserve charge balance.[39,40] Additionally, perovskite materials can be viewed as a cubic close-packed AX_3 sublattice, with divalent B-site cations located within six-fold coordinated octahedral sites. Besides the cubic phase, perovskites can also exist in the form of tetragonal and orthorhombic phases.

Moreover, by carefully picking and coordinating the components in organometal halide perovskites, materials with different dimensionalities including three-dimensional (3D), two-dimensional (2D), one-dimensional (1D), and zero-dimensional (0D), can be attained. These classifications are based on the connectivity and spatial arrangement of the metal halide octahedra within the crystal structure.[41]

2D organometal halide perovskites can be observed as layers or sheets derived from 3D perovskite structures by slicing along specific crystallographic directions.[42] When one or more layers of corner-sharing metal halide octahedra are separated by bulky cations, the resulting structures are known as Ruddlesden–Popper-type perovskites.[41] In addition, in 1D perovskites, the metal halide octahedra attach through corner-sharing, edge-sharing, or face-sharing configurations to form continuous 1D chains or nanowires. These inorganic chains are typically isolated by surrounding bulky cations.[41] Moreover, in 0D perovskites, individual metal halide octahedra are surrounded and isolated by bulky cations.[43]

The Goldschmidt tolerance factor (GTF) is sometimes used to predict the potential of perovskites for photovoltaic applications, though it has seen limited application in the development of scintillators. The GTF is a dimensionless quantity that

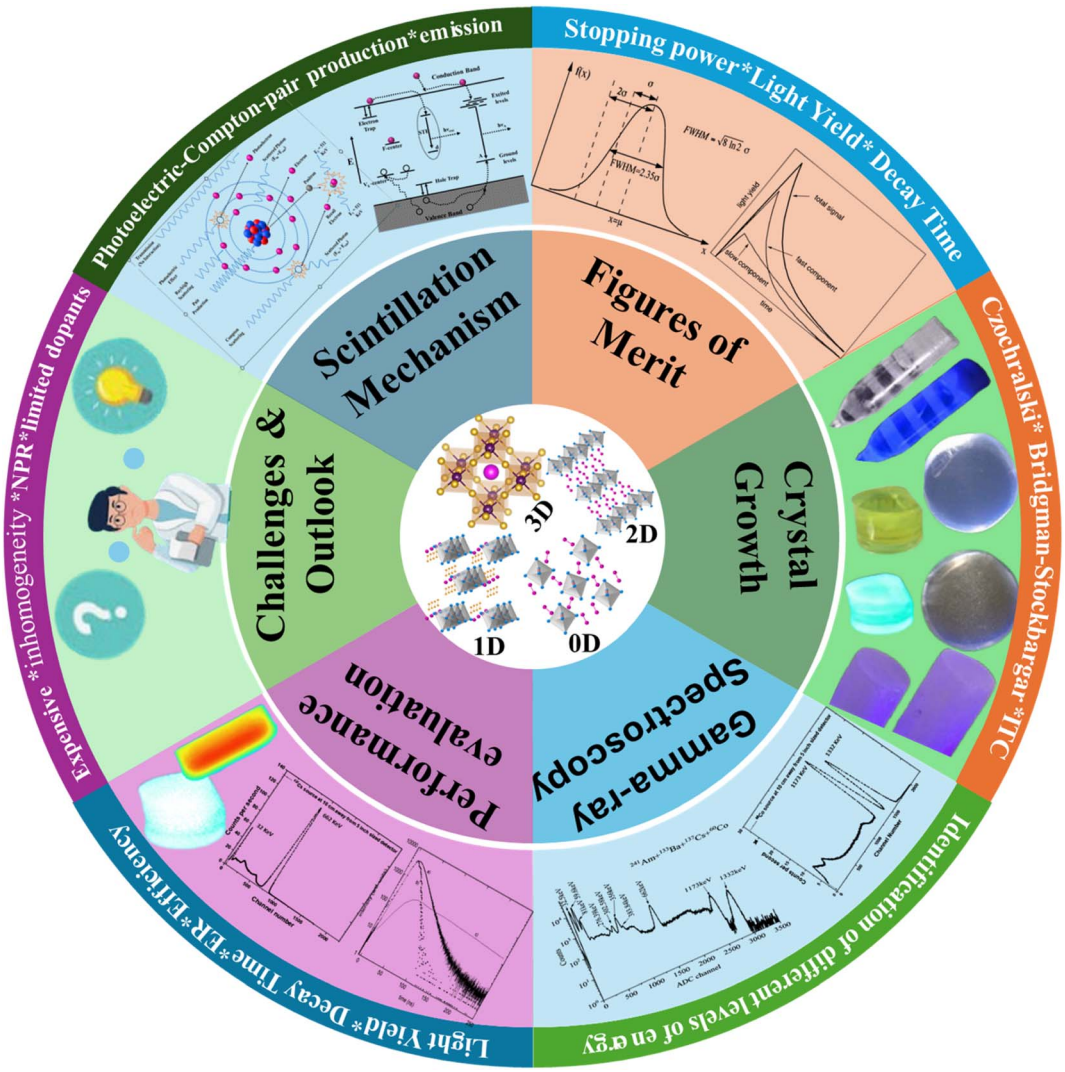

Fig. 2 Brief essence of this review.

is employed to predict the geometrical distortion and phase stability of perovskite compounds based on the ionic sizes of the atoms in ABX_3. It is expressed by $t = (R_A + R_X)/2(R_X + R_B)$, where R_A, R_B and R_X correspond to the ionic radius of the A, B, and X atoms in ABX_3 or mixed perovskite, respectively. For a stable 3D perovskite, this value should be between 0.80 and 1.0.[44] The GTF of a given ABX_3 structure not only acts as an indicator for evaluating its likelihood to be a 3D formation but also assists as a projecting tool for defining whether it will display an ideal cubic phase ($t \approx 1$) or transition to tetragonal phases ($0.9 < t < 1.0$) or to an orthorhombic phase ($0.8 < t < 0.9$).[45] In addition, GTF values below 0.8 or above 1.0 tend to lead to non-photovoltaic perovskites.[46]

Another important parameter, known as the octahedral factor (μ), evaluates the ability to form BX_6^{4-} octahedra and the stability of perovskite compounds. This factor is determined by the ratio of R_B and R_X. For the formation of stable BX_6^{4-} octahedra, μ should lie within the range of $0.414 < \mu < 0.732$.[47] Maintaining a 3D structure is crucial to facilitating charge transport throughout the system, which in turn ensures the efficient accumulation of photo-generated charges.[48] In devices with semiconductors such as perovskite solar cells, the cubic phase of the material and a lower band gap are highly desirable for efficient charge carrier extraction and transport. A lower band gap enables better absorption of light, while the cubic phase contributes to the isotropic charge mobility, which enhances the overall performance. However, in the case of scintillators, materials with relatively higher band gaps are often preferred to facilitate efficient energy transfer between the host material and the activators (dopants). This higher band gap ensures that the energy levels of the activators align properly within the host, allowing efficient recombination processes that generate scintillation light. Additionally, the cubic phase of the material in scintillators is crucial because it supports fast and isotropic charge generation and recombination, contributing to a higher LY and faster response and decay times, which are key for high-performance radiation detection applications. Therefore, although both solar cells and scintillators benefit

from the cubic phase structure, the optimal band gap for each application varies based on the functional requirements. Schematic diagrams of the various dimensional configurations are depicted in Fig. 3.

3. Required properties of materials to be used as scintillators

This section delves into the detailed material characteristics and their influence on performance. The material properties explored include high stopping power, LY, afterglow, non-proportionality, emission spectrum, refractive index, ER, and radiation hardness. These intrinsic properties of the materials directly shape the behavior and effectiveness of the devices. This analysis focuses solely on understanding how these material properties impact the overall device functionality and performance.

3.1. Stopping power

The stopping power of a material represents the energy loss of an incident particle per unit distance as it travels through the material. The attenuation formula is used to predict the radiation stopping ability, as follows in eqn (1).[49–51]

$$I = I_o e^{[-\mu x]} \quad (1)$$

where μ and x represent the linear attenuation coefficient, and thickness, respectively.

The attenuation of incident radiation occurs due to the interaction of incident radiation with materials through mainly the photoelectric effect (PE), Compton effect (CE), pair production (PP) processes, *etc.* The cross-section of interaction for these three phenomena largely depends on the atomic number of the constituent atoms of the substance. In addition, the cross-section, $\sigma_{PE} \propto Z^{3to5}$, $\sigma_{CE} \propto Z$, and $\sigma_{PP} \propto Z^3$ are estimated for PE, CE and PP, respectively.[52,53]

The linear attenuation coefficient in inverse length units can be expressed as follows in eqn (2).[54]

$$\mu\alpha\frac{\rho Z^n}{AE^3} \quad (2)$$

where Z indicates the atomic number of the material, A specifies the atomic mass, and E represents the energy of the incident radiation. However, depending on interaction methods such as photo-electric effect, Compton scattering and pair production, the value of n will change. As the energy increases, the dependence of the attenuation coefficient on atomic number becomes less pronounced, reflecting the variations in cross-sections for these interactions. Therefore, although the attenuation coefficient strongly correlates with atomic number for low-energy photons, the dependence weakens with an increase in energy due to the changing dominance of different interactions. Thus, the radiation blocking ability or stopping power of a material is directly proportional to ρZ_{eff}^{n}, where the power of the effective atomic number will change based on the interaction mechanism.[10,34] Different research estimated a high atomic number and moderate density for perovskite, making it a promising candidate for radiation detection.[50,55]

3.2. Light yield

The light yield is a key performance metric for scintillators. It is defined as the number of photons emitted per unit of energy through the process of scintillation.[56]

$$N_{ph} = \frac{E}{\beta E_{gap}} \times S \times Q \quad (3)$$

where E is the energy of the incident X-ray photons, E_{gap} represents the band gap of the scintillator, S stands for the transmission efficiency of electron–hole pair energy to the luminescent center, and Q refers to the quantum yield. Parameter $\beta = \frac{E_{eh}}{E_{gap}}$ and E_{eh} = energy required to generate one electron–hole pair. The luminescence efficiency Q plays a dominant role in scintillation; however, the LY of scintillators does not always directly correlate with Q, as it reflects only the luminescence efficiency. The efficiency of electron–hole pair transport to the optical emission centers is also critical in determining LY.[57]

In practical applications, the actual LY is often diminished due to factors such as self-absorption, non-radiative recombination caused by defects, and suboptimal light extraction efficiency. Some effective measures to enhance the light extraction,

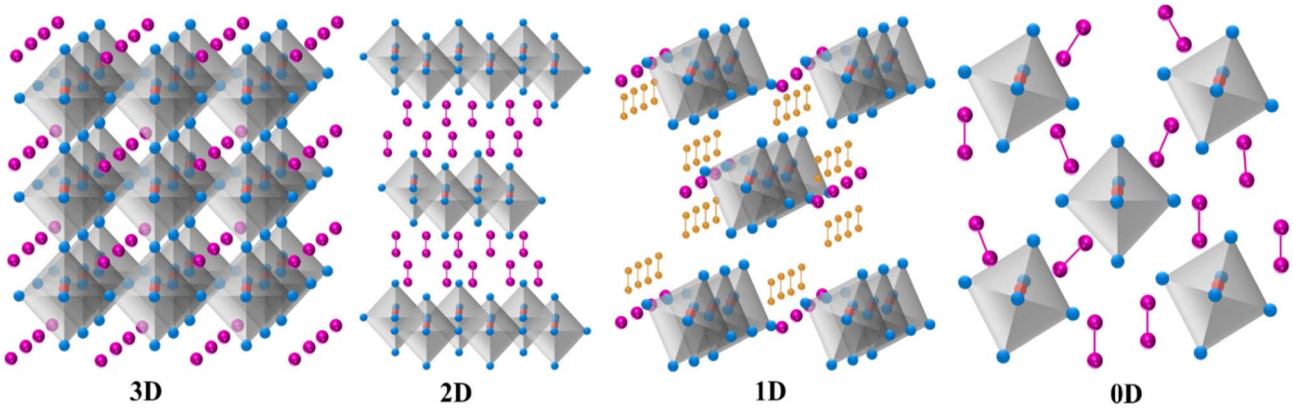

Fig. 3 Schematic diagram of the perovskite structures of various dimensions.

and thus improve the performance of scintillators include applying reflective coatings to minimize light loss, using single crystals with low defect concentrations, and incorporating optical coupling agents between the scintillator and photodiode to optimize light transfer.[58,59] These approaches help to accumulate more light, leading to improved performances. Given that the band gap of perovskite materials is lower than that of commercially available scintillators (BGO: 5 eV, NaI: 5.9 eV and CsI: 6.4 eV), the theoretical LY of perovskite-based scintillators can reach up to 129 000–250000 photons per MeV; however, no perovskite has yet to achieve this level of LY.[60,61] In addition, a few strategies including modulation of the exciton confinement effect, minimization of self-absorption in perovskite, constructing energy-transfer channels, and defect modification can enhance the LY of perovskite-based scintillators.

3.2.1 Modulation of the exciton confinement effect. In semiconductor materials, an exciton, sometimes called a quasiparticle, represents a bound state of an electron and a hole, held together by electrostatic (Coulombic) attraction. An exciton has a finite lifetime; hence, when the electron and hole eventually recombine (the electron falls back into the hole), the energy is typically released in the form of a photon (UV/visible photons) or as heat (non-radiative recombination). The emission of light is primarily dependent on excitonic recombination. Therefore, the LY of scintillators is substantially determined by the parameters of excitons, such as their binding energy (energy required to break apart excitons into free electrons and holes). Materials with low exciton binding energies can indeed dissociate excitons more easily into free charge carriers, which may enhance the LY if the material relies primarily on free charge recombination. However, in the case of perovskite-based scintillators, the situation is slightly different because excitonic recombination is the primary mechanism of light emission. In perovskite-based scintillators, a low exciton binding energy can lead to significant thermal dissociation of excitons at room temperature, resulting in a lower LY because excitons are less likely to survive long enough to recombine radiatively and produce photons. Therefore, in the case of perovskite-based scintillators specifically, increasing the exciton binding energy can indeed improve LY, given that this helps to stabilize excitons at room temperature and enables them to recombine radiatively rather than thermally dissociate. Bulk 3D halide perovskite-based scintillators exhibited very low LY of 1000 photons per MeV at room temperature because of their low exciton binding near to a few tens of meV, indicating loosely bound exciton states and strong thermal dissociation of excitons.[61,62] Techniques such as reducing the dimensionality materials or altering their structural distortions can help increase the exciton binding energy, thereby increasing the likelihood of radiative recombination and enhancing the photon output.[63]

3.2.1.1. Enhancement of light yield by structural modification. Reducing the dimensionality of perovskite materials has enormous potential for altering their electrical and optical characteristics by altering the quantum confinement and dielectric effects.[42] Quantum dots, nanowires, and 2D perovskite layers have size- and thickness-dependent light absorption and emission spectra.[64] In perovskite structures, when the A-site cation is larger than the ideal size, it disrupts the typical 3D framework, leading to a 2D layered structure.[65] In this modified structure, the oversized A-site cation functions as a spacer, separating the crystal along a particular direction. This results in alternating layers, where the inorganic BX_6^{4-} octahedral units form one set of layers, while larger organic/inorganic cations form the other. Electrostatic forces bind these layers, maintaining a stable 2D perovskite structure.[66] The inclusion of large organic/inorganic cations enhances the stability of 2D layered perovskites. Although these bulky cation layers may restrict carrier transport within the 2D layers, they play a crucial role in adjusting the electrostatic forces influencing electron–hole pairs. In this layered structure, the organic/inorganic cationic layers serve as barriers due to their larger energy gap, while the inorganic octahedral layers function as well because of their smaller energy gap.[67] Consequently, excitons are confined within the inorganic octahedral layers. The quantum confinement effect on these trapped excitons within the quantum well structure results in a higher binding energy and oscillator strength, providing the excitons in 2D perovskites with improved thermal stability and leading to a high LY.[9] Due to the increase in exciton binding energy and band gap of lower-dimensional structures compared with 3D perovskites, the electrical conductivity and thermal quenching of lower-dimensional materials remain limited. In this situation, excitonic radiative recombination-dominated light emission could be found more. For example, the LY of 3D europium-doped $RbSrI_3$ was 78 700 photons per MeV. However, it was enhanced to 90 400 photons per MeV for the 2D perovskite of europium-doped $RbSr_2I_5$.[68,69] In addition, the 3D perovskite $CsCaI_3$:Eu had LY of 40 000 photons per MeV, whereas 0D perovskites such as Cs_4CaI_6:Eu showed LY of 69 000 photons per MeV, respectively.[70,71] In another study, the highest LYs of 3D perovskite of $RbCaBr_3$:Eu and 0D perovskite of Rb_4CaBr_6:Eu reached 45 000 photons per MeV and 71 000 photons per MeV, respectively.[72] Moreover, perovskites also exhibit thermal quenching due to their low exciton binding energy. For instance, the research team led by V. B. Mykhaylyk reported that the LY of $MAPbBr_3$ was estimated to be 116 000 photons per MeV at 8 K; however, it was reduced to 90 000 photons per MeV due to increasing the temperature to 77 K.[73] To tackle the issue of thermal quenching, researchers have explored reducing the size of single crystals to lower-dimensional forms. This approach effectively confines excitons in a restricted space, enhancing the overlap of exciton wavefunctions in nanocrystals. By limiting excitons within a reduced Bohr radius, this method boosts the exciton binding energy.[74] For example, the research group led by prominent researchers V.B. Mykhaylyk studied the temperature-dependent LY of a 3D $CsPbBr_3$ single crystal and found that the intensity of light decreases with an increase in temperature.[75] In addition, they claimed that the highest LY of the crystal was of ~50 000 photons per MeV at a temperature of 7 K. Later another research group, Q. Xu *et al.*, reported that embedding 3D $CsPbBr_3$ single crystals in 0D Cs_4PbBr_6 nanocrystals is a promising strategy to enhance their LY at room temperature by inhibiting thermal quenching.[76] Additionally,

they found that the LY is ~64 000 photons per MeV at room temperature for the scintillator of $CsPbBr_3@Cs_4PbBr_6$ nanocrystals.

In addition to the quantum confinement effects in lower-dimension perovskite structures that confine excitons within the inorganic octahedral layers, thereby enhancing their binding energy, the research group led by Asai *et al.* discovered that structural distortions in the adjoining $PbBr_6^{2-}$ octahedra, specifically the Pb–Br–Pb bond angles, as well as distortions of the internal $PbBr_6^{2-}$ octahedra (Br–Pb–Br bond angles), can further contribute to exciton confinement. These distortions are thought to reduce the exciton Bohr radius, thereby enhancing the confinement effects.[77] The distortion of these octahedra can be tuned by partially replacing Pb^{2+} with various divalent cations. The research group led by Yanagida incorporated various divalent cations including Ni^{2+}, Sr^{2+}, Zn^{2+}, Sn^{2+} and Ca^{2+} in 2D perovskites to partially substitute Pb^{2+}, specifically $(C_6H_5C_2H_4NH_3)_2PbBr_4$.[78–82] As a result, this modification enhances the structural distortions in the inorganic octahedral layers due to the differences in cationic radii between the introduced cations and host cation Pb^{2+}. Due to this distortion, the exciton confinement effect is increased, hence enhancing LY. For instance, the baseline LY for pure $(C_6H_5C_2H_4NH_3)_2PbBr_4$ was 14 000 photons per MeV, which increased to 19 700 photons per MeV and 18 500 photons per MeV at doping levels of $x = 0.1$ and $x = 0.25$, respectively, due to the incorporation of Sr^{2+} into this 2D structure $[(C_6H_5C_2H_4NH_3)_2Pb_{1-x}Sr_xBr_4]$.[78] Similarly, the Cd^{2+}-doped structure $[(C_6H_5C_2H_4NH_3)_2Pb_{1-x}Cd_xBr_4]$ demonstrated LYs of 16 000 photons per MeV, 18 000 photons per MeV, 20 000 photons per MeV, and 19 000 photons per MeV at the doping level of $x = 0.05$, $x = 0.1$, $x = 0.25$, and $x = 0.5$, respectively.[81]

In recent years, self-trapped exciton (STE) emission has gained popularity as a viable approach for increasing the LY of perovskite-based scintillators.[83–85] The strong interaction between excitons and phonons is the result of localized lattice deformation, where excitons are trapped, limiting their mobility inside the crystal. In addition, the soft lattice structure of halide perovskites makes them more susceptible to distortions, facilitating the formation of STEs.[86] The research group led by Smith reported that the ratio of STE emission to free exciton emission increases with the level of distortion in the PbX_6^{4-} octahedra.[87] Additionally, another research team, Ma *et al.*, discovered that lower-dimensional halide perovskite structures promote the formation of STEs by enabling the more effective confinement of excitons and enhanced interaction with phonons.[88] The prominent research group led by Tang recently investigated the scintillation characteristics of copper-based lower-dimensional perovskites named Rb_2CuBr_3, K_2CuBr_3 and Rb_2CuCl_3, which exhibited strong STE emissions driven by Jahn–Teller distortion.[83,89,90] The STE state had a lower energy than the excited state, resulting in a significant Stokes shift. These materials also showed impressive LYs of approximately 91 056 photons per MeV, 23 806 photons per MeV, and 16 600 photons per MeV, respectively, due to their minimal self-absorption.

3.2.2 Enhancement of light yield through activators. For a material to act as a scintillator, it is essential that it has a luminescent center. These centers originated from lattice defects or the transition of electrons from the core to valence band in an intrinsic scintillator, or from the purposeful addition of impurities in intrinsic scintillators.[91] The impurities intentionally added to scintillators act as activators. Activators raise the LY of scintillators by launching additional energy states within the band gap of the host material, which may lead to more efficient light emission.[92] When radiation excites the scintillator, energy is transferred from the excited states in the host lattice to these activator centers. As the activators return to their ground state, they emit light by converting its absorbed radiation during excitation into visible photons. This process lessens energy loss as heat rather than light through non-radiative recombination, thereby improving the scintillation efficiency. Furthermore, activators can control the emission wavelength and frequently extend it into the visible region, which can be detected more effectively. In addition, matching the emission to the sensitivity range of photodetectors improves the light collecting efficiency. In some circumstances, several activators or co-dopants can be utilized to raise LY even further by promoting energy transfer pathways that increase the number of photons released. Activators also alter the decay time, with some emitting quicker, resulting in a larger light output inside the detection window of fast detectors. Thus, activators play an important role in increasing the brightness and efficiency of scintillator materials.

Rare-earth elements are commonly used as effective activators in scintillators due to their unique electronic properties. These elements have well-defined energy levels within the band gap of the host material, allowing efficient energy transfer and photons emission when exposed to radiation. Trivalent rare-earth ions including Eu^{3+}, Yb^{3+}, and Tb^{3+} are commonly known to demonstrate intrinsic 4f-4f transitions although these transitions are parity-forbidden but occur due to the mixing of states caused by the crystal field and spin–orbit coupling.[9] Conversely, the divalent elements including Eu^{2+} and Tb^{2+} display $4f^n$–$4f^{n-1}5d$ transitions, which are parity-allowed, and thus about 10^6 times stronger and emit much more intense light than 4f–4f transitions in trivalent rare-earth ions.[72] By introducing these types of ions into halide perovskite structures, their distinctive emissions can effectively amplify the Stokes shift of halide perovskite scintillators, and subsequently enhance the scintillation efficiency. For example, Yang and colleagues reported the *in situ* growth of Eu^{3+}-doped $CsPbBr_3$ quantum dots and observed a significant Stokes shift between their luminescence and absorption spectra under exposure to X-rays.[93] This shift is attributed to the intrinsic $^5D_0 \rightarrow {}^7F_J$ ($J = 1$, 2, 3, and 4) transition of Eu^{3+}, leading to reduced self-absorption and light production of 10 100 photons per MeV. In another study conducted by Katelyn A. Dagnall *et al.*, they reported that Yb^{3+}-doped $CsPbCl_3$ displayed a significant amount of light production of 102 000 photons per MeV under X-ray illumination at room temperature, which is brighter than the cutting-edge commercial scintillators.[94] Alternatively, the research group led by L. Stand observed high light production of 90 400 photons per MeV from $RbSr_2I_5$ doped with Eu^{2+}, while $RbSr_2Br_5$

doped with Eu^{2+} exhibited light production of 64 700 photons per MeV.[68,69]

Alongside rare-earth elements, a variety of other elements are now being used as activators in perovskite structures to improve the performance of scintillators. These alternative activators are being explored to optimize the LY, decay times, and overall efficiency of the scintillation process, broadening the range of materials available for enhanced detection applications. Dongsheng Yuan developed $Cs_3Cu_2I_5$ doped with a Tl activator and obtained the scintillation LY of 51 000 photons per MeV.[95] In addition, the prominent research group led by L. Stand developed two single crystals of undoped and Tl-doped $Cs_3Cu_2I_5$ through Bridgman crystal growth.[96] The undoped $Cs_3Cu_2I_5$ had an LY of 41 500 photons per MeV. Alternatively, Tl doping at 0.5 mol% resulted in an improved performance with LY of 98 200 photons per MeV at under the same level of energy.

3.3. Afterglow

The afterglow in scintillator materials, particularly those based on perovskites, is the persistent emission of light after the excitation source has been withdrawn. This effect can have a major influence on the performance of perovskite-based scintillators, particularly in applications that require accurate timing and rapid response, such as fast radiation detection. The afterglow in perovskite scintillators is frequently attributed to traps within the structure of the material, which can momentarily hold excited carriers and slowly release them over time. These traps may arise from defects, impurities, or inherent characteristics of the perovskite crystal lattice.[97,98] Although perovskite scintillators are promising due to their high LY and tunable emission wavelengths, minimization of afterglow is crucial for achieving accurate and high-speed detection. In addition, to achieve lag-free radiation detection and high-contrast imaging, particularly in the case of CT where the imaging demands are as high as 0.1% at 3 ms, minimizing afterglow is essential.[99] $Cs_2Ag_{0.6}Na_{0.4}In_{0.85}Bi_{0.15}Cl_6$ perovskite scintillators exhibit an afterglow of only 0.1% at 16 μs, which is significantly shorter than that of the commonly used CsI scintillator (1.5% at 3 ms).[57] This reduction in afterglow paves the way for real-time, dynamic X-ray imaging and medical CT applications. Thus, research efforts are directed at improving the composition and crystallinity of perovskites to decrease their trap states and increase their temporal performance in scintillator applications.

3.4. Non-proportionality in performance

Non-proportionality, where the conversion factor between deposited energy and produced light is not constant, have been studied in scintillators for over 70 years. However, at first, it was thought that the cause of nonproportionality is the thermalization of energy carriers.[100] In the 1950s, researchers thought that particles of the same energy but different types (*e.g.*, gamma rays, electrons, and alpha particles) produced different amounts of scintillation light.[101] Later, it was established that type and energy of particles were strongly correlated with the ionization density and due to the fact that the interaction of these particles with matter invariably leads to a non-uniform ionization density in the scintillator, coupled with the fact that the LY depends on the ionization density.[102] This was attributed to the differences in ionization density, with heavier particles such as alpha particles having higher ionization density, and thus lower light output due to saturation of luminescence centers.[13,103] Particularly, by the 1960s, it was understood that luminescent centers could only process one electron–hole pair at a time, and excess pairs in high-ionization-density regions led to reduced light output.[100] In 1991, the discovery of the LSO scintillator, which had a much higher light output (4–5 times) than BGO but almost similar ER, highlighted that ER was not dominated by photon counting statistics but by non-proportionality and complex energy deposition processes as well. Non-proportionality, combined with Compton scattering and photoelectric interactions, introduces event-to-event variations in light production.[101,104] More clearly, Compton scattering creates multiple discrete energy deposits, while photoelectric interactions trigger cascade processes involving fluorescent X-rays, Auger electrons, and delta rays further dividing the energy into smaller fractions.[101] These processes are involved in non-proportionality and degraded ER. The "electron response" of scintillators is considered a more fundamental probe of scintillation mechanisms because the electrons produced by Compton scattering involve fewer confounding interactions than photoelectric interactions. However, even electron-excited interactions show ER degradation due to delta rays (knock-on electrons) and Landau fluctuations, where energetic electrons deposit energy non-uniformly, creating multiple smaller deposits with varying ionization densities.[105,106] As electrons slow down, their ionization density increases, leading to further variations in light output. Thus, non-proportionality arises from a combination of ionization density effects, saturation of luminescence centers, cascade processes, and non-uniform energy deposition, all of which contribute to event-to-event variations in light production and degraded ER. Despite the extensive progress, gaps still remain in understanding the fundamental causes of non-proportionality and their quantitative relationship with ER.[101] Very recently, the research group led by J. Kaewkhao conducted a study on the non-proportionality of Cs_2LiYCl_6:Ce (CLYC) adopting the Compton coincidence technique. They reported that the electron response of the CLYC crystal decreased by approximately 7% for energies below 179 keV, which indicates greater LY non-proportionality at lower energies. However, in the case of electron energies above 200 keV, the crystal exhibited good proportionality. They also proposed that the non-proportional response primarily influences the intrinsic ER, which is linked to the crystal structure.[107,108]

3.5. Matching emission spectrum with the response spectrum of photodetectors

After the generation of light through the scintillation process, the detection of these photons is crucial. To minimize post-scintillation losses and maximize the detection efficiency, it is imperative to ensure a strong overlap between the

radioluminescence spectrum of the scintillator and the peak response window of the photodetector. This spectral alignment reduces energy losses during the detection process, leading to an overall improvement in the performance of the detector in applications including radiation detection, imaging, and high-energy spectroscopy.[109,110] Many effective scintillating materials predominantly generate ultraviolet photons with very short attenuation lengths that are rapidly absorbed within the material. This absorption causes severe loss of information. Thus, to alleviate this problem, a popular option is to include additional scintillators in the bulk material. This secondary scintillator captures ultraviolet photons and emits them as visible light.[110] Visible photons have substantially longer attenuation lengths; thus, they stay in the material for longer periods of time, increasing the total efficiency of the detector. These secondary scintillators are also known as wavelength shifters.

3.6. Refractive index

The refractive index of a scintillator material must be compatible with the refractive index of the coupling material or the refractive index of the PMT tube glass to improve the light transmission and collection efficiency in scintillation-based detection systems.[111] When scintillation photons are generated, they are emitted isotopically from the scintillator, covering a full 4π solid angle, and their migration to the photodetector is affected by the refractive index mismatch among the scintillator materials, coupling material, and window glass of the photodetector. In addition, according to Snell's law, photons can only exit the material and reach a photodetector if their angle of incidence is less than the critical angle at interfaces. Photons with incidence angle $\geq$ critical angle are subject to total internal reflection. For example, in LYSO (refractive index 1.82), only about 8% of the light escapes at the crystal–air interface.[111] Thus, a significant mismatch can initiate total internal reflection, trapping photons within the scintillator and reducing the light available for detection. Moreover, the reflection losses at interfaces and increased scattering and absorption due to mismatched refractive indices further reduce the number of photons reaching the photodetector. Minimizing the refractive index mismatch can enhance the light collection efficiency and improve the system performance. To minimize the refractive index mismatch, applying an optical grease or fluid with an intermediate refractive index between the scintillator and the photodetector creates a refractive index gradient that enhances photon transmission. This method can increase LY to 50–60%;[112] for example, Singh and research group demonstrated that coupling LYSO ($n = 1.82$) with a PMT using optical grease ($n = 1.52$) raised the light output to 50%.[113]

3.7. Energy resolution

The energy resolution of scintillators is calculated by dividing the full width at half maximum peak intensity (FWHM) by the peak position in gamma ray pulse height spectra measured by PMT. In addition, it can be formulated from three contributions, namely, inhomogeneity contribution, contribution due to nonproportional response and statistical contribution. Mathematically, it can be expressed as a squared sum of these contributions according to eqn (4).[10,114]

$$(ER)^2 = \left(\frac{\Delta E}{E}\right)^2 = R^2 = {R_{\text{inh}}}^2 + {R_{\text{npr}}}^2 + {R_{\text{stat}}}^2 \quad (4)$$

where R_{inh} represents the contribution of inhomogeneity. This may result from the inhomogeneity in crystal quality or existence of defects or nonuniform distribution of activators, causing variable LY based on the interaction point within the crystal. In addition, the nonuniform properties of the scintillator wrapping or the irregularities across the photocathode area may also affect R_{inh}. R_{npr} stands for the contribution resulting from the nonproportional response of the scintillator. R_{stat} corresponds to the statistical contribution arising from the variance in the number of detected photons N_{dp}, in addition to the variance ($\upsilon\text{ar(M)}$) resulting from electron multiplication in the PMT. This contribution is accurately characterized by Poisson statistics according to eqn (5).[115]

$$R_{\text{stat}} = 2.36\sqrt{\frac{1 + \upsilon\text{ar(M)}}{N_{\text{dp}}}} \quad (5)$$

where υar(M) is the variance in the gain when photoelectrons are multiplied in the PMT and N_{dp} is the number of photoelectrons created when scintillation photons interact with the PMT photocathode. The influence of R_{stat} on the overall ER of the detector diminishes as the LY in the scintillator increases and the dispersion caused by the PMT also decreases. The maximum LY is predominantly influenced by the emission wavelength and the band gap width of the scintillator.[116] The fundamental limit in N_{dp} at 662 keV can be expressed as eqn (6).

$$N_{\text{dp}} = QE \times \frac{662\,000}{\approx 2.5E_{\text{g}}} \quad (6)$$

Momentum conservation in the electron–electron interactions accounts for the value of 2.5.[116]

A high energy resolution (ER) corresponds to a lower R value. According to eqn (4), for a perfectly uniform scintillator crystal with ideal energy transfer, the contribution R_{inh} can be considered zero. In this case, the overall ER primarily depends on the statistical component and the nonproportionality component. To get a high ER, R_{npr} should be the lowest possible value. This is because R_{stat} is fixed and shows the theoretical limit set by the number of photons detected (N_{dp}) in the PMT. Unfortunately, R_{npr} is not negligible. For instance, the statistical limit of ER for NaI:Tl and LSO:Ce^{3+} scintillators at 511 keV is 3.8% and 4.2%, respectively.[117] However, the actual measured ERs are 7% and 9%, respectively. The nonproportionality contributions are of $\sqrt{7^2 - 3.8^2} \approx 5.88\%$ and $\sqrt{9^2 - 4.2^2} \approx 7.96\%$, respectively. Similarly, the relatively poor ER of 6–8% demonstrated by conventional scintillators including NaI:Tl, Lu_2SiO_5:Ce^{3+}, CsI:Tl, BGO, is caused by poor proportionality.[107,115] This shows that eliminating R_{npr} could nearly halve the ER values. Thus, understanding and reducing the LY nonproportionality in scintillators is critical for improving their ER.

3.8. Radiation hardness

Radiation hardness denotes the capacity of a material to preserve its scintillation efficacy without deterioration when subjected to extended or intense high-energy radiation, including X-rays or gamma rays. This property is essential in applications involving high-radiation environments, such as high-energy physics experiments, space missions, and nuclear reactors, where materials are consistently exposed to extreme radiation flux.[118] Conversely, in traditional medical imaging applications such as PET, CT, and SPECT scans, the radiation doses are relatively moderate and administered intermittently.[119] Consequently, although radiation hardness is a significant criterion for evaluating long-term material stability, its influence on routine medical imaging performance is typically minimal and receives less emphasis during the selection of materials for these clinical technologies.

4. Interaction of radiation with matter and production mechanism of scintillation light

High-energy electromagnetic radiation possesses energy typically in the range of 100 eV to 100 keV (X-rays) and 100 keV to MeV (γ-rays). The spectroscopy of this high energy radiation has an important role in the diversified field including medical imaging, nuclear nonproliferation, industrial monitoring, nuclear site inspection, astrophysical study, homeland security and basic scientific research. Due to the broad applications and great importance of this high-energy radiation detection, it is also essential to understand the interaction of radiation with materials during the detection procedures. Mainly three phenomena including PE, CE and PP are observed during the interaction of X-rays and γ-rays with the detector materials. However, there is a possibility of no interaction, Rayleigh scattering, and photo-disintegration during interaction also. Fig. 4(a) depicts the transmission, Rayleigh scattering, PE, CE, and PP.

The PE is predominantly observed in the energy range of 10 keV to 500 keV.[120] When the incident energy interacts with the detecting materials, more specifically with the orbital electrons of the atoms, the orbital electrons are ejected from atoms by getting sufficient energy from the incident radiation. The passage of the ejected electron initiates *via* the nearby matter and it starts to rapidly lose its momentum and moves only a comparatively shorter path from its origin. Thus, the energy handover is a two-step route. The first one is the PE in which the photons relocate their energy to the electron and second is the depositing of the energy in the neighboring matter by the electron. As the interaction produces a vacancy in the electronic shells, usually K or L, an electron travels to fill the vacancy by releasing energy, which is often called the characteristic X-ray photon energy. The strength of the characteristic energy relies on the binding energy of the involved electrons. Sometimes, this process transforms X-ray photons into light photons. Conversely, the CE occurs dominantly in the energy range of 50 keV to 3 MeV.[120] In CE, the incident radiation partially transfers its momentum to the orbital electrons of the atoms, and subsequently the orbital electrons are ejected from the atoms. The rest of the incoming energy will be deviated with respect to its incident direction.

Contrariwise, PP is usually observed for high energy of at least 1.022 MeV.[120] Due to the interaction of the high energy radiation with the electromagnetic field in the vicinity of a heavy nucleus, a pair of electron-positron is produced. Later the produced positron can disappear through interaction with free electrons by releasing two identical gamma energies with energy of 511 keV in opposite direction. The cross-section of interaction for these three phenomena largely depends on the proton number of the constituent atoms of the substance. The cross-section, $\sigma_{PE} \propto Z^{3to5}$, $\sigma_{CE} \propto Z$, and $\sigma_{PP} \propto Z^3$ are estimated for PE, CE and PP, respectively. A graphical representation of the dependence of PE, CE and PP on the incident radiation energy and proton number of the absorber is provided in Fig. 4(b).

A scintillator basically operates as an energy converter by transforming high-energy photons into low-energy photons in the visible range, which can be sensed by PMT or SiPM. For a material to be selected as a scintillator, it is essential for it to have a luminescent center. This center originates from lattice defects or the transition of electrons from the core to valence band in an intrinsic scintillator, or from the intentional addition of impurities in intrinsic scintillators. In both intrinsic and extrinsic scintillators, a radiative transition occurs from an excited quantum state to a low-energy quantum state. In addition, during the scintillation process, typically energy losses are observed owing to non-radiative defects, deep-level electron traps, and the de-excitation of e–h pairs through interaction with phonons during thermalization. The conversion of high-energy photons to visible photons can be divided into four steps, as follows: Step (1): energy conversion: absorption of high energy radiation produces e-h pairs. During the interaction of the high-energy photons with the scintillator material, they (photons) transfer their energy to electrons in the material, causing them to reach higher energy levels and form e–h pairs. Step (2): relaxation and thermalization: the produced e–h pairs undergo relaxation and thermalization by losing their energy until they have an energy equivalent to the band gap of the material. This process includes the interaction of the e-h pairs with the lattice, which commonly causes phonon emission. Step (3): transfer to luminescence centers: the e–h pairs are then transferred to the luminescent centers, which are specific spots in the material that allow radiative recombination. These centers might be inherent defects or impurity sites (dopants) that contain energy levels within the band gap. Step (4): light emission: when the e–h pairs recombine at these luminescence centers, the energy is released as photons in the visible range. Thus, the luminescence centers emit light, which is detected as scintillation light.

Steps (3) and (4) of the light emitting process are depicted in Fig. 4(c) by illustrating single crystalline inorganic scintillators in an energy-band scheme. Generally, rare earth elements Eu^{2+}, Ce^{3+}, *etc.* are employed to create luminescent centers into scintillator materials.[12] These rare earth elements display parity allowed electronic transitions among the electronic configurations of $4f^{n-1}5d$ and $4f^n$, resulting in rapid luminescence decay,

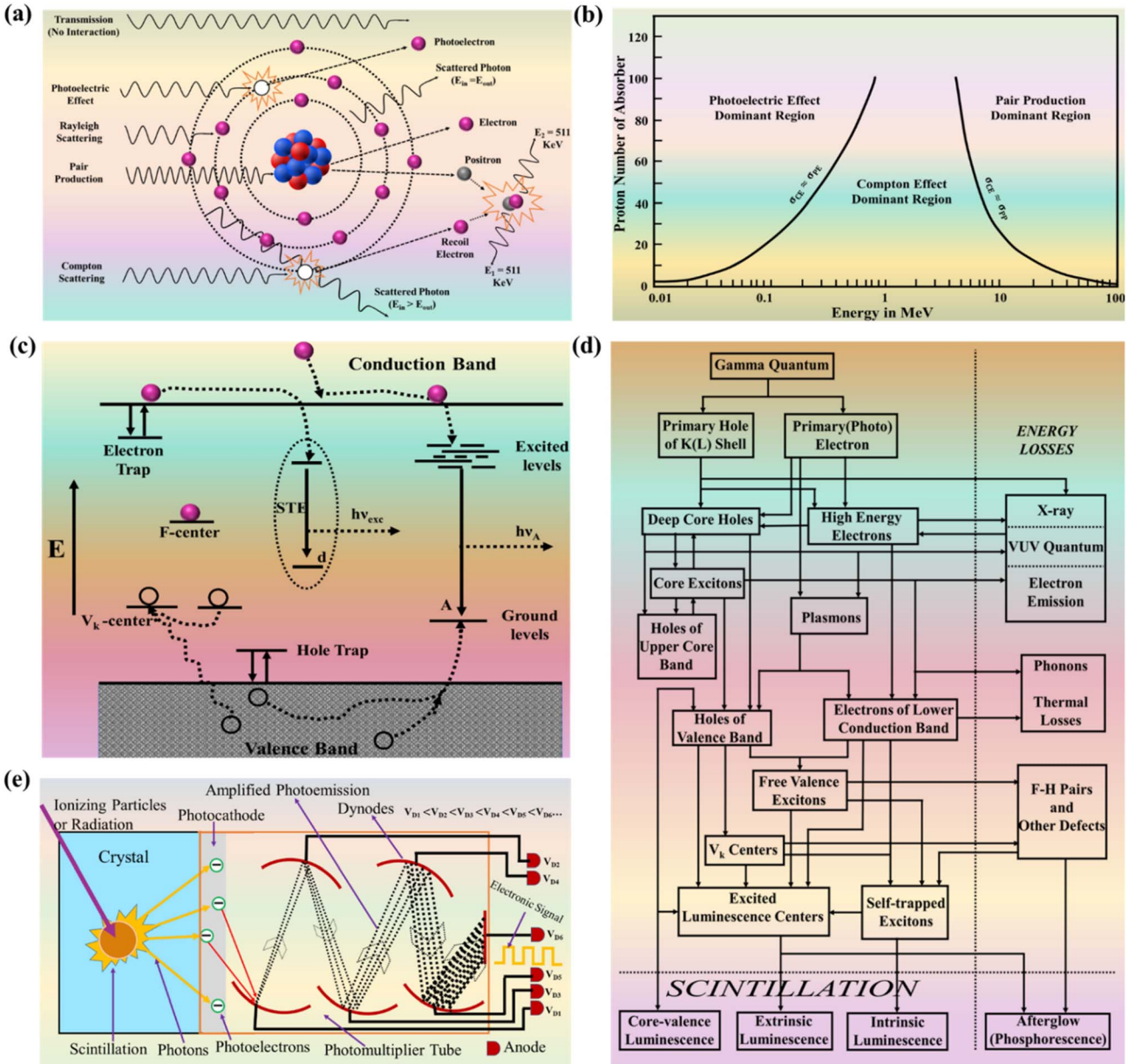

Fig. 4 (a) Graphical representation of light-matter interaction. (b) Probability of the occurrence of PE, CE and PP, depending on the incident radiation's energy and proton number of the absorber[121]. (c) Depiction of energy band scheme of the scintillation process.[91] (d) Flowchart of the scintillation in an inorganic scintillator.[91] (e) Schematic diagram of a high energy radiation detection procedure through scintillation.

which is essential for the scintillation technique.[122] The fundamentals of the scintillation process are depicted in Fig. 4 for an inorganic scintillator owing to the absorption of incident high-energy radiation.

4.1. Luminescence without activators (intrinsic luminescence)

Scintillators can be classified into two categories based on their luminescence mechanisms, *i.e.*, intrinsic and extrinsic luminescence. Their emission mechanisms are crucial in determining essential properties, including the emission wavelength and decay time. Consequently, these characteristics substantially affect the efficacy of scintillation detectors. Intrinsic luminescence arises from the inherent properties of the scintillator material including free-exciton luminescence, self-trapped exciton luminescence, Auger-free luminescence, and self-activation luminescence. Free-exciton luminescence results from the recombination of free electron–hole pairs, which is witnessed in wide bandgap scintillating semiconducting materials with direct transitions and characterized by fast scintillation decay time having a sharp emission peak in the spectrum. The examples of these scintillating materials exhibiting free-exciton luminescence include ZnO, GaN, and Ga_2O_3.[123–125]

Self-trapped exciton (STE) luminescence occurs in wide bandgap insulating materials when excitons become localized due to self-induced lattice distortion. The common scintillators

based on alkali and alkaline earth metal halides include BaF_2, SrF_2, CaF_2, $LiSrF_3$, and $LiCaF_3$.[126–130] The characteristics of STE luminescence are a broad emission peak in the spectrum, a significant Stokes shift, relatively high scintillation LY, and a decay time ranging from several hundred nanoseconds to a few microseconds. Additionally, the scintillation LY of STE exhibits strong temperature dependence.

Auger-free luminescence refers to emission occurring without Auger processes, typically in wide-bandgap materials including CsF, BaF_2, and Cs_2ZnCl_4, which is characterized by a band gap energy exceeding the energy difference between the core and valence bands.[131,132,133] Auger free luminescence exhibits a rapid decay with a short emission wavelength. However, a controversial study was performed on the temperature dependent performance of scintillators.[134,135]

Self-activation luminescence occurs when the host material naturally contains luminescent activators or consists of luminescent ions as a primary structural component. The common scintillators in this category include BGO, $CeBr_3$, $TlMgCl_3$ and $TlCaI_3$.[136–138] In BGO, $TlMgCl_3$ and $TlCaI_3$, scintillation arises from the ns^2 transitions of Bi^{3+} ions, and Tl^+, while in $CeBr_3$, it is due to the 5d–4f transitions of Ce^{3+} ions. The emission properties are determined by the luminescent ions within the host material, and notably this type of scintillator does not experience concentration quenching.

4.2. Luminescence with activators (extrinsic luminescence)

Extrinsic luminescence occurs when external activators or dopants are introduced into the host material. Among the various electronic transitions, activator-related transitions influence the luminescence characteristics of scintillators, playing a crucial role in defining their emission wavelength, decay time, and overall scintillation efficiency. The 1s ↔ 2p transition occurs in color centers (F-centers), where an electron is trapped in an anion vacancy within a crystal lattice. These centers can serve as luminescence centers by emitting light when they are subjected to irradiation. Common materials exhibiting F-centers are MgO and Al_2O_3.[139,140] In addition to F-centers, there are other related defect centers, such as F_D-centers and F^+-centers. An F_D-center involves an F-center located adjacent to a cation vacancy, while an F^+-center is a defect where an anion vacancy captures two instead of one electron. These defect centers play a significant role in the luminescence properties of scintillator materials. Conversely, the ns^2 ↔ nsnp transition is characteristic of materials with heavy elements exhibiting an ns^2 electronic configuration including Ga^+, In^+, Tl^+, Ge^{2+}, Sn^{2+}, Pb^{2+}, Sb^{3+}, and Bi^{3+}.[92] The prevalent scintillators are Tl-doped NaI, Tl-doped CsI, and BGO.[141–144] The spectral characteristic of the ns^2 ↔ nsnp transition is defined by a broad emission band, with emission wavelengths ranging from near ultraviolet to visible light. The decay time ranges from several hundred nanoseconds to several microseconds, making it suitable for pulse-height-based radiation detectors.

Conversely, the 3d ↔ 3d transitions observed in transition metals including Mn^{2+}, Cr^{3+}, and Fe^{3+} are typically parity-forbidden transitions.[145] However, these transition are allowed due to the state mixing induced by the crystal field and spin–orbit coupling. These transitions are characterized by long decay times on the millisecond scale and the emission spectra can sometimes be affected by self-absorption. Thus, these transition metals are frequently used in dosimetry applications. Similar transitions occurred in trivalent rare-earth ions (Eu^{3+}, Yb^{3+}, Nd^{3+}, and Tb^{3+}), which demonstrate intrinsic f–f transitions with a long decay time although these transitions are parity-forbidden but occur due to the mixing of states caused by the crystal field and spin–orbit coupling.[146] Recently, Eu^{3+}-doped $(Lu,Gd)_2O_3$ has gained interest for X-ray CT, offering higher emission intensity in the red region.[147] However, less investigations have been on the actinide series (5f–5f transition).

Instead, divalent and trivalent elements including Eu^{2+}, Tb^{2+}, Ce^{3+} display $4f^n$–$4f^{n-1}5d$ transitions, which are parity-allowed, and thus about 10^6 times stronger and emit much more intense light than f–f transitions in the trivalent rare earth ions.[72] Emissions due to the transitions (5d–4f transitions) of trivalent and divalent rare-earth ions are very important for scintillation detectors because they show intense and fast emissions by spin- and parity-allowed transitions. In the research conducted by Dagnall *et al.*, they reported that Yb^{3+}-doped $CsPbCl_3$ displayed a significant amount of LY under X-ray illumination at room temperature, which is brighter than the cutting-edge commercial scintillators.[94] Conversely, the research group led by Stand observed high LY and better ER from $RbSr_2I_5$ doped with Eu^{2+} under gamma energy.[68]

Lastly, charge transfer luminescence can occur in certain atomic groups, including Yb^{3+}-doped materials and compounds containing VO_4^{3-} and WO_4^{2-}. Examples are Lu_2O_3:Yb, YVO_4 and $CaWO_4$.[148–150] Among the materials with charge-transfer luminescence, $CdWO_4$ has been used with Si-PD for X-ray detectors for security applications.[151]

5. Single crystal development method

The quality of crystals is essential to efficiently absorb and convert ionizing radiation into detectable light in the scintillation process. High-quality crystals ensure the optimal performance in terms of light output, ER, and reliability. The development of high-quality single crystals (ingots) involves specific crystal growth techniques that produce highly ordered structures with a continuous lattice and no grain boundaries. These methods are primarily used in the semiconductor, photovoltaic, and optical industries. Here, the most common methods for the development of single crystals are discussed.

5.1. Czochralski method

The Czochralski method, developed in 1916 by Polish scientist Jan Czochralski, is a widely used technique for growing high-quality and large single crystals of semiconductors, metals, salts, and synthetic gemstones for different applications in opto-electronics.[152,153] Additionally, this crystal growth

technique allows precise control of the crystal orientation by using a seed crystal with a specific orientation and enables the production of single crystals with minimum defects at a relatively faster growth rate. The process begins with a crucible containing the raw material, which is usually melted at high temperatures in an inert or vacuum atmosphere to prevent contamination. Then, a seed crystal of the chosen material is carefully dipped into the molten. This seed is gradually lifted up along with rotation, enabling the molten material to solidify on its preferential surface and create a single-crystal structure. In addition, the pulling rate and the temperature gradient are precisely controlled to ensure uniform crystal growth. Moreover, factors such as the rotation speed and the ambient conditions also directly influence the quality of the crystal. Similarly, using this method, R. Zheng and group effectively developed a single-crystal perovskite of $Cs_3Cu_2I_5$ doped with thallium.[154] Their findings discovered an LY of 81 000 photons per MeV and ER of 5.2% under the exposure of 662 keV. A schematic diagram of the Czochralski method is presented in Fig. 5(a).

5.2. Bridgman–Stockbarger method

The Bridgman–Stockbarger (BS) scheme is one of the various types of crystallization processes from a melt, in which the crystallization happens from a melt when the melt is cooled, lowering its icing point and leading to the fusion, and then solidification of the pure substance. During the synthetization of SCs, there are no probable sources of pollutants apart from the contamination from the crucible substance as well as the surroundings. Additionally, the crystallinity and growth rate are generally higher than that of other existing approaches. According to this approach, the composition of perovskite will be melted during the passing of the silica ampule filled by perovskite precursor through the hot region, and then the perovskite material will be nucleated and grown into a SC due to the movement of the ampule toward the cold region. The eminent research group led by V. B. Mykhaylyk developed a single crystal of $CsPbBr_3$ to explore its scintillating properties by means of the Bridgman-Stockbarger method.[155] The $CsPbBr_3$ crystal produces 50 000 photons per MeV when excited by X-rays at 12 keV and 109 000 photons per MeV when excited by α-particles from ^{241}Am at 7 K. A schematic diagram showing the different components of the Bridgman–Stockbarger method for SC development is provided in Fig. 5(b).

5.3. The edge-defined film-fed growth

The edge-defined film-fed growth method is another method to grow crystals, which builds on the Czochralski process by introducing a floating graphite die on the melt surface.[156] At the top of the die, there is a pool, which is filled by molten material through narrow tiny channel due to capillary action principles. Then, a seed crystal is lowered to contact the melt in the pool, and crystallization occurs under the optimal thermal conditions. As the seed is pulled upward at a controlled rate (1–10 mm h^{-1}), the molten substance solidifies, and the crystal grows with a cross-section defined by the shape of the die.[157] By controlling the environmental condition and pulling speed, the crystal formation can be smooth and uniform.

This technique is great for forming crystals with consistent shapes including sheets or ribbons because the die directly controls the size and shape of the crystal. The prominent research group of G. Calvert and colleagues developed a strontium iodide (SrI_2) scintillator crystal for the first time by the edge-defined film-fed growth method.[158] They claimed that the LYs were in the range of 90 000 to 107 000 photons per MeV and ER in the range of 5.96% to 3.69% for different crystals of SrI_2 doped with europium. Similarly, using this method, R. Zheng and team successfully developed a single crystal of $Cs_3Cu_2I_5$ doped with thallium.[154] Their findings revealed an LY of 79 000 photons per MeV and ER of 5.4%.

5.4. Floating zone method

The floating zone technique is another effective method for developing high-quality single crystals.[159–161] In this procedure, a feed rod of the material is vertically positioned, and a tiny molten zone is formed at the center using targeted heating, often with a laser, halogen lamp, or radio frequency induction. The molten zone is held together by surface tension between the feed rod and the developing crystal. As the molten zone travels up the rod, the material solidifies with a controlled crystal orientation, resulting in a defect-free single crystal. The floating zone approach is particularly useful since it eliminates contamination from crucibles and allows exact control over crystal formation factors, such as temperature gradients and growth rates. This makes it ideal for developing high-quality crystals for advanced optical, electronic, and scintillation applications. R. Takahashi and colleagues developed a single crystal of $Ca_3TaGa_3Si_2O_{14}$ doped with thulium by the floating-zone method.[162] The scintillator with 0.1%, 0.5%, and 1% Tm-doping displays the LYs of 1300 photons per MeV, 1800 photons per MeV, and 1500 photons per MeV under γ-ray irradiation, respectively. In addition, the well-known research group of Yusuke Endo and colleagues developed a perovskite $Ca_{1-x}Mg_xHfO_3$ scintillator crystal doped with terbium by the floating zone method and they found the highest LY of 17 400 photons per MeV.[163] In another experiment, Y. Endo and team developed $CaHfO_3$ single crystals doped with Dy using the floating zone technique, and they confirmed from the pulse height spectra of ^{137}Cs that 3.0% Dy:$CaHfO_3$ exhibited an LY of 20 000 photons per MeV.[164] A schematic diagram of the floating zone method is presented in Fig. 5(c).

5.5. Solution-based single crystal growth techniques

The crystal growth methods based on melting suffer from high energy costs and challenges to form uniform crystals due to the differing solidification points (temperatures) of constituent compounds. Often they lead to phase segregation, compositional inhomogeneity, and structural defects, which affect the performance of scintillators. Therefore, future research should place greater emphasis on alternative cost effective and solution-based crystal growth methods. Perovskite material-based single crystals can be synthesized using simple solution

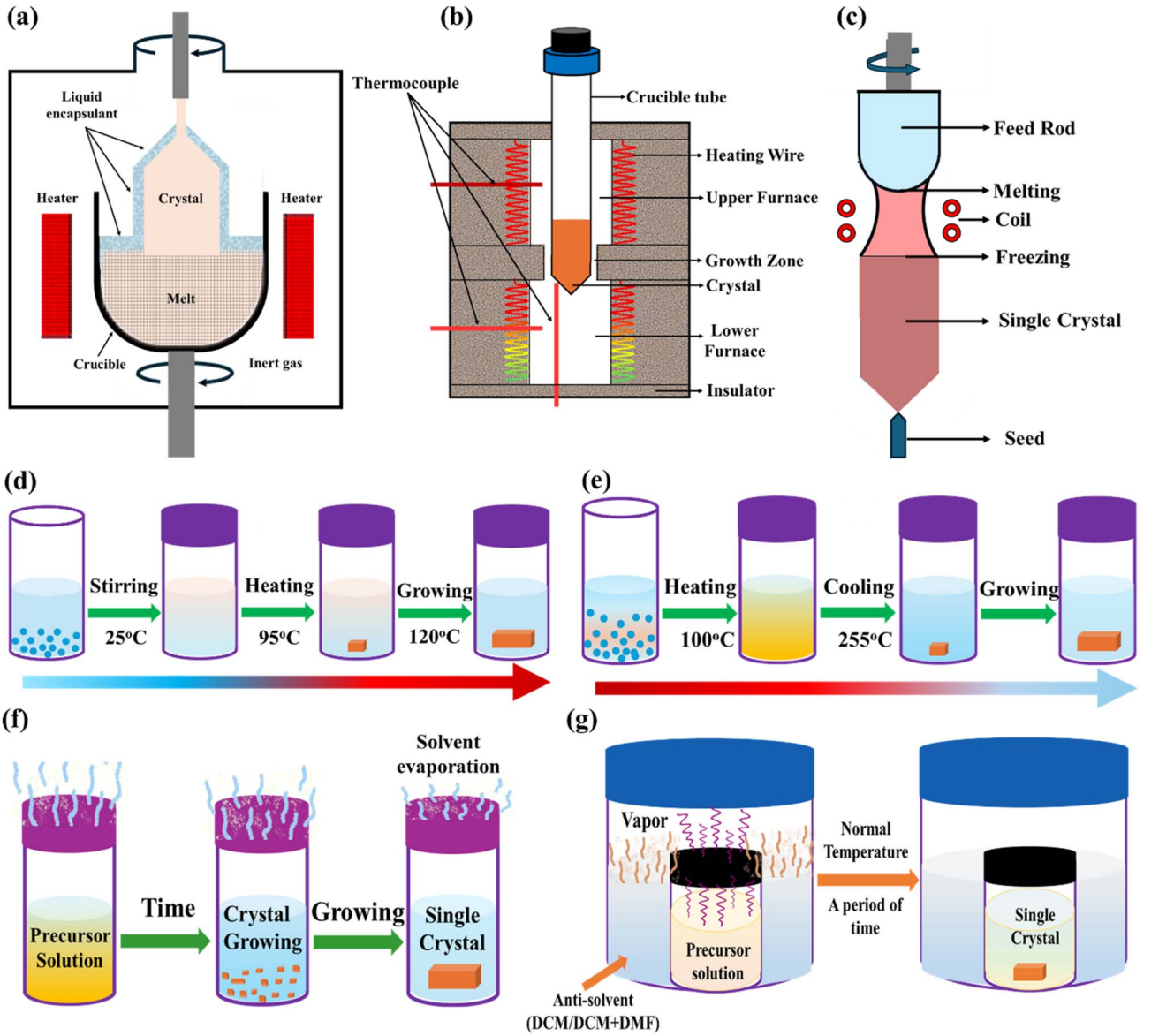

Fig. 5 Schematic of the (a) Czochralski method; (b) Bridgman–Stockbarger method; (c) floating zone method; (d) inverse-temperature crystallization; (e) temperature-lowering crystallization; (f) slow solvent evaporation method and (g) antisolvent vapor-assisted crystallization for SC development.

processes at temperatures below 150 °C. Some prominent solution methods for growing single crystals including inverse-temperature crystallization (ITC), slow solvent evaporation method, temperature-lowering crystallization, and antisolvent vapor-assisted crystallization techniques are utilized to create crystals.[165–168] Schematic diagrams of a few solution-based SC growth methods are presented in Fig. 5(d–g).

6. Performance analysis of perovskite scintillators derived from alkali metal halides and alkaline earth metal halides

Scintillators, as a primary category of radiation detectors, hold significant importance in the realms of radiation detection and imaging. The evolution of scintillators has emerged with alkali and alkaline metal halides as first-generation scintillators, developed between the 1940s and 1970s, consisting of simple chemical compounds such as NaI and CsI, along with natural phosphor materials such as CaF_2 and $CdWO_4$, which were widely used due to their basic scintillation properties. Then, second-generation scintillators emerged in the 1970s, with BGO (bismuth germanate) being a notable advancement, offering a higher density and improved gamma-ray detection efficiency, making it valuable for medical imaging and high-energy physics applications. Since the 1990s, third-generation scintillators have been developed, primarily based on host materials doped with an emission center, such as Ce-doped LSO and LYSO. These modern scintillators follow three main trends of rare-

earth silicates, rare-earth garnets, and halide materials.[13] Among them, halide materials from alkali and alkaline groups of periodic tables and their combination are a niche area of research because of their enhanced LY, faster decay times, and improved ER, making them highly effective for advanced imaging and radiation detection technologies. Among the initial inorganic scintillators, alkali metal halides exhibit promising scintillation properties and better performance in high energy radiation detection. More specifically, thallium (Tl)-doped NaI and CsI are extensively utilized in medical imaging, high energy/space physics and homeland security.[169,170] In addition, CsI:Tl stands as a prominent scintillator, having found utility across a multitude of applications over several decades. With an impressive LY of 54 000 photons per MeV and minimal sensitivity to moisture, making it nearly non-hygroscopic, CsI:Tl is distinguished as a reliable and efficient gamma-ray detector, featuring an emission spectrum that peaks at around 540 nm.[170] Moreover, the ER typically reaches approximately 4.42% to 6% at 662 keV for CsI:Tl when paired with photodetectors.[171–173] Thallium-doped sodium iodide (NaI:Tl) scintillators are commonly employed in radiation detection, and in general demonstrate an ER of 6.5 to 7% at 662 keV.[170,174] A recent investigation has paid attention to improving their performance through various strategies. Co-doping with alkaline metals including Sr^{2+} and Ca^{2+} has shown promising results by improving the ER to 5.3% and reducing the decay time to 170 ns.[174] In addition, lithium halides, potassium halides, and rubidium halides doped with different activators show promising scintillation properties and performances for detecting high-energy electromagnetic radiation and particles.[175–177] Thus, undoped alkali metal halides and doped with various activators exhibit promising scintillation properties and better performances in the detection of high energy radiation.

Conversely, alkaline earth metal halides more specially, beryllium halides, magnesium halides, calcium halides, strontium halides, barium halides, radium halides (less studied due to the radioactivity of radium) doped with various activators have been studied for deciphering their scintillation properties and applied to detect high-energy electromagnetic radiation and particles. In addition, alkaline halide materials exhibit a high effective atomic number, which enhances their photoelectric cross-section.[178] Among the alkaline earth metal halides, europium-doped strontium iodide (SrI_2:Eu) has surfaced as a noteworthy scintillator material for gamma-ray spectroscopy and radio-isotope identification. Although it was first developed by Hofstadter in 1968, its remarkable characteristics have come to light day by day due to advancements in crystal growth methods and characterizations techniques.[179] Moreover, SrI_2:Eu demonstrates an impressive LY surpassing 120 000 photons per MeV, along with outstanding ER of 3% at 662 keV.[179,180] In addition, BaBrI doped with Eu also shows a high light output of 71 000 photons per MeV and ER of 4.3% at 662 keV.[181] Moreover, CaI_2 scintillator was also confirmed to have a high light output of 107 000 photons per MeV and ER of 3.2% at 662 keV, which was 2.7 times higher than that of NaI(Tl).[182] Thus, undoped alkaline earth metal halides and doped with various activators demonstrate promising scintillation properties along with better performance in the detection of high-energy radiation.[183]

In recent years, the outstanding scintillation performance of alkali metal halides (*e.g.*, CsI) and alkaline earth metal halides (*e.g.* SrI_2) have motivated the scientific community to investigate the combination of both halides materials, integrating the benefits of both classes of halides. The combination of these two halides in various ratios results in the formation of different dimensional perovskite materials featuring a variety of structural configurations, including $AX:BX_2 = ABX_3$ (3D), $2AX:BX_2 = A_2BX_4$(2D), $AX:2BX_2 = AB_2X_5$ (2D) and $4AX:BX_2 = A_4BX_6$ (0D) frameworks.[69,184–187]

In addition, elements from these two categories can be combined with other groups of elements to form various types of perovskites, such as $A_3B^{3+}{}_2X_9$ (2D) and $A_2B^{+}B^{3+}X_6$ (3D) structures. The electronic and optical properties of these perovskite materials can be adjusted for better scintillation performances including high LY for outstanding ER, which can position them as strong candidates for future scintillation technologies. In addition, reducing the dimensionality of perovskite materials holds significant promise for modifying their bandgap properties, ultimately resulting in changes to their optoelectronic features.[201]

When perovskite structures are restricted to two, one, or even zero dimensions, the effects of quantum confinement and dielectric confinement become increasingly significant, leading to adjustable bandgaps and unique optoelectronic properties and enabling precise manipulation of their light absorption and emission spectra.[202,203] The ability to alter the bandgap of perovskites through dimensionality reduction presents exciting opportunities in various applications, where meticulous control of optoelectronic properties is essential for optimal device performance. By utilizing the combined characteristics of alkali and alkaline earth metal halides in these dimensional structures, experts seek to tackle issues related to the detection of high-energy electromagnetic radiation and particles, with potential uses in medical imaging, nuclear spectroscopy, and particle physics. This new category of materials presents an exciting opportunity for developing high-performance scintillators. Photographs of successfully grown single crystals with varying compositions, activator concentrations and dimension are displayed in Fig. 6(a–r).

6.1. ABX_3 perovskite scintillators

The most common and widely recognized structure of perovskite is ABX_3, which can be produced using an equal mixture of alkali metal halides (AX) and alkaline earth metal halides (BX_2). The scientific community seeks to harness and integrate the beneficial features of both groups of materials, given that each exhibits remarkable efficacy in the detection of high-energy particles. In the pursuit of advancing intrinsic ABX_3-based perovskite scintillators, various research teams have encountered challenges, as these scintillators have not demonstrated the desired performance metrics including LY, ER, and energy linearity. For example, the prominent research group led by K.

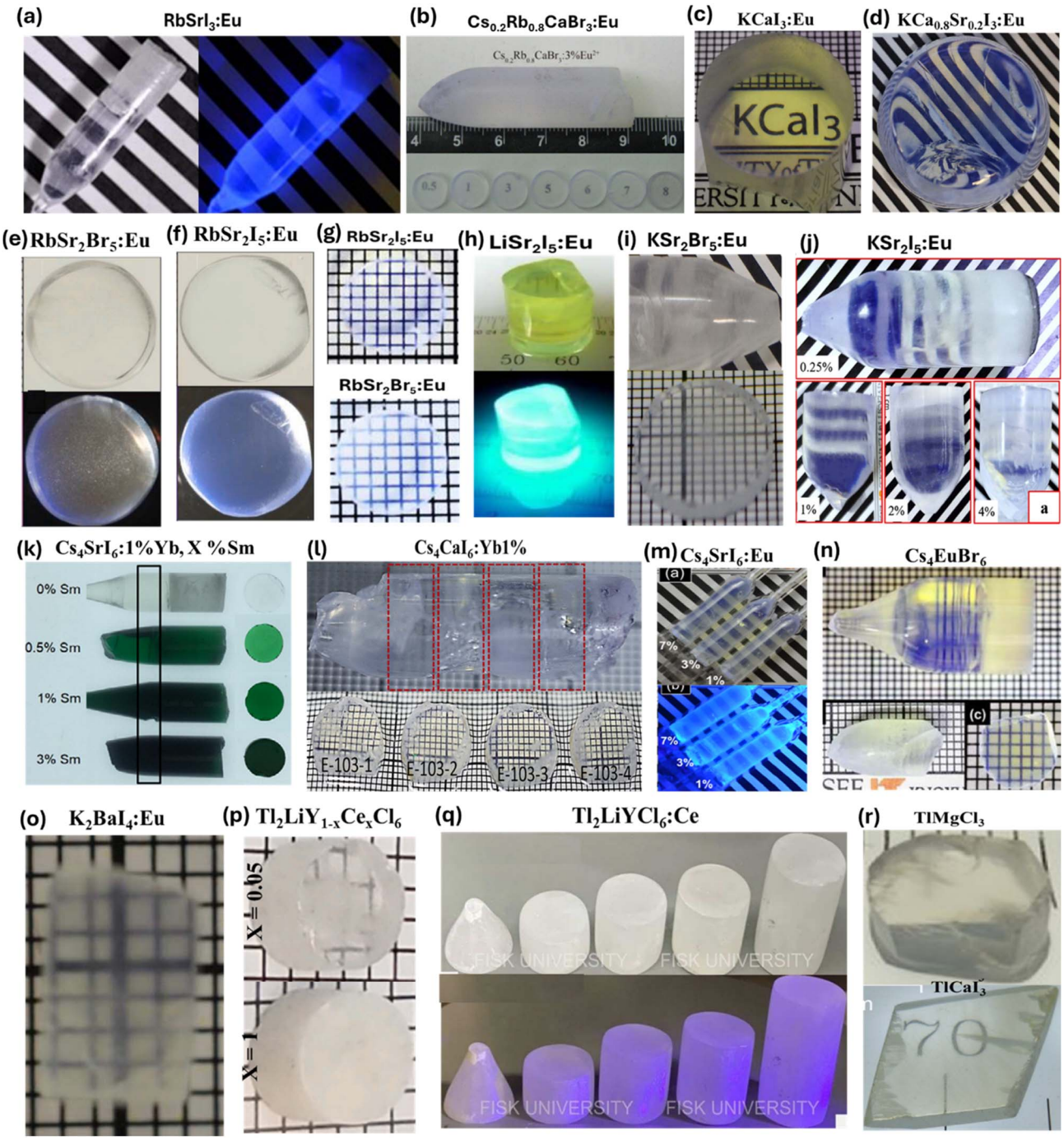

Fig. 6 (a–r) Photographs of successfully grown single crystals with varying compositions, activator concentrations and dimensions. The images reflect high optical transparency, uniformity, and luminescent properties under ambient and UV illumination. (a) Reprinted from ref. 69 with permission from Elsevier, Copyright 2024; (b) reprinted from ref. 188 with permission from Elsevier, Copyright 2022; (c) reprinted from ref. 189 with permission from Elsevier, Copyright 2015; (d) reprinted from ref. 190 with permission from Elsevier, Copyright 2017; (e and f) reprinted from ref. 191 with permission from Elsevier, Copyright 2025; (g) reprinted from ref. 68 with permission from Elsevier, Copyright 2017; (h) reprinted from ref. 192 with permission from IEEE, Copyright 2016; (i) reprinted from ref. 193 with permission from Elsevier, Copyright 2015; (j) reprinted from ref. 194 with permission from Elsevier, Copyright 2018; (k) reprinted from ref. 195 with permission from Wiley, Copyright 2023; (l) reprinted from ref. 196 with permission from Elsevier, Copyright 2020; (m) reprinted from ref. 70 with permission from Elsevier, Copyright 2019; (n) reprinted from ref. 197 with permission from RSC, Copyright 2018; (o) reprinted from ref. 198 with permission from Elsevier, Copyright 2016; (p) reprinted from ref. 199 with permission from Elsevier, Copyright 2022; (q) reprinted from ref. 200 with permission from Elsevier, Copyright 2022; and (r) reprinted from ref. 138 with permission from Elsevier, Copyright 2017.

S. Pestovich successfully synthesized an intrinsic scintillator of $RbSrI_3$ through the precise mixing of RbI and SrI_2 in an optimal ratio with help of the widely used Bridgman-Stockbarger single-crystal growth technique.[69] They reported essential performance metrics including an LY of 8000 photons per MeV, ER of 7.9%, and fast decay time of 375 ns under exposure from a radioactive source of 137Cs (662 keV). Generally, undoped scintillators often exhibit a relatively lower performance compared to doped scintillators, including reduced light production because of the lack of activators, which facilitate radiative relaxation. Dopants introduce additional efficient recombination pathways, which slow the decay times along with high LY compared to undoped materials. Moreover, undoped scintillators emit intrinsic wavelengths that may not effectively align with the detector response curve, which may be another issue that reduces the overall performance. These variables cumulatively lead to a diminished scintillation performance. The same research group assessed the effects of introducing various elements as an activator into the same framework. Upon doping $RbSrI_3$ with 5% Eu^{2+}, outstanding performance metrics were documented including a high LY of 78 700 photons per MeV, decay time of 1.03 μs, and ER of 2.8% under the same radiation source.[69] In addition, upon the introduction of 0.5% Yb^{2+} as a dopant, the LY of the scintillator reduced to 24 000 photons per MeV, accompanied by a scintillation decay time of 795 ns and ER of 4.9% under the 137 Cs gamma source. However, the observed reduced LYs in the structure of Yb-doped scintillators can be attributed to an inadequate concentration of the dopant, which might consequently lead to a reduced number of radiative relaxation pathways. Another prominent research group, headed by M. Zhuravleva, developed two $RbCaBr_3$ scintillators doped with 5% and 7% Eu^{2+}, respectively.[72] The reported LYs were 37 000 photons per MeV and 43 000 photons per MeV with the corresponding ERs of 7.6% and 4% of each device doped with 5% and 7% Eu^{2+}, respectively. Furthermore, a scintillator based on $CsSrI_3$ with different concentrations of Eu^{2+} doping was developed by the group of K. Yang *et al.*.[204] According to them, their structure worked best with 8% Eu^{2+} doping. However, when Eu^{2+} completely replaced Sr^{2+}, they observed a drop in performance. In particular, the LYs of $CsSrI_3$:1% Eu, $CsSrI_3$:8% Eu and $CsEuI_3$ (totally replaced Sr^{2+} with Eu^{2+}) were 32 000 photons per MeV, 65 000 photons per MeV and 24 000 photons per MeV, with the corresponding ER of 9%, 5.9% and 11%, respectively. More importantly, the fully Eu-substituted structure ($CsEuI_3$) showed similar features to that of the undoped ABX_3 material and may not have extra pathways for additional light emission that would improve the scintillation performance of the device. Alternatively, the performance can be optimized through compositional engineering of the ABX_3 framework by maintaining a fixed activator concentration. For instance, the Japanese research team headed by K. Mizoi investigated the scintillation characteristics of ABX_3 *via* composition engineering, while keeping the dopant concentration constant.[205] By maintaining the Yb^{2+} dopant concentration at 1% through whole study, they completely replaced Sr^{2+} in compounds of $CsSrCl_3$ and $CsSrBr_3$ with Ca^{2+}. As a result, they observed an enhanced LY from 16 000 photons per MeV ($CsSrCl_3$) to 48 000 photons per MeV ($CsCaCl_3$) and 23 000 ($CsSrBr_3$) to 120 000 photons per MeV ($CsCaBr_3$), respectively. In addition, another research group adopted a similar strategy to improve the scintillator performance. Specifically, two devices were developed with $CsCaBrI_2$:Eu 7% and $CsSrBrI_2$:Eu 7% (by replacing Ca by Sr) and they demonstrated an enhanced performance in both LY (from 51 800 photons per MeV to 65 300 photons per MeV) and ER (from 3.8% to 3.4%), respectively.[206]

The non-proportionality of LY in scintillators represents a multifaceted phenomenon that arises from the intricate interactions between microscopic and macroscopic processes occurring within the scintillator material. More specifically, it emerges from the intricate interaction of energy deposition, thermalization, transport, and recombination mechanisms, all of which are affected by the types of incident particles and energies, ionization density and nature of the energy carriers generated during the scintillation process.[100] Various research teams investigated the non-proportionality issue in ABX_3 perovskite structures, although these studies are still limited in these compounds. Notwithstanding these endeavors, the above-mentioned issue remains prevalent in ABX_3 perovskite systems. For example, the research team of A. C. Lindsey explored the non-linearity in the scintillator performance of $KCaI_3$:Eu 3% with different sizes.[189] The findings revealed that the device with ∅ 2 mm × 5 mm crystal achieved an ER of 3% when it was subjected to 662 keV energy emitted from a ^{137}Cs source. Alternatively, relatively lower ER of 6.1% was recorded when the same device was subjected to 122 keV energy emitted from a ^{57}Co source. Moreover, the device with larger dimensions of ∅ 17 mm × 17 mm crystal under excitation from ^{137}Cs and ^{57}Co source demonstrated the ER of 4.4% and 7.3%, respectively. The observation of outcomes underscores a divergence in performance, suggesting a lack of proportionality in the response of the scintillator. The research group investigated the factors contributing to the fluctuation in ER and determined a non-proportionality degree of roughly 0.015, which is similar to the high-performance scintillator $LaBr_3$:Ce, documented to exhibit a non-proportionality of 0.013 in existing literature.[219] Furthermore, the statistical impact on the decrease in performance was around 2.3% for the small crystal and 2.8% for the big crystal at 662 keV. They determined that the principal factor affecting the decline in ER was the inhomogeneity of faults, impurities, or activators inside the crystal. Nonetheless, they observed that statistical factors probably exert a significant influence on the total performance. Another research team, headed by Y. Wu, also observed the non-proportionate ER of a perovskite-based scintillator with dimensions of ∅ 50 mm × 45 mm, developed from $KCa_{0.8}Sr_{0.2}I_3$:Eu 0.5%.[190] Particularly, when the device was exposed to 662 keV radiation from a ^{137}Cs source, it demonstrated an ER of 4.1%, whereas the device exhibited a substantially lower ER of 7.9% under exposure from 122 keV radiation from a ^{57}Co source. Similar observations by the research team of Y. Wu *et al.* for a scintillator made from $KCa_{0.835}Sr_{0.165}I_3$:Eu 3% found different ER of 2.5% and 5.9% under exposure from ^{137}Cs (662 keV) and ^{57}Co (122 keV), respectively. However, a remarkable LY of 74 000 photons per

MeV was observed under exposure from ^{137}Cs (662 keV). Finally, the degree of non-proportionality of the structure was 0.015.

A contemporary research trend emphasizes the integration of alkali or alkaline earth metal halides with other halide materials to investigate their feasibility and performance over diverse energy ranges. As part of their efforts, A. Khan and team developed an intrinsic scintillator by combining TlCl and $CaCl_2$ in a proportionate ratio using the Bridgman–Stockbarger method.[218] Similar to other intrinsic scintillators, the performance of $TlCaCl_3$ remained limited, which may be due to the absence of additional pathways for radiative recombination, which are typically introduced through activators in scintillating materials. Specifically, the device exhibited an LY of 30 600 photons per MeV, scintillation decay time of 727 ns, and ER of 5% when exposed to a ^{137}Cs (662 keV) radiation source. In addition, the research group also investigated the non-proportionality of the device performance under different ranges of energy from diverse radio isotopes. At higher energy levels, the response exhibited a linear proportionality; however, at a lower energy of incident gamma rays (less than 350 keV), this proportionality diminishes. A more important observation was that the scintillation response of the $TlCaCl_3$ crystal demonstrates a notable linearity compared to traditional alkali halide crystals such as NaI:Tl and CsI:Tl.[218] Another research team developed two intrinsic scintillators named $TlCaI_3$ and $TlMgCl_3$.[138] However, their performance metric remains inadequate compared to activated scintillators. In particular, $TlCaI_3$ showed an LY of 42 200 photons per MeV alongside an ER of 6.2%, whereas $TlMgCl_3$ revealed an LY of 30 600 photons per MeV with an ER of 3.7%. A notable discovery was their rapid intrinsic band-to-band decay with a decay time of 200 ns and 449 ns for $TlCaI_3$ and $TlMgCl_3$, respectively, which is essential for obtaining precise and fast high-energy spectroscopy. The investigation further analyzed the non-proportionality of the two devices and observed that $TlCaI_3$ demonstrated a nearly linear correlation between incident energy and LY, while $TlMgCl_3$ displayed non-linearity at lower radiation energies. Although $TlCaI_3$ demonstrates praiseworthy proportionality, it exhibits a moderate ER of 6.2% at 662 keV, which can be attributed to its comparatively low crystal quality. Furthermore, the research group of M. Arai and colleagues developed various scintillator crystals using the self-seeding solidification method to investigate the photoluminescence properties of $(Tl_{1-x}A_x)MgCl_3$, where A represents an alkali metal dopant.[220] They observed varying LYs when 0.5% of different alkali metals was substituted at the A site in the perovskite structure. Particularly, the LYs for $(Tl_{0.995}Li_{0.005})MgCl_3$, $(Tl_{0.995}Na_{0.005})MgCl_3$, $(Tl_{0.995}K_{0.005})MgCl_3$, $(Tl_{0.995}Rb_{0.005})MgCl_3$, $(Tl_{0.995}Cs_{0.005})MgCl_3$, and $TlMgCl_3$ were of 28 000 photons per MeV, 27 000 photons per MeV, 55 000 photons per MeV, 35 000 photons per MeV, 49 000 photons per MeV, and 42 000 photons per MeV, respectively. Additionally, the study confirmed a fast decay rate similar to previous findings, with decay times of 319 ns, 197 ns, 269 ns, 295 ns, 259 ns, and 350 ns for the respective scintillators. Various studies have established that a proportionate ratio of alkali or alkaline earth metal halides with other substances to for the ABX_3 framework yields intrinsic scintillators, which reliably exhibit rapid decay due to band-to-band decay scheme, moderate ER, and a linear performance response across diverse energy levels. Several promising perovskite scintillators along with their performance metrics are presented in Table 1 and SI Table S1.

6.2. AB_2X_5 perovskite scintillators

This section reviews the scintillation performance of various undoped and doped AB_2X_5 framework materials composed of a proportionate ratio of alkali (AX) and alkaline earth metal halides ($2BX_2$). Lower-dimensional materials can sometimes offer advantages in scintillation performance due to their unique electronic and optical properties, such as enhanced quantum confinement effects and reduced defect densities over bulk scintillators. Many research groups investigated the performances of intrinsic AB_2X_5 scintillators. Under K. S. Pestovich, one of these groups developed an intrinsic scintillator with $RbSr_2Br_5$ using the Bridgman–Stockbarger technique.[191] However, the first performance of this device fell short of expectations with an LY of 2400 photons per MeV, scintillation decay time of 2.2 μs, and ER of 12.9%. However, they used composition engineering of the AB_2X_5 framework to improve its performance and obtained notable results when they replaced bromine with iodine. Upon exposure to 662 keV radiation (^{137}Cs), the revised scintillator showed an LY of 14 000 photons per MeV, a lower decay time of 1.9 μs, and enhanced ER of 7.9%. The general performance of the scintillator was improved by this compositional change. Notwithstanding these advances, other intrinsic scintillator designs have shown comparably poor performances; this could be explained by the lack of extra radiative recombination channels.[35] Different research groups have added various activators, such europium (Eu) and samarium (Sm), into scintillator materials to solve this constraint and increase the number of radiative pathways. These activators are included to increase the efficiency of radiative recombination, thus enhancing the general scintillator performance. For example, prominent researcher K. S. Pestovich and colleagues incorporated different concentrations of divalent europium into $RbSr_2Br_5$ and $RbSr_2I_5$ scintillators.[191] Significant improvements in performance were noted including an increase in LY from 2400 photons per MeV to 73 000 photons per MeV for $RbSr_2Br_5$ and 14 000 photons per MeV to 90 000 photons per MeV for $RbSr_2I_5$ upon activation with 5% Eu. Furthermore, the ER was enhanced from 12.9% to 3.9% for $RbSr_2Br_5$ and 7.9% to 2.9% for $RbSr_2I_5$. These findings indicate that the incorporation of Eu activators successfully established multiple radiative recombination pathways, which lead to a notable improvement in the scintillation efficiency and overall performance of the materials. In addition, using a similar approach, the research team led by P. Dorenbos improved the performance of the intrinsic scintillator $CsBa_2I_5$.[35] Key performance indicators were significantly improved by including 5% divalent europium as an activator. Upon exposure to 662 keV radiation from ^{137}Cs, the LY climbed from 22 000 photons per MeV to 80 000 photons per MeV and the ER improved from 9.6% to 2.3%. These results show how well the inclusion of Eu

Table 1 Performance metrics of ABX_3 perovskite scintillators under various ranges of gamma energy

Material		Crystal growth method	Volume (mm^3)	Emission wavelength (nm)	Source	LY photons per MeV	Decay time (μs)	ER (%)	Ref.
ABX_3	$CsSr_{0.93}Eu_{0.07}I_3$	Vertical gradient freeze(VGF)	—	455	^{137}Cs (662 keV)	73 000	3.2	3.9	207
	$Cs_{1.06}Sr_{0.8742}Eu_{0.0658}I_{2.94}$	BS	5702.7	469	^{137}Cs (662 keV)	44 000	3.7	3.4	208
					^{57}Co (122 keV)	—	—	6.8	
	$RbSrI_3$:5% Eu	BS	77	462	^{137}Cs (662 keV)	78 700	1.03	2.8	69
	$RbSrI_3$:0.5% Yb			457		24 000	0.795	4.9	
	$CsBaI_3$:2% Eu	BS	—	429	^{137}Cs (662 keV)	55 000	0.760	3.8	209
	$CsBaBr_3$:2% Eu		—	425	^{137}Cs (662 keV)	22 000	1.193	5.5	
	$CsSrI_3$:2% Eu		—	450	^{137}Cs (662 keV)	20 000	0.700	5.5	
	$CsSrBr_3$:2% Eu		—	431	^{137}Cs (662 keV)	17 000	0.973		
	$KCaI_3$:3% Eu	BS	4	—	^{137}Cs (662 keV)	70 000	1.0	3.8	210
	$CsCaI_3$:5% Eu		8	—	^{137}Cs (662 keV)	39 000	1.0 s	3.8	
	$CsSrBr_3$:5% Eu		—	—	^{137}Cs (662 keV)	40 000	3.0	3.8	
	$CsSrI_3$:7% Eu		20	—	^{137}Cs (662 keV)	73 000	3.0	3.7	
	$CsSr_{0.92}Eu_{0.08}I_3$	VGF	—	457	^{137}Cs (662 keV)	65 000	3.3	5.9	204
	$KCaI_3$:0.5% Eu	BS	43 096	—	^{137}Cs (662 keV)	59 100	—	~4	211
	$KCaI_3$:3% Eu	BS	16	466	^{137}Cs (662 keV)	72 000	1.06	3	189
					^{57}Co (122 keV)	—	—	6.1	
	$RbCaBr_3$:7% Eu	BS	115	436	^{137}Cs (662 keV)	43 000	2.8	4.0	72
	$CsSrBr_3$:5% Eu	BS	125	430	^{137}Cs (662 keV)	55 600	2.16	5.2	212
	$CsSrBr_3$:5% Eu	BS	125	437	^{137}Cs (662 keV)	55 000	—	5.6	213
	$KCa_{0.8}Sr_{0.2}I_3$:0.5% Eu	BS	88 357	472	^{137}Cs (662 keV)	51 000	2.37	4.1	190
					^{57}Co (122 keV)	—	—	7.9	
	$CsSrBrI_2$:7% Eu	BS	50	449	^{137}Cs (662 keV)	65 300	1.8	3.4	206
	$CsCaBrI_2$:7% Eu		50	452	^{137}Cs (662 keV)	51 800	2.1	3.8	
	$CsSrClBr_2$:10% Eu		468	441	^{137}Cs (662 keV)	35 100	3.5	3.9	
	$CsSrCl_3$: 0.5% Ce	BS	9	365	^{137}Cs (662 keV)	8600	0.626	7.2	214
	$KCa_{0.835}Sr_{0.165}I_3$:3% Eu	BS	64	470	^{137}Cs (662 keV)	74 000	1.06	2.5	215
					^{57}Co (122 keV)	—	—	5.9	
					^{241}Am (59.5 keV)	—	—	8.0	
ABX_3	$MAPbBr_{0.05}Cl_{2.95}$	ITC	—	—	^{137}Cs (662 keV)	18 000	0.00014	10.5	216
(Other)	$TlMgCl_3$	BS	16	405	^{137}Cs (662 keV)	46 000	0.350	5	217
	$TlCaI_3$	BS	28	533	^{137}Cs (662 keV)	42 200	0.200	6.2	138
	$TlMgCl_3$	—	396	409		30 600	0.449	3.7	
	$TlCaCl_3$	BS	—	425	^{137}Cs (662 keV)	30 600	0.727	5	218

creates extra radiative recombination channels, thus improving the general performance of the scintillator. The co-doping strategy is another effective way to improve the performance of scintillators. W. Wolszczak and associates adopted a co-doping approach and developed a $CsBa_2I_5$ scintillator with 2% europium and 1% samarium.[221] The scintillator showed an LY of 45 000 photons per MeV and ER of 3.2% upon 662 keV gamma radiation. By means of emission source analysis, they discovered that the 5d-4f transition of Sm^{2+} at 755 nm accounted for 95% of the light emission; a minor contribution came from Eu^{2+}, emitting weakly around 430 nm. This work emphasizes the main influence of Sm^{2+} in the scintillation process and the complementary effect of Eu^{2+} in the general performance of the material.

Another strategy for optimizing the performance of scintillators involves composition engineering within the AB_2X_5 framework by maintaining a constant doping concentration. The prominent research group L. Stand and colleagues employed this approach to enhance the radiation detection performance of $RbSr_2Br_5$ doped by 2.5% europium.[68] By replacing bromine with iodine and by keeping the doping concentration constant, they developed a modified scintillator named $RbSr_2I_5$:Eu 2.5%. This modification led to significant performance improvements, including an increase in LY from 64 700 photons per MeV to 90 400 photons per MeV and an improvement in ER from 4% to 3% when exposed to 662 keV radiation from a ^{137}Cs source. This demonstrates the effectiveness of composition engineering in enhancing the properties of scintillators without altering the dopant concentration. In addition, the better performance might be attributed to the fact that the stopping power is increased by inserting iodine also. A similar approach has been used to enhance the performance of the KBa_2I_5:Eu 4% scintillator. By substituting barium with strontium and maintaining the same dopant concentration, the research group improved the LY of the modified scintillator (KSr_2I_5:Eu 4%) from 90 000 photons per MeV to 94 000 photons per MeV when it was subjected to 662 keV radiation (^{137}Cs) with 2.4% ER.[198,222] Similarly, by simply replacing potassium in the KBa_2I_5:Eu 4% scintillator, a research group achieved an enhancement in LY from 90 000 photons per MeV to 102 000 photons per MeV.[226] These studies underscore that by strategically applying compositional engineering at various sites within the scintillator structure AB_2X_5, researchers can achieve the optimal performance from the material.

The non-proportionality in the performance of AB_2X_5 compounds has been investigated by various researchers although studies are still limited on these compounds. Notwithstanding these endeavors, issues remain prevalent in AB_2X_5 perovskite systems. For example, the research team of L. Stand explored the non-linearity in the scintillator performance of KSr_2Br_5:Eu 5% under various levels of energy.[193] The findings revealed that the device achieved an ER of 3.5% when it was subjected to 662 keV energy emitted from a ^{137}Cs source. Alternatively, a comparatively lower ER of 6.7% was recorded when the same device was subjected to 122 keV energy emitted from a ^{57}Co source. Additionally, when the device was exposed to ^{241}Am (59.5 keV), an ER of 7.9% was noted. The results in ER show performance differences, which indicate a non-proportional response from the scintillator. Despite this, the research group asserted that within the measured gamma-ray energy range of 59 keV to 662 keV, there was a minimal deviation of about ±4% in the LY per unit energy. A separate study found that substituting bromine with iodine and fine-tuning the dopant concentration improved both the LY and ER.[222] The device with KSr_2I_5:Eu 4% demonstrated the highest LY of 94 000 photons per MeV and impressive ER of 2.4% when it was exposed to ^{137}Cs (662 keV). However, ERs of 5.7% and 7.2% were observed for ^{57}Co (122 keV) and ^{241}Am (59.5 keV), respectively. In the linearity test, the devices were excited with energies ranging from 14 keV to 1275 keV and minimal variation in LY within 3% across the entire energy range was observed. Another prominent research team focused on the scintillation performance of $CsBa_2I_5$:Eu 4% in the presence of frequently used radio isotopes.[226] The performance metrics indicate that the LY and ER of the devices increased in the range of 2600 photons per MeV to 198 000 photons per MeV and 21.3% to 1.8%, respectively, due to the change in the excitation energy from 18 keV to 1332 keV. In addition, the device exhibited a better performance for higher energy spectroscopy. Particularly, under the sources of ^{60}C o(1173 keV), ^{22}Na (1274 keV) and ^{60}Co (1332 keV), the LY of 174 600 photons per MeV, 190 000 photons per MeV and 198 000 photons per MeV and ER of 2.1%, 1.9% and 1.8% were observed, respectively. In addition, excited by the popular source ^{137}Cs (662 keV), the device shows a high LY of 102 000 photons per MeV with an ER of 2.55%. This trend implies a strong scintillation response over a broad energy range. A few promising perovskite scintillators along with their performance metrics are summarized in Table 2 and SI Table S2.

6.3. A_4BX_6 perovskite scintillators

A_4BX_6 is another zero-dimensional framework of perovskites, which is composed of a 4 : 1 ratio of alkali (AX) and alkaline earth metal halides (BX_2). In an effort of advancing zero-dimensional perovskite materials, the prominent research group led by L. Stand developed Cs_4CaI_6 with 4% Eu doping by means of reliable Bridgman–Stockbarger method and evaluated its performance metrics.[227] They reported an LY of 51 800 photons per MeV and ER of 3.6% under exposure to ^{137}Cs (662 keV). To further enhance the performance of scintillators, they employed compositional engineering by substituting calcium with the iso-valent element strontium. This modification resulted in significant improvements in the performance of the new Cs_4SrI_6:Eu 4% device including a higher LY of 62 300 photons per MeV, better ER of 3.3%, and faster scintillation decay time of 1.9 μs compared to its predecessor. These findings underscore the potential of these materials for high-resolution gamma-ray spectroscopy, and Cs_4SrI_6:Eu 4% emerging as the most efficient and promising scintillator. Later, Rutstrom *et al.* explored the effects of europium doping concentration on the scintillation performance under ^{137}Cs (662 keV) excitation of Cs_4SrI_6 and Cs_4CaI_6 devices developed *via* the Bridgman-Stockbarger approach.[70] Due to the enhanced doping

Table 2 Performance metrics from AB_2X_5 perovskite scintillators under various concentrations of dopants and varying gamma-ray energy

Material		Crystal growth method	Volume (mm^3)	Emission wavelength (nm)	Source	LY photons per MeV	Decay time (μs)	ER (%)	Ref.
AB_2X_5	$RbSr_2Br_5$:1% Eu	BS	154	423	^{137}Cs (662 keV)	58 000	0.8	3.9	191
	$RbSr_2Br_5$:3% Eu			431		73 000	1	4.1	
	$RbSr_2Br_5$:5% Eu			433		73 000	1.18	3.9	
	$RbSr_2Br_5$:7% Eu			438		71 000	1.22	4.0	
	$RbSr_2I_5$:1% Eu			438		74 000	0.7	3.5	
	$RbSr_2I_5$:5% Eu			444		90 000	1	2.9	
	$RbSr_2I_5$:7% Eu			445		89 000	1.1	2.8	
	$RbSr_2Br_5$:2.5% Eu	BS	37	429	^{137}Cs (662 keV)	64 700	0.78	4.0	68
	$RbSr_2I_5$:2.5% Eu			445		90 400	0.89	3.0	
	$CsBa_2I_5$:0.5% Eu	BS	30	430	^{137}Cs (662 keV	62 000		5.1	35
	$CsBa_2I_5$:5% Eu		50	435	^{137}Cs (662 keV)	80 000	~1	2.3	
					^{241}Am(59.5 keV)	—	—	7.5	
	KSr_2Br_5:5% Eu	BS	24	427	^{137}Cs (662 keV)	75 000	1.07	3.5	193
					^{57}Co (122 keV)	—	—	6.7	
					^{241}Am (59.5 keV)	—	—	7.9	
	KSr_2I_5:4% Eu	BS	2	445	^{137}Cs (662 keV)	94 000	0.99	2.4	222
			8		^{57}Co (122 keV)	—	—	5.7	
			8		^{241}Am (59.5 keV)	—	—	7.2	
	$RbBa_2I_5$:3% Eu	BS	226	436	^{137}Cs (662 keV)	58 200	0.800	8.18	223
	$LiSr_2I_5$:3% Eu	BS	3619	497	^{137}Cs (662 keV)	60 000	1.331	3.5	192
	$LiCa_2I_5$:Eu			472		90 000	1.416	5.6	
	$LiSr_2Br_5$:Eu			407, 476		32 000	1418	6.1	
	KSr_2I_5:0.5% Eu	BS	—	448	^{137}Cs (662 keV)	—	—	3.5	224
					^{57}Co (122 keV)	—	—	6.5	
	KSr_2I_5:2% Eu	BS	12	—	^{137}Cs (662 keV)	87 900	0.85	2.9	194
					^{57}Co (122 keV)	—	—	5.5	
					^{241}Am (59.5 keV)	—	—	7.8	
	KBa_2I_5:4% Eu	BS	4	444	^{137}Cs (662 keV)	90 000	0.91	2.4	198
					^{241}Am (59.5 keV)	—	—	7.6	
	KSr_2I_5: 4% Eu	BS	2	445	^{137}Cs (662 keV)	94 000	0.99	2.4	222
			8		^{57}Co (122 keV)	—	—	5.7	
			8		^{241}Am (59.5 keV)	—	—	7.2	
	KSr_2I_5:4% Eu	BS	—	—	^{137}Cs (662 keV)	94 000	0.99	2.4	210
	KBa_2I_5:5% Eu		—	—		84 000	0.91	2.6	
	$CsBa_2Br_5$:2% Eu	—	—	—	—	91 800	1.26	—	225
	$CsBa_2I_5$:4% Eu	BS	10	435, 466	^{137}Cs (662 keV)	102 000	1.20	2.55	226
					^{241}Am(59.5 keV)	9000	—	8.1	
					^{133}Ba(81 keV)	12 300	—	7.2	
					^{133}Ba (303 keV)	48 600	—	3.7	
					^{133}Ba(356 keV)	53 250	—	3.3	
					^{133}Ba (384 keV)	57 400	—	3.1	
					^{22}Na (511 keV)	76 350	—	2.9	
					^{60}Co(1173 keV)	174 600	—	2.1	
					^{22}Na(1274 keV)	190 000	—	1.9	
					^{60}Co(1332 keV)	198 000	—	1.8	
	$CsBa_2I_5$:2% Eu; 1% Sm	BS	—	755, 430	^{137}Cs (662 keV)	45 000	2.1	3.2	221

concentration of Eu in Cs_4SrI_6, the LY increased from 23 000 photons per MeV at 0.5% Eu dopant to 71 000 photons per MeV at 7% Eu along with improved ER from 6.6% to 3.2%. Similarly, Cs_4CaI_6:Eu showed an increased LY from 22 000 photons per MeV at 0.5% to 69 000 photons per MeV at 7% and improved ER from 4.8% to 3.6%. The decay times remained relatively stable, ranging from 1.63 μs to 1.90 μs, indicating the minimal impact from the dopant concentration. These findings indicate that the LY is enhanced due to additional activators, which necessarily augment the radiation recombination centers. However, the

concentration of the activator should be optimized; otherwise, it would act as a self-absorber. They also examined the proportionality with respect to the excitation energy and observed a satisfactory performance, with the exception of the 0.5% Eu-doped Cs_4SrI_6 device at a lower energy. A subsequent study conducted by the same group introduced a new activator named ytterbium at different concentrations and evaluated the performance of both scintillators under ^{137}Cs (662 keV).[196] Their study revealed that the scintillator with Cs_4CaI_6 doped by 1% Yb attained an impressive LY of 43 000 photons per MeV and exhibited the optimal ER of 3.5%. Nonetheless, the decay time diminished with an increase in the Yb concentration. In the case of the Cs_4SrI_6 scintillator, the highest LY of 40 000 photons per MeV was noted with 3% Yb doping, whereas the optimal ER of 5.1% was attained with 1% Yb doping. In addition, the decay time exhibited a remarkable consistency across all concentrations for the Cs_4SrI_6 structure. Very recently, the prominent researcher Pestovich and colleagues investigated the scintillation properties of Rb_4CaBr_6:Eu with varying europium doping concentrations of 3%, 7%, and 9%.[72] Their study revealed that increasing the Eu doping concentration significantly enhanced the LY, from 21 000 photons per MeV at 3% to 71 000 photons per MeV at 9%, when the devices were subjected to ^{137}Cs (662 keV) excitation. However, this improvement came at the cost of increased decay times, which increased from 2.07 μs at 3% to 2.83 μs at 9%. The ER also improved slightly from 7.7% at 3% to 6.9% at 9%. Although this study did not pay attention to the response against higher energy and proportionality performance, it reflects that Eu works efficiently as an activator to enhance the radiative recombination centers. Several promising perovskite scintillators and their performance metrics are shown in Table 3.

6.4. A_2BX_4 perovskite scintillators

A_2BX_4 represents another distinct framework of perovskites characterized by its two-dimensional structure, consisting of a 2 : 1 ratio of alkali (AX) and alkaline earth metal halides (BX_2). In an effort to develop the A_2BX_4 perovskite framework, the prominent research group led by L. Stand developed an Eu-activated K_2BaI_4 scintillator for the first time *via* the Bridgman–Stockbarger method.[210] Throughout the synthesis process, the concentration of europium (Eu) was methodically adjusted between 5% and 10% to ascertain the ideal doping level for improving the scintillation efficacy. The optimization process revealed that a 7% concentration of Eu produced the most favorable outcomes. At the optimal doping concentration of 7% Eu, the K_2BaI_4:Eu crystals exhibited remarkable scintillation characteristics including the light output of roughly 57 000 photons per MeV and ER of 2.9% at 662 keV. The research examined the correlation between light output and the energy of the incoming radiation and reported that the light output increased proportionally with the radiation energy. In the case of γ-ray energies exceeding 100 keV, the light output was determined to be directly proportional to the deposited energy, exhibiting a minimal deviation of less than approximately 2%. Conversely, at energies below 50 keV, the crystals retained approximately 96% of their scintillation LY, demonstrating their efficacy in detecting low-energy radiation. This property is especially beneficial for applications necessitating sensitivity over a wide energy range. Numerous promising perovskite scintillators along with their performance metrics are displayed in Table 3.

6.5. Halide double perovskite scintillators

Initiating compositional engineering using various sized cations or anions in their respective sites in ABX_3 can result in the formation of a huge number of derivatives of PVSK materials. However, among them, $A_2B^+M^{3+}X_6$, called halide double perovskite (HDP) (given that its unit cell is twice that of lead halide perovskites), is more efficient and stable.[238,239] Using common X atoms at the octahedral vertices, a strong rigid link connects the B^+X_6 and $M^{3+}X_6$ octahedra.[240] Because of their possible uses in radiation detection and medical imaging, the study of scintillator materials, especially those based on $A_2B^+M^{3+}X_6$ structures, has been a major focus of attention. Usually, when using the Bridgman–Stockbarger approach, a proven method for producing premium single crystals, the performance of these materials is critically explained based on their key performance parameters including LY, ER, and decay time. As part of developing intrinsic HDP-based scintillators, various research groups have adopted alkali metal halides or monovalent metal halides in combination with trivalent metal halides. With decay times in the range of 181 ns to 350 ns, and ERs between 5.3% and 6.3%, intrinsic materials such $Tl_2NaScCl_6$ and Tl_2NaYCl_6 show moderate LYs ranging from 20 000 photons per MeV to 23 000 photons per MeV.[233–236] These materials offer a basis for comprehending the basic features of the $A_2B^+M^{3+}X_6$ family. Doping is another strategy to enhance LY by creating additional recombination centers. However, doping these materials with rare earth elements including cerium, has shown to greatly improve their scintillation characteristics. The prominent researcher J. Glodo and research team developed high-performance scintillators based on Ce doping in Cs_2NaLaI_6 at concentrations of 2%, 5%, and 10%.[229] The LYs were measured to be 39 000 photons per MeV, 46 000 photons per MeV, and 34 000 photons per MeV, respectively, and the light emission attributed to the d-f transitions of Ce^{3+} ions. Among them, the 5% Ce-doped Cs_2NaLaI_6 was identified as the optimized structure along with an ER of 5%. The non-proportionality of light output *versus* excitation energy for Cs_2NaLaI_6:5% Ce was investigated under exposure to gamma-ray sources (^{137}Cs, ^{22}Na, ^{57}Co, and ^{241}Am) in the energy range of 14.4 keV to 1274 keV. The photopeak positions were normalized to the incident energy and plotted relative to the 662 keV reference. The results demonstrated excellent linearity with deviations of less than ±5%. A slight deviation was observed only at lower energies (14 keV). This near-ideal linearity suggests that ER is primarily governed by photons statistics, with a calculated ER of 3.1% at 662 keV, highlighting the superior performance of the material. In a similar study, $Cs_2NaLaBr_3I_3$ doped with 5% Ce demonstrated an exceptional performance, with an LY of 58 000 photons per MeV, decay time

Table 3 Performance metrics of A_4BX_6, A_2BX_4 and $A_2BB'X_6$ perovskite scintillators under various dopant concentrations and varying gamma-ray energies

Material		Crystal growth method	Volume (mm^3)	Emission wavelength (nm)	Source	LY photons per MeV	Decay time (μs)	ER (%)	Ref.
A_4BX_6	Rb_4CaBr_6:3% Eu	BS	116	455	^{137}Cs (662 keV)	21 000	2.07	7.7	72
	Rb_4CaBr_6:7% Eu		—	456		63 000	2.77	7.5	
	Rb_4CaBr_6:9% Eu		—	457		71 000	2.83	6.9	
	Cs_4SrI_6:0.5% Eu	BS	27	460	^{137}Cs (662 keV)	23 000	1.73	6.6	70
	Cs_4SrI_6:3% Eu			460		57 000	1.74	3.9	
	Cs_4SrI_6:7% Eu			460		71 000	1.88	3.2	
	Cs_4CaI_6:0.5% Eu			462		22 000	1.63	4.8	
	Cs_4CaI_6:3% Eu			462		52 000	1.65	4.3	
	Cs_4CaI_6:7% Eu			462		69 000	1.90	3.6	
	Cs_4SrI_6:4% Eu	BS	8	467	^{137}Cs (662 keV)	62 300	1.9	3.3	227
	Cs_4CaI_6:4% Eu			467		51 800	2.1	3.6	
	Cs_4CaI_6:0.5% Yb	BS	125	446	^{137}Cs (662 keV)	30 000	3.50	4.6	196
	Cs_4CaI_6:1% Yb			446		43 000	3.08	3.5	
	Cs_4CaI_6:3% Yb			446		42 000	2.15	4.8	
	Cs_4SrI_6:0.5% Yb			446		27 000	2.04	9.2	
	Cs_4SrI_6:1% Yb			446		35 000	2.28	5.1	
	Cs_4SrI_6:3% Yb			—		40 000	2.11	5.5	
A_2BX_4	K_2BaI_4:7% Eu	BS	36	—	^{137}Cs (662 keV)	57 000	—	2.9	228
	K_2BaI_4:7% Eu	BS	4	448	^{137}Cs (662 keV)	63 000	0.720	2.9	198
$A_2BB'X_6$	Cs_2NaLaI_6:2% Ce	BS	—	—	^{137}Cs (662 keV)	39 000	—	—	229
	Cs_2NaLaI_6:5% Ce			—	458	46 000	—	5	
	Cs_2NaLaI_6:10% Ce			—	—	34 000	—	—	
	$Cs_2NaYBr_3I_3$:2% Ce	BS	9	—	^{137}Cs (662 keV)	41 000	0.056	3.5	210
	$Cs_2NaLaBr_3I_3$:5% Ce		98	—		58 000	0.078	3.3	
	$Tl_2LiGdCl_6$:10% Ce	BS	101	387	^{137}Cs (662 keV)	58 000	0.034	4.6	230
	$Tl_2LiGdCl_6$:1% Ce		101	387		45 700	—	—	
	$Tl_2LiGdBr_6$:10% Ce	BS	75	422	^{137}Cs (662 keV)	17 400	0.029	17	231
	Tl_2LiYCl_6:3% Ce	BS	864	435	^{137}Cs (662 keV)	26 000	0.431	4.2	232
	$(Cs,Tl)_2LiLaBr_6$:3% Ce	BS	—	—	^{137}Cs (662 keV)	—	0.529	3.4	200
	$Tl_2NaScCl_6$	BS	—	430	^{137}Cs (662 keV)	20 000	0.181	5.3	233
	Tl_2NaYCl_6	BS	25	390	^{137}Cs (662 keV)	23 000	0.350	6.3	234
	$Tl_2LiScCl_6$	BS	—	385	^{137}Cs (662 keV)	26 000	1.147	8.3	235
	$Tl_2LiGdBr_6$	BS	20	435	^{137}Cs (662 keV)	27 000	0.105	7.2	236
	Tl_2LiYCl_6:1% Ce	BS	—	—	^{137}Cs (662 keV)	30 500	0.459	4.8	237
	Tl_2LiYCl_6:10% Ce		—	—		11 000	0.560	18	

of 78 ns, and excellent ER of 3.3%.[210] These findings highlight that Ce doping not only enhances the LY but also contributes to shorter decay times and improved ER, underscoring its critical role in optimizing scintillator materials. A higher Ce doping content does not always result in an improved performance, according to systematic studies on doping concentrations. For instance, Tl_2LiYCl_6:Ce 10% shows a much smaller LY of 11 000 photons per MeV and a longer decay time of 560 ns than the 1% doped variant, with an LY of 30 500 photons per MeV and decay time of 459 ns.[237] This emphasizes the need of the optimizing doping levels to attain the intended scintillation characteristics. The research group of R. Hawrami *et al.* grew $(Cs,Tl)_2$-$LiLaBr_6$:3% Ce crystals with different Cs-to-Tl ratios to address the non-congruence issue in $Tl_2LiLaBr_6$:Ce.[200] The 50% Cs–50% Tl crystal grew as a single and crack-free crystal but exhibited a poor scintillation performance along with an ER of 6.3% at 662 keV, which is lower than that expected for $Cs_2LiLaBr_6$:Ce. Additionally, a dark last-to-freeze section was observed, likely due to thallium segregation during growth. To improve the performance, the Tl content was reduced, resulting in a 75% Cs–25% Tl crystal with better crystallinity, which was also single and crack-free. This composition demonstrated a significantly improved ER of 3.4% at 662 keV, which is comparable to that of $Cs_2LiLaBr_6$:Ce. Both samples exhibited radioluminescence peaks at 390 nm and 422 nm, and the decay time profiles of 81 ns and 529 ns, making it a more promising scintillator. All things considered, the methodical study of intrinsic and doped $A_2B^+M^{3+}X_6$ materials reveal that doping, especially with Ce, can greatly improve the scintillation characteristics. To reach the intended balance among LY, decay time, and ER, the dopant concentration and material composition must be carefully tuned. These findings also provide a lack of insightful extensive research on various HDP combinations with different activators, aiming to develop next-generation scintillator materials tailored for specific applications. Several promising perovskite scintillators along with their performance metrics are presented in Table 3 and SI Table S3.

7. Comparative study of various dimensional perovskite scintillators

Our research has explored high-dimensional to low-dimensional metal halide perovskite scintillators, especially comprised of alkali and alkaline earth metal halides as promising alternatives to traditional inorganic scintillators.[76,241] The unique quantum confinement effects and dielectric confinement in lower-dimensional perovskites enable precise tuning of their light absorption and emission properties.[42,63] This arises from the spatial isolation of metal halide octahedra, which are spaced apart by bulky cations. In these structures, the separated octahedral units behave similarly to discrete nanocrystals, leading to strong exciton localization.[43,88,197,242] As a result, these confined excitons predominantly undergo radiative recombination, contributing to efficient light emission. These advancements in low-dimensional scintillators offer potential applications in various fields, including medical imaging, homeland security, and high-energy physics.[243] Our investigation into perovskite scintillators reveals that their scintillation performance is strongly influenced by their structural dimensionality. Specifically, our analysis of 3D perovskites (ABX_3) shows that these detectors produce a high LY, which is greater than that of conventional scintillators such as CsI:Tl and NaI:Tl but to some extent, it is lower than their lower-dimensional perovskite counterparts.[69,111,222] Additionally, these 3D scintillators exhibit promising ER; however, their relatively slow decay times may limit their suitability for fast-timing applications. Notably, the $RbSrI_3$:Eu 5 mol% scintillator achieved the highest recorded LY of 78 700 photons per MeV and an ER of 2.8% when exposed to a ^{137}Cs (662 keV) gamma source, though it exhibited a decay time of 1.03 μs.[69] In contrast, a better performance was also observed in the $KCa_{0.835}Sr_{0.165}I_3$:Eu 3% scintillator, which showed a high LY of 74 000 photons per MeV, highest ER of 2.5%, and decay time of 1.06 μs under the same radiation source.[215]

In contrast to the 3D ABX_3 structures, the most extensively studied 2D perovskites with the AB_2X_5 configuration have demonstrated superior performances overall. These materials exhibited the highest LYs, best ERs, and shortest decay times among all dimensional variants investigated. Notably, the $CsBa_2I_5$:Eu 4% scintillator achieved an impressive LY of 198 000 photons per MeV and an ER of 1.8% under exposure to a ^{60}Co source (1332 keV). This study further highlighted this consistent response of this scintillator across a wide energy range from 303 keV to 1332 keV. Additionally, high-performing candidates include KSr_2I_5:Eu (4%), with an LY of 94 000 photons per MeV and ER of 2.4% under ^{137}Cs (662 keV); KBa_2I_5:Eu (4%) with 90 000 photons per MeV and 2.4% ER; and $CsBa_2I_5$:Eu (5%), delivering 80 000 photons per MeV and an ER of 2.3% under the same source.[35,198,222]

In contrast, the zero-dimensional perovskite structure (A_4BX_6) has been relatively less explored. Among this class, the most notable performer is Cs_4SrI_6:Eu (7%), which achieved an LY of 71 000 photons per MeV, ER of 3.2%, and decay time of 1.88 μs when tested under a ^{137}Cs (662 keV) source.[70] Another strong candidate is Cs_4CaI_6:Eu (7%), which delivered an LY of 69 000 photons per MeV, ER of 3.6%, and decay time of 1.90 μs under the same irradiation source.[70] Additionally, Cs_4SrI_6:Eu (4%) also showed a promising performance, with an LY of 62 300 photons per MeV, ER of 3.3%, and decay time of 1.90 μs, again under ^{137}Cs exposure.[227] Alternatively, the A_2BX_4 structure remains the least explored among the perovskite scintillator types. The best-performing material in this category is K_2BaI_4:Eu (7%), which demonstrated an LY of 63 000 photons per MeV, ER of 2.9%, and relatively fast decay time of 720 ns.[228] These comparative findings highlight the importance of tailoring the dimensionality and composition of perovskites to specific application requirements, whether for high-sensitivity spectroscopy or ultrafast particle detection. Further investigation into low-dimensional systems, particularly A_4BX_6 and A_2BX_4 phases, and mixed-dimensional structures could unlock enhanced scintillation properties and novel functional applications. However, according to the review of a few studies, it can be concluded that the thermal stability decreases with reduced

dimensionality, though a systematic study has not been reported to date.[206,227,247] Fig. 7, 8 and 9 present a comparative analysis of the LY, ER, and non-proportionality across scintillators of varying dimensionalities, respectively.

8. Comparative study with conventional scintillators

Commercially available scintillators including NaI(Tl), CsI:Tl, LYSO:Ce, and BGO stand out for their historical success and application in medical imaging, security screening, and nuclear science. However, each scintillator comes with trade-offs in terms of performance parameters including LY, decay time, and ER. The emergence of halide perovskite scintillators has advanced a new class of materials that is not only comparable but also in some cases surpasses these commercial standards. NaI:Tl scintillators are the most established radiation detectors having a moderate LY of approximately 42 000 photons per MeV and ER around of 5.4%.[170] However, although its decay time is very fast at only 234 ns, it is limited by the fact that it is hygroscopic and has a low ER. In addition, another widely used scintillator is CsI:Tl and it performs better in LY, reaching up to 87 000 photons per MeV, but with a relatively longer decay time of about 500 ns and better ER near 4.9%.[170] Furthermore, LYSO:Ce is recognized for its ultrafast response near to ~45 ns, but suffers from poor ER ranging between 8% to 20%, depending on its crystal quality and configuration.[248] Moreover, BGO is dense and robust but has one of the lowest LYs ranging from 8000 photons per MeV to 10 000 photons per MeV and poor ER, which is generally worse than 10%.[248]

In contrast, recent advancements in halide perovskite scintillators comprised of alkali and alkaline earth metal halides demonstrate significantly improved performances across

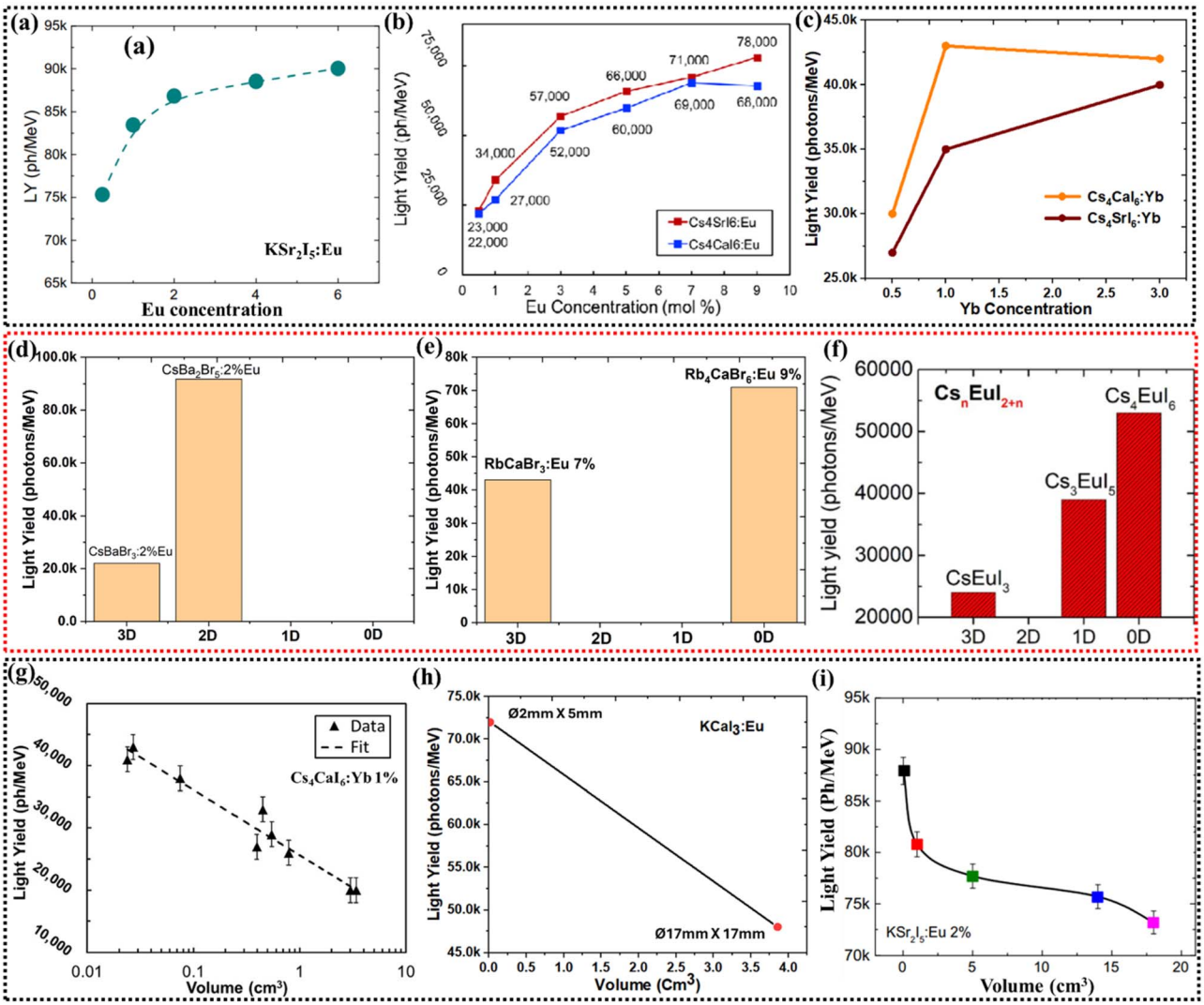

Fig. 7 Performance metric (light yield) of scintillation crystals as a function of (a–c) dopant concentration, (d–f) dimensional variation, and (g–i) thickness (volume). (a and i) Reprinted from ref. 194 with permission from Elsevier, Copyright 2018; (b) reprinted from ref. 244 with permission from Elsevier, Copyright 2019; (c and g) reprinted from ref. 196 with permission from Elsevier, Copyright 2020; (d) ref. 209 and 225; (e) ref. 72 and 245; (f) reprinted from ref. 197 with permission from RSC, Copyright 2018; and (h) reprinted from ref. 189 with permission from Elsevier, Copyright 2015.

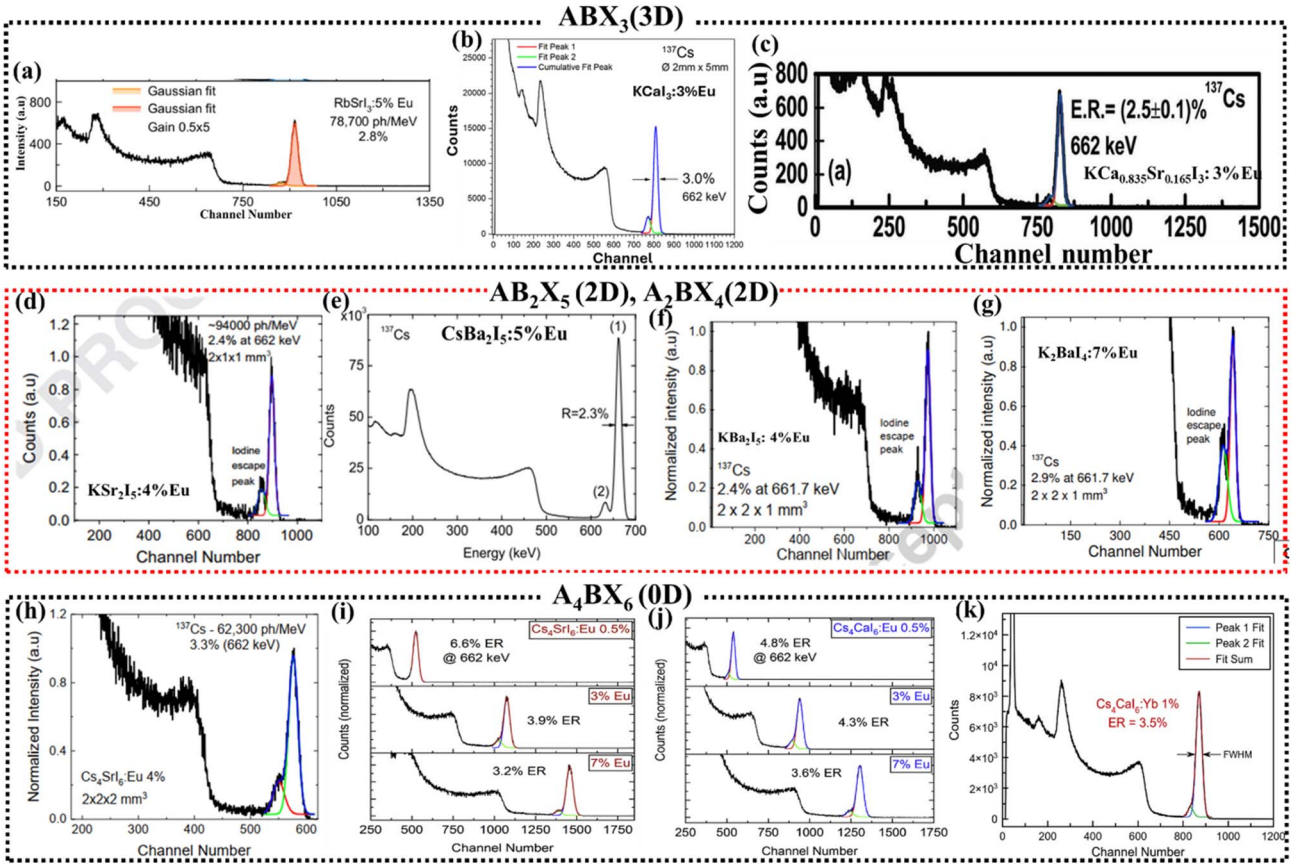

Fig. 8 (a–k) Energy resolution comparison of various scintillation crystals with different compositions, dopants, and dimensions. (a) Reprinted from Ref. 69 with permission from Elsevier, Copyright 2024; (b) reprinted from ref. 189 with permission from Elsevier, Copyright 2015; (c) reprinted from ref. 246 with permission from Wiley, Copyright 2016; (d) reprinted from ref. 222 with permission from Elsevier, Copyright 2015; (e) reprinted from ref. 35 with permission from Elsevier, Copyright 2014; (f and g) reprinted from ref. 198 with permission from Elsevier, Copyright 2016; (h) reprinted from ref. 227 with permission from Elsevier, Copyright 2018; (i and j) reprinted from ref. 244 with permission from Elsevier, Copyright 2019; and (k) Reprinted from ref. 196 with permission from Elsevier, Copyright 2020.

several key metrics. For example, europium-doped AB_2X_5 perovskites including KSr_2I_5 and $CsBa_2I_5$ have shown LYs of 94 000 photons per MeV and 102 000 photons per MeV under ^{137}Cs (662 keV), respectively, which not only surpass NaI:Tl and CsI:Tl but also exceed even the best-performing commercial scintillators.[222,226] These materials maintain excellent ER values between 2.4% and 2.55% respectively, a major improvement over their traditional counterparts.

In addition, $CsBa_2I_5$:Eu demonstrated the highest performance under high energy ^{60}Co(1332 keV) with LY of 198 000 photons per MeV and ER of 1.8%.[226] Additionally, their structural dimensionality plays a significant role in optimizing the scintillation properties. Similarly, 3D perovskites such as $KCa_{0.835}Sr_{0.165}I_3$:Eu and $RbSrI_3$:Eu exhibit high LYs of 74 000 photons per MeV to 78 700 photons per MeV and ERs as good as 2.5% to 2.8%.[69,215] However, their decay times are longer than that of commercial materials ranging from ns to μs (shown in Table 4). Meanwhile, 0D perovskites such as Cs_4SrI_6:Eu demonstrate slightly lower performances, with LYs of around 71 000 photons per MeV and ER near 3.2%.[70] However, they show better performances than NaI:Tl and CsI:Tl. Another promising composition is K_2BaI_4:Eu, which exhibits a balanced performance with an LY of around 70 000 photons per MeV, ER of 2.9%, and decay time near 720 ns.[228] These values make it highly competitive with commercial scintillators and indicate its strong potential for practical deployment.

The non-proportional performances between commercial and perovskite scintillators over a broad gamma energy range are illustrated in Fig. 9. Traditional scintillators including CsI:Na and NaI:Tl display significant non-proportionality, where their LY deviates notably from linearity.[170,249] This behavior underlines the constraints of these materials for precise spectroscopic applications, where a proportional response is essential. Conversely, LSO:Ce and LYSO:Ce both display a steadily increasing LY with gamma energy. LYSO:Ce performs better, with approximately 35% non-proportionality compared to 42% from LSO:Ce.[250] This improved proportionality is one of the reasons behind the superior ER of LYSO:Ce. In contrast, halide perovskite scintillators containing Cs_4CaI_6:Eu and Cs_4SrI_6:Eu show that the concentration of Eu significantly impacts their LY response.[70] Lower concentrations (0.5%) result in more proportional responses for the Cs_4CaI_6:Eu scintillator,

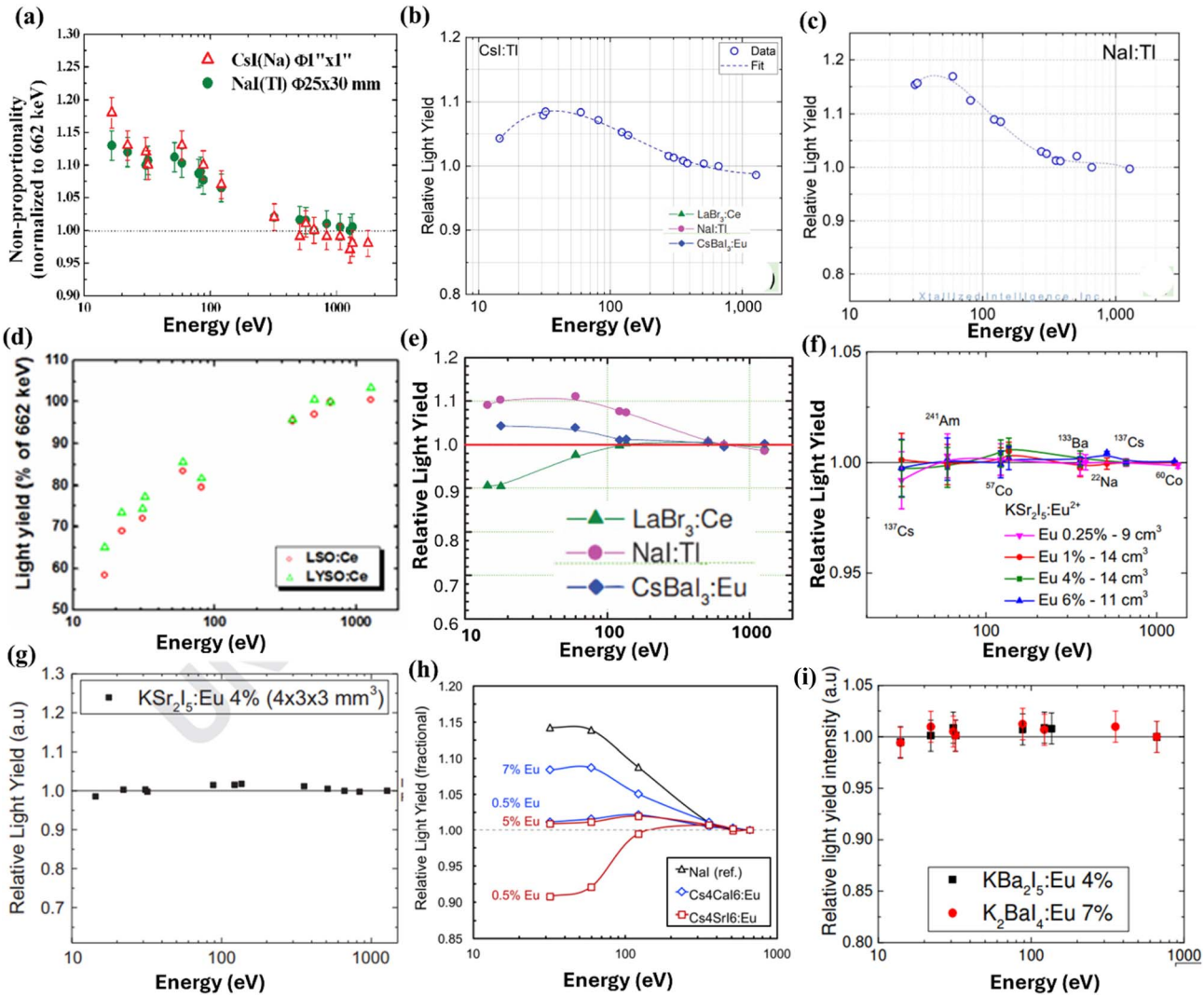

Fig. 9 (a–i) Comparison of the non-proportional (relative light yield) behavior under various range of energies between conventional scintillators and perovskite-based scintillators with varying dimensions. The data are standardized to the light yield measured at 662 keV from a ^{137}Cs source. (a) Reprinted from ref. 249 with permission from IEEE, Copyright 2015; (b and c) reprinted from ref. 170 with permission from MDPI, Copyright 2022; (d) reprinted from ref. 250 with permission from Elsevier, Copyright 2012; (e) reprinted from ref. 209 with permission from IEEE, Copyright 2011; (f) reprinted from ref. 194 with permission from Elsevier, Copyright 2018; (g) reprinted from ref. 222 with permission from Elsevier, Copyright 2015; (h) reprinted from ref. 244 with permission from Elsevier, Copyright 2019; and (i) reprinted from ref. 198 with permission from Elsevier, Copyright 2016.

whereas higher concentrations (5%) are more effective for the Cs_4SrI_6:Eu scintillator. The most promising performance is observed in europium-doped materials including KSr_2I_5:Eu, KBa_2I_5:Eu, and KBa_2I_5:Eu.[194,198,251] These scintillators demonstrate nearly ideal LY proportionality across the full gamma energy spectrum, with minimal variation from a constant response. This behavior signifies their capability for gamma-ray detection with high-resolution over a broad energy range, as they overcome one of the fundamental limitations named non-proportionality. In summary, this comparative study underscores the remarkable progress of halide perovskite scintillators comprised of alkali and alkaline earth metal halides, particularly in achieving superior LY and ER and non-proportionality over traditional commercial materials.

Alternatively, limited studies have focused extensively on the moisture stability of newly developed scintillator materials derived from alkali halides and alkaline metal halides. However, it is apparent from existing data that many of them demonstrate significantly higher vulnerability to moisture compared to traditional scintillators such as NaI and SrI_2. For example, as shown in Fig. 10, NaI(Tl) consistently demonstrates minimal weight change under humid conditions, which indicates its superior moisture resistance.

In contrast, perovskite materials including $RbCaBr_3$, Rb_4CaBr_6, and $CsSr_xBa_{1-x}I_3$:Eu display much higher weight changes, which reflect how much they are susceptible to moisture. However, some structures including $CsCaCl_3$:Eu exhibit better moisture resistance. Moreover, zero-dimensional

Table 4 Comparative performance metrics of perovskite scintillators to those of traditional scintillators

Material	Source	LY (photons per MeV)	Decay time (μs)	ER (%)	Ref.
NaI(Tl)	^{137}Cs (662 keV)	42 000	0.234	5.4	170
CsI:Tl	^{137}Cs (662 keV)	87 000	0.500	4.9	
$Lu_{1.95}Y_{0.05}SiO_5$:Ce	^{137}Cs (662 keV)	39 900		8.2	250
Lu_2SiO_5:Ce	^{137}Cs (662 keV)	35 900		10.6	
BGO		8000–10 000	0.300	9.7–16	248
LYSO(Ce)		30 000–33 000	0.045	8–20%	
CsI(Na)		38 000–44 000	0.630	5.8	
CsF	^{137}Cs (662 keV)	1900	0.002–0.004	19	252
BaF_2		1430	0.0008	10	130
$CaWO_4$	^{137}Cs (662 keV	4800	6.800	6.6	253
$CdWO_4$		19 700	0.104	6.5	21 and 254
$RbSrI_3$:5% Eu	^{137}Cs (662 keV)	78 700	1.03	2.8	69
$KCa_{0.835}Sr_{0.165}I_3$:3% Eu	^{137}Cs (662 keV)	74 000	1.060	2.5	215
$CsBa_2I_5$:5% Eu	^{137}Cs (662 keV)	80 000	~1	2.3	35
KSr_2I_5:4% Eu	^{137}Cs (662 keV)	94 000	0.990	2.4	222
KBa_2I_5:4% Eu	^{137}Cs (662 keV)	90 000	0.910	2.4	198
$CsBa_2I_5$:4% Eu	^{137}Cs (662 keV)	102 000	1.200	2.55	226
	^{60}Co (1332 keV)	198 000		1.8	
Cs_4SrI_6:7% Eu	^{137}Cs (662 keV)	71 000	1.88	3.2	70
Cs_4SrI_6:4% Eu	^{137}Cs (662 keV)	62 300	1.9	3.3	227
K_2BaI_4:7% Eu	^{137}Cs (662 keV)	63 000	0.720	2.9	198

perovskites achieve better moisture resistance compared to their 3D counterparts, even close to some conventional scintillators (shown in Fig. 10f). Therefore, when aiming for commercial viability and large-scale application, it is necessary to prioritize enhancing the environmental stability of these materials. Without improvements, their prospective as replacements for traditional scintillators remains limited due to their compromised performances under humid conditions.

9. Economic viability of perovskite-based scintillators compared to conventional commercial scintillators

High-bandgap perovskite materials, *i.e.*, materials derived from alkali and alkaline earth metal halides including $CsSrI_3$, $KCaI_3$, Cs_4CaBr_6, and $CsCa_2Br_5$, have recently emerged as promising candidates for scintillator and associated applications. In addition to their scintillation properties, these materials offer economic advantages over conventional scintillators. The raw materials used in their synthesis, including cesium bromide, strontium iodide, calcium bromide, and potassium iodide, are generally more abundant and less expensive than the rare-earth based compounds required for traditional commercial scintillators including $LaBr_3$:Ce, LYSO:Ce, and Gd_2O_3:Eu (**https://www.sigmaaldrich.com**). For example, materials like $LaBr_3$, Lu_2O_3, and Eu_2O_3 are costly due to the scarcity and processing difficulty of rare-earth elements (**https://www.sigmaaldrich.com**). Another key benefit of halide perovskite-related compounds lies in their relatively low melting points, especially compared to oxide-based scintillation materials. Most alkali halides and alkaline earth metal halides exhibit melting points below 1000 °C, with the exception of fluorine-containing compounds (**https://www.webelements.com/caesium/compounds.html**). In contrast, the compounds in traditional oxide scintillators containing Lu_2O_3, Y_2O_3, SiO_2, CeO_2, *etc.* possess significantly higher melting points, often up to 2700 °C, making them expensive to grow *via* melt-based crystal growth techniques (**https://www.webelements.com/caesium/compounds.html**). Furthermore, single crystals from low-bandgap halide perovskites have already been successfully synthesized using low-temperature solution-based growth methods such as inverse-temperature crystallization, slow solvent evaporation, temperature-lowering crystallization, and antisolvent vapor-assisted crystallization for radiation detection.[55] These methods can be adapted for the growth of high-bandgap perovskite single crystals, which offers substantial reductions in manufacturing costs by avoiding high-temperature processing. Overall, perovskite-based scintillators have a very bright economic future because of their potential to drastically reduce manufacturing costs through solution processability, easily accessible precursors, and less energy-intensive manufacture. Their outstanding performance-to-cost ratio and superior intrinsic scintillation qualities further improve their value proposition.

10. Perspective and prospective

Our studied halide perovskite-based scintillators have demonstrated impressive scintillation performances that surpasses many conventional commercial scintillators; however, their performances are still inferior compared to that of direct detectors including $CsPbBr_3$ with an ER of 1.4% or HPGe detectors.[256,257] In addition, current research shows the limited diversity of crystal growth techniques and most studies rely

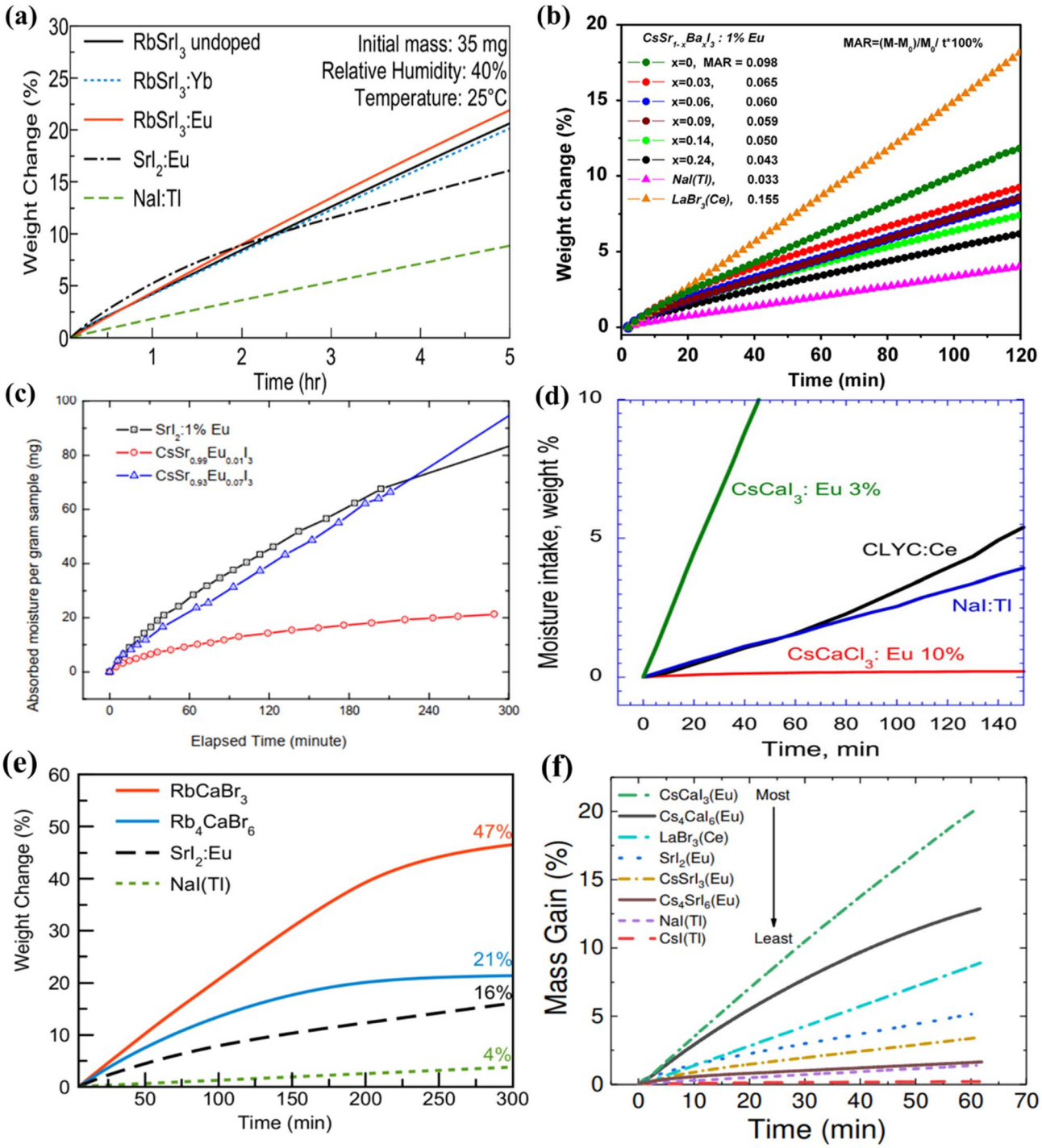

Fig. 10 (a–f) Comparison of the hygroscopicity of perovskite and conventional scintillators. (a) Reprinted from ref. 69 with permission from Elsevier, Copyright 2024. (b) Reprinted from ref. 247 with permission from Elsevier, Copyright 2013. (c) Reprinted from ref. 207 with permission from IEEE, Copyright 2010. (d) Reprinted from ref. 255 with permission from Elsevier, Copyright 2012. (e) Reprinted from ref. 245 with permission from IEEE, Copyright 2023. (f) Reprinted from ref. 227 with permission from Elsevier, Copyright 2018.

predominantly on the Bridgman–Stockbarger method. However, although the Bridgman-Stockbarger technique is an effective method for growing large-scale perovskite single crystals, with their size reaching inch-scale dimensions; however, it presents several limitations. The resulting crystals often suffer from non-uniform compositional distribution and localized structural defects, which can lead to inconsistencies in the performance of scintillators. Furthermore, this method is relatively expensive due to the high energy requirement during melting of compounds. A major challenge arises from the differing melting points of the constituent compounds. These disparities can cause one compound to solidify, while another

remains in the liquid phase, which reduces the likelihood of complete chemical reactions, resulting in phase segregation or compositional inhomogeneity. This makes it particularly difficult to achieve uniformity across the entire crystal. Therefore, future research should place greater emphasis on alternative growth methods, specifically solution-based techniques at room temperature, which can offer better control over phase purity and compositional uniformity throughout the crystal.

Current studies largely focus on structures including ABX_3 and AB_2X_5, whereas there remains substantial unexploited potential in less-explored configurations such as A_4BX_6 and A_2BX_4. Thus, future research should place emphasis on exploring a broader range of structural dimensionalities. In addition, by strategically manipulating the cation and anion compositions within these structures, it is possible to fine-tune their emission spectra for aligning with the peak sensitivity of PMTs, which enhances their overall performance. Furthermore, emission tunability, LY enhancement and tunable decay time can be achieved by incorporating suitable activator ions in the host crystal. The choice of activator plays a pivotal role in modulating the decay time, which facilitates either rapid or slow scintillation responses based on the application, such as swift timing for high-rate counting systems or sharp imaging system. However, a significant limitation in the current studies is the narrow focus on a limited set of activators, predominantly europium, with only few explorations of samarium and ytterbium. Other promising dopants, including Nd, Tb, Ce, Pr, Ga, In, Tl, Ge, Sn, Pb, Sb, Bi, Mn, Cr, and Fe, have been largely overlooked and should be the focus of further investigation.

Most studies on the performance of scintillators have been reported as the best performer or carried out performance tests under an energy of 662 keV from ^{137}Cs sources. This limited report on a broad energy range constrains our understanding of scintillator behavior across a broader spectrum. Although a few studies have investigated non-proportionality over a wide energy range and showed performances that surpasses conventional scintillators, comprehensive and systematic evaluations remain limited. Thus, to develop reliable and high-performance devices over a broad energy range, it is crucial to conduct detailed non-proportionality analyses including the sources of non-proportionality across a wide energy range given that it has a direct impact on ER. Although certain scintillators display fast decay times, others demonstrate slower decay times. While slower decay is normally less desirable for fast counting applications, it can be advantageous in specific imaging systems. However, none of the studies that were reviewed explored or capitalized on this prospective advantage. Moreover, long-term stability under environmental conditions and radiation hardness under various ranges of energy are essential for practical deployment. However, these aspects have not been thoroughly investigated, and it raises concerns about the real-world applicability of these scintillators. Finally, the lack of a unified and standardized evaluation framework for perovskite scintillators poses a significant challenge in benchmarking their performance consistently across different studies. As a result, this constraint hampers meaningful comparisons and limits the reproducibility of findings and slows down technological optimization. Ultimately, this creates a barrier in the progress of these scintillators toward commercial viability and integration into practical radiation detection systems.

Finally, in addition to the quantum confinement effect, nanophotonic strategies, particularly the Purcell effect, which can be activated by impinging quantum dot or nanoparticles into the host matrix,[258,259] have gained interest to improve the scintillator efficiency. However, they are typically restricted to the nanoscale or very thin films due to the localized nature of plasmonic field enhancements. Recently, for the first time, the research group led by M. Makowski overcame this limitation by dispersing 100 nm plasmonic nanoparticles (Ag-spheroidal and cuboidal in shape) into a 5-mm-thick bulk composite containing $CsPbBr_3$ perovskite nanocrystals.[259] The result is a significant boost in performance including an increase in the light emission intensity and decay rate by up to 3.2 and 4.2 times, respectively. This enhancement also translated to a measurable doubling of the scintillation yield under gamma-ray radiation from a ^{241}Am source. This type of approach can be implemented in the case of perovskite scintillators derived from alkali and alkaline metal halide perovskites to enhance their scintillation performances.

11. Conclusion

This review presents the recent progress in halide perovskite scintillators, particularly those derived from alkali and alkaline earth metal halides, covering a range of structures from higher-dimensional frameworks to low-dimensional configurations. In addition, this review begins with key figures of merit of scintillation, fundamental principles of radiation detection and methods for fabricating high-quality single crystals. This study also provides a comprehensive overview of gamma-ray spectroscopy-related research, detailing various strategies and approaches adopted to enhance the performance of scintillators. These perovskite-based scintillators are proving to be strong contenders to traditional inorganic scintillators, offering improved performances for gamma-ray detection. Among the various dimensional structures explored, ABX_3 and AB_2X_5 types have been more extensively studied, whereas A_4BX_6 and A_2BX_4 structures remain relatively underexplored. However, our investigation demonstrated that low-dimensional perovskite scintillators tend to outperform their higher-dimensional counterparts. Notably, $CsBa_2I_5$:Eu 4% demonstrated a superior performance across energies ranging from 303 keV to 1332 keV, achieving its best results under ^{60}Co (1332 keV) with an LY of 198 000 photons per MeV and ER of 1.8%. Although it showed a slightly lower ER of 2.55% at 662 keV with an LY of 102 000 photons per MeV, interestingly the same structure with different concentrations of Eu ($CsBa_2I_5$:Eu 5%) delivered the best ER of 2.3% at 662 keV under ^{137}Cs. In the ABX_3 category, the best performance was observed in $KCa_{0.835}Sr_{0.165}I_3$:3% Eu with an LY of 74 000 photons per MeV and ER of 2.5% at 662 keV. In the A_4BX_6 class, Cs_4SrI_6:Eu 7% achieved the best results with LY of 71 000 photons per MeV and 3.2% ER at 662 keV, while for AB_2X_4, K_2BaI_4:Eu 7% stood out with an LY of 63 000

photons per MeV and 2.9% ER under ^{137}Cs irradiation. Finally, this review also covers the perovskite configuration including ABX_3 and $A_2B^+M^{3+}X_6$, which integrate alkali or alkaline earth metal halides with other halide compounds, and highlights their potential with enhanced scintillation performance.

However, although halide perovskite-based scintillators have demonstrated impressive scintillation performances over many conventional commercial scintillators, they are still inferior compared to the performance of direct detectors including $CsPbBr_3$ with an ER of 1.4% under ^{137}Cs irradiation. Current crystal growth methods (crystallization from melting) suffer from high energy costs and challenges due to differing solidification points (temperatures) of the constituent compounds. Often they lead to phase segregation, compositional inhomogeneity, and structural defects, which affect their scintillator performance. Therefore, future research should place greater emphasis on alternative cost effective and room temperature crystal growth methods. Current studies give more attention to certain dimensional structures, leaving others comparatively understudied. Future exploration should focus on a broader range of structural dimensionalities and compositional tuning to optimize the emission spectra for better alignment with PMT sensitivity. In addition, emission tunability, LY enhancement, and tailored decay times can be attained by integrating an appropriate activator for specific scintillation applications. However, current investigations are limited by their narrow focus on a few activators such europium, while many promising dopants such as Nd, Tb, Ce, Pr, Tl, and In remain underexplored. Most studies focus on the performance of scintillators at 662 keV (^{137}Cs), which limits insight into their behavior across a broader energy spectrum. In addition, comprehensive non-proportionality analyses and assessments of their long-term stability and radiation hardness remain less explored. Thus, addressing these gaps is necessary for obtaining high-performance and reliable scintillators for real-world applications.

In summary, although perovskite scintillators show significant potential, their effective transition from the laboratory scale to industrial phase requires the development of alternative cost-effective and room-temperature crystal growth methods, expansion of structural and compositional engineering, exploration of a wider range of activators, deciphering the performance behavior under broad energy range, enhancing the stability and radiation hardness, and implementing standardized testing protocols.

Consent for publication

All authors of this work have agreed and are ready to sign the transfer of copyright which empowers the publisher to protect the work against unauthorized use and to maintain the integrity of the work from a bibliographical and archival standpoint.

Author contributions

Md. Helal Miah: literature review, designed and executed the study, data analysis and writing of the original draft; Mohammad Aminul Islam, Phannee Saengkaew, Arshid Numan, and Mohammad Aminul Islam: data curation, discussion, software and validation; Mayeen Uddin Khandaker: conceptualization, supervision, and reviewing and editing of the manuscript.

Conflicts of interest

The authors declare that they have no known competing financial interests or personal relationships that could have appeared to influence the work reported in this paper.

Data availability

All data are available in the manuscript.

Supplementary information is available. See DOI: **https://doi.org/10.1039/d5ra04980f**.

Acknowledgements

The Sunway University Scholarship support received by Md. Helal Miah is acknowledged. During the preparation of this work, the authors used some online services (such as Grammarly and Gemini) in order to improve language and readability. After using these tools/services, the authors reviewed and edited the content as needed, and they take full responsibility for the content of the publication.

References

1 R. F. Mould, The early history of X-ray diagnosis with emphasis on the contributions of physics 1895-1915, *Phys. Med. Biol.*, 1995, **40**(11), 1741, DOI: **10.1088/0031-9155/40/11/001**.

2 P. W. Frame, A history of radiation detection instrumentation, *Health Phys.*, 2005, **88**(6), 613–637, DOI: **10.1097/00004032-200506000-00008**.

3 J. L. Basdevant, Henri Becquerel: discovery of radioactivity, *BibNum*, 2008, DOI: **10.4000/bibnum.848**.

4 M. Nikl, Scintillation detectors for x-rays, *Meas. Sci. Technol.*, 2006, **17**(4), R37–R54, DOI: **10.1088/0957-0233/17/4/R01**.

5 L. H. Brixner, New X-ray phosphors, *Mater. Chem. Phys.*, 1987, **16**(3–4), 253–281, DOI: **10.1016/0254-0584(87)90102-7**.

6 P. Russer, Ferdinand Braun — A pioneer in wireless technology and electronics, *European Microwave Conference*, 2009, pp. 547–554, DOI: **10.23919/EUMC.2009.5296324**.

7 L. Ozawa and M. Itoh, Cathode Ray Tube Phosphors, *Chem. Rev.*, 2003, **103**(10), 3835–3855, DOI: **10.1021/CR0203490/ASSET/CR0203490.FP.PNG_V03**.

8 G. A. Morton, The scintillation counter story part II, *IEEE Trans. Nucl. Sci.*, 1975, **22**(1), 26–28, DOI: **10.1109/TNS.1975.4327608**.

9 Y. Wang, M. Li, Z. Chai, Y. Wang and S. Wang, Perovskite Scintillators for Improved X-ray Detection and Imaging,

Angew. Chem., Int. Ed., 2023, **62**(38), e202304638, DOI: 10.1002/ANIE.202304638.

10 P. Dorenbos, (INVITED) The quest for high resolution γ-ray scintillators, *Opt. Mater.:X*, 2019, **1**, 100021, DOI: 10.1016/J.OMX.2019.100021.

11 C. Dujardin, *et al.*, Needs, trends, and advances in inorganic scintillators, *IEEE Trans. Nucl. Sci.*, 2018, **65**(8), 1977–1997, DOI: 10.1109/TNS.2018.2840160.

12 P. Dorenbos, Fundamental limitations in the performance of Ce^{3+}-, Pr^{3+}-, and Eu^{2+}-activated scintillators, *IEEE Trans. Nucl. Sci.*, 2010, **57**, 1162–1167, DOI: 10.1109/TNS.2009.2031140.

13 T. Yanagida and T. Yamazaki, Inorganic scintillating materials and scintillation detectors, *Proc. Jpn. Acad., Ser. B*, 2018, **94**(2), 75–97, DOI: 10.2183/PJAB.94.007.

14 F. H. Marshall, J. W. Coltman and A. I. Bennett, The photomultiplier radiation detector, *Rev. Sci. Instrum.*, 1948, **19**(11), 744–770, DOI: 10.1063/1.1741156.

15 M. Blau and B. Dreyfus, The Multiplier Photo-Tube in Radioactive Measurements, *Rev. Sci. Instrum.*, 1945, **16**(9), 245–248, DOI: 10.1063/1.1770379.

16 R. Sherr, Scintillation Counter for the Detection of α-Particles, *Rev. Sci. Instrum.*, 1947, **18**(10), 767–770, DOI: 10.1063/1.1740842.

17 S. Naeem Ahmed, *Physics and Engineering of Radiation Detection | ScienceDirect*, Elsevier, 2015, https://www.sciencedirect.com/book/9780128013632/physics-and-engineering-of-radiation-detection#book-info.

18 C. Dujardin and M. Hamel, Introduction—Overview on Plastic and Inorganic Scintillators, in *Plastic Scintillators*, ed. M. Hamel, Springer, Cham, 2021, vol. 140, DOI: 10.1007/978-3-030-73488-6_1.

19 S. Schoppmann, Review of Novel Approaches to Organic Liquid Scintillators in Neutrino Physics, *Symmetry*, 2023, **15**(1), 11, DOI: 10.3390/SYM15010011.

20 S. Baccaro, *et al.*, Measurement of radiation damage on organic scintillators caused by gamma-rays and its recovery time, *Radiat. Phys. Chem.*, 1992, **40**(6), 585–587, DOI: 10.1016/1359-0197(92)90228-8.

21 F. Maddalena, *et al.*, Inorganic, Organic, and Perovskite Halides with Nanotechnology for High–Light Yield X- and γ-ray Scintillators, *Crystals*, 2019, **9**, 88, DOI: 10.3390/CRYST9020088.

22 I. Mouhti, A. Elanique and M. Y. Messous, Monte Carlo modelling of a NaI(Tl) scintillator detectors using MCNP simulation code, *J. Mater. Environ. Sci.*, 2017, **8**(12), 4560–4565, DOI: 10.26872/JMES.2017.8.12.481.

23 R. Hofstadter, The Detection of Gamma-Rays with Thallium-Activated Sodium Iodide Crystals, *Phys. Rev.*, 1949, **75**(5), 796–810, DOI: 10.1103/PHYSREV.75.796.

24 E. Monachesi, *et al.*, Comparative Evaluation of Cesium Iodide Scintillators Coupled to a Silicon Photomultiplier (SiPM): Effect of Thickness and Doping on the scintillators, *J. Phys.:Conf. Ser.*, 2017, **931**(1), 012013, DOI: 10.1088/1742-6596/931/1/012013.

25 M. da C. C. Pereira, T. M. Filho, J. R. Berretta and C. H. de Mesquita, Characteristics of the CsI:Tl Scintillator Crystal for X-Ray Imaging Applications, *Mater. Sci. Appl.*, 2018, **09**(2), 268–280, DOI: 10.4236/MSA.2018.92018.

26 S. Il Kwon, A. Gola, A. Ferri, C. Piemonte and S. R. Cherry, Bismuth germanate coupled to near ultraviolet silicon photomultipliers for time-of-flight PET, *Phys. Med. Biol.*, 2016, **61**(18), L38–L47, DOI: 10.1088/0031-9155/61/18/L38.

27 A. Lightstone, R. Mcintyre, R. Lecomte and D. Schmitt, A Bismuth Germanate-Avalanche Photodiode Module Designed for Use in High Resolution Positron Emission Tomography, *IEEE Trans. Nucl. Sci.*, 1986, **33**(1), 456–459, DOI: 10.1109/TNS.1986.4337142.

28 S. E. Derenzo and J. K. Riles, Monte Carlo Calculations of the Optical Coupling between Bismuth Germanate Crystals and Photomultiplier Tubes, *IEEE Trans. Nucl. Sci.*, 1982, **29**(1), 191–195, DOI: 10.1109/TNS.1982.4335825.

29 S. Yamamoto and H. Tomita, Comparison of light outputs, decay times, and imaging performance of a ZnS(Ag) scintillator for alpha particles, beta particles, and gamma photons, *Appl. Radiat. Isot.*, 2020, **168**(2), 109527, DOI: 10.1016/J.APRADISO.2020.109527.

30 S. Yamamoto, I. Aoki and T. Higashi, Optical fiber-based ZnS(Ag) detector for selectively detecting alpha particles, *Appl. Radiat. Isot.*, 2020, **169**(3), 109495, DOI: 10.1016/J.APRADISO.2020.109495.

31 S. A. Osseni, *et al.*, Gadolinium oxysulfide nanoparticles as multimodal imaging agents for T2-weighted MR, X-ray tomography and photoluminescence, *Nanoscale*, 2014, **6**(1), 555–564, DOI: 10.1039/C3NR03982J.

32 J. Santelli, *et al.*, Multimodal Gadolinium Oxysulfide Nanoparticles for Bioimaging: A Comprehensive Biodistribution, Elimination and Toxicological Study, *Acta Biomater.*, 2020, **108**(5), 261–272, DOI: 10.1016/j.actbio.2020.03.013.

33 I. Hossain, N. Sharip and K. Viswanathan, Efficiency and resolution of HPGe and NaI(Tl) detectors using gamma-ray spectroscopy, *Sci. Res. Essays*, 2012, **7**(1), 86–89, DOI: 10.5897/SRE11.1717.

34 F. Zhou, Z. Li, W. Lan, Q. Wang, L. Ding and Z. Jin, Halide Perovskite, a Potential Scintillator for X-Ray Detection, *Small Methods*, 2020, **4**(10), 2000506, DOI: 10.1002/SMTD.202000506.

35 M. S. Alekhin, D. A. Biner, K. W. Krämer and P. Dorenbos, Optical and scintillation properties of CsBa2I5:Eu2+, *J. Lumin.*, 2014, **145**, 723–728, DOI: 10.1016/J.JLUMIN.2013.08.058.

36 S. Stave, Germanium Detectors in Homeland Security at PNNL, *J. Phys.:Conf. Ser.*, 2015, **606**(1), 012018, DOI: 10.1088/1742-6596/606/1/012018.

37 M. H. Miah, *et al.*, Understanding the Degradation Factors, Mechanism and Initiatives for Highly Efficient Perovskite Solar Cells, *ChemNanoMat*, 2023, **9**(3), e202200471, DOI: 10.1002/CNMA.202200471.

38 Md. B. Rahman, N.- E-Ashrafi, Md. H. Miah, M. U. Khandaker and M. A. Islam, Selection of a compatible electron transport layer and hole transport layer for the mixed perovskite FA0.85Cs0.15Pb(I0.85Br0.15)3, towards achieving novel structure and

high-efficiency perovskite solar cells: a detailed numerical study by SCAPS-1D, *RSC Adv.*, 2023, **13**(25), 17130–17142, DOI: 10.1039/D3RA02170J.

39 A. Aftab and M. I. Ahmad, A review of stability and progress in tin halide perovskite solar cell, *Sol. Energy*, 2021, **216**, 26–47, DOI: 10.1016/J.SOLENER.2020.12.065.

40 N. Suresh Kumar and K. Chandra Babu Naidu, A review on perovskite solar cells (PSCs), materials and applications, *J. Materiomics*, 2021, **7**(5), 940–956, DOI: 10.1016/J.JMAT.2021.04.002.

41 H. Lin, C. Zhou, Y. Tian, T. Siegrist and B. Ma, Low-Dimensional Organometal Halide Perovskites, *ACS Energy Lett.*, 2018, **3**(1), 54–62, DOI: 10.1021/ACSENERGYLETT.7B00926/ASSET/IMAGES/LARGE/NZ-2017-00926N_0003.

42 M. H. Miah, M. U. Khandaker, M. B. Rahman, M. Nur-E-Alam and M. A. Islam, Band gap tuning of perovskite solar cells for enhancing the efficiency and stability: issues and prospects, *RSC Adv.*, 2024, **14**(23), 15876–15906, DOI: 10.1039/D4RA01640H.

43 F. Liu, *et al.*, Recent Progress in Halide Perovskite Radiation Detectors for Gamma-Ray Spectroscopy, *ACS Energy Lett.*, 2022, **7**(3), 1066–1085, DOI: 10.1021/ACSENERGYLETT.2C00031/ASSET/IMAGES/MEDIUM/NZ2C00031_0012.

44 F. Valipour, E. Yazdi, N. Torabi, B. F. Mirjalili and A. Behjat, Improvement of the stability of perovskite solar cells in terms of humidity/heat *via* compositional engineering, *J. Phys. D Appl. Phys.*, 2020, **53**(28), 285501, DOI: 10.1088/1361-6463/AB8511.

45 W. Gao, *et al.*, A-Site Cation Engineering of Metal Halide Perovskites: Version 3.0 of Efficient Tin-Based Lead-Free Perovskite Solar Cells, *Adv. Funct. Mater.*, 2020, **30**(34), 2000794, DOI: 10.1002/ADFM.202000794.

46 C. C. Stoumpos and M. G. Kanatzidis, The Renaissance of Halide Perovskites and Their Evolution as Emerging Semiconductors, *Acc. Chem. Res.*, 2015, **48**(10), 2791–2802, DOI: 10.1021/ACS.ACCOUNTS.5B00229/ASSET/IMAGES/MEDIUM/AR-2015-002292_0014.

47 C. J. Bartel, *et al.*, New tolerance factor to predict the stability of perovskite oxides and halides, *Sci. Adv.*, 2019, **5**(2), eaav0693, DOI: 10.1126/SCIADV.AAV0693/SUPPL_FILE/AAV0693_TABLE_S4.

48 L. Etgar, The merit of perovskite's dimensionality; can this replace the 3D halide perovskite?, *Energy Environ. Sci.*, 2018, **11**(2), 234–242, DOI: 10.1039/C7EE03397D.

49 C. Zhou, *et al.*, Lead-free perovskites and derivatives enable direct and scintillation-type X-ray detection, *Mater. Sci. Eng., R*, 2023, **156**(12), 100756, DOI: 10.1016/J.MSER.2023.100756.

50 Z. Li, F. Zhou, H. H. Yao, Z. Ci, Z. Yang and Z. Jin, Halide perovskites for high-performance X-ray detector, *Mater. Today*, 2021, **48**, 155–175, DOI: 10.1016/J.MATTOD.2021.01.028.

51 M. H. McKetty, The AAPM/RSNA Physics Tutorial for Residents: X-ray Attenuation, *Radiographics*, 1998, **18**(1), 151–163, DOI: 10.1148/RADIOGRAPHICS.18.1.9460114.

52 Y. Wang, Intuitive dimensional analyses of the energy and atomic number dependences of the cross sections for radiation interaction with matter, *J. Xray Sci. Technol.*, 2007, **15**(3), 169–175, DOI: 10.3233/XST-2007-00177.

53 D. R. White, An analysis of the Z-dependence of photon and electron interactions, *Phys. Med. Biol.*, 1977, **22**(2), 219, DOI: 10.1088/0031-9155/22/2/003.

54 H. Lusic and M. W. Grinstaff, X-ray-computed tomography contrast agents, *Chem. Rev.*, 2013, **113**(3), 1641–1666, DOI: 10.1021/CR200358S.

55 M. H. Miah, M. U. Khandaker, M. Aminul Islam, M. Nur-E-Alam, H. Osman and M. H. Ullah, Perovskite materials in X-ray detection and imaging: recent progress, challenges, and future prospects, *RSC Adv.*, 2024, **14**(10), 6656–6698, DOI: 10.1039/D4RA00433G.

56 M. Nikl and A. Yoshikawa, Recent R&D Trends in Inorganic Single-Crystal Scintillator Materials for Radiation Detection, *Adv. Opt. Mater.*, 2015, **3**(4), 463–481, DOI: 10.1002/ADOM.201400571.

57 W. Zhu, *et al.*, Low-dose real-time X-ray imaging with nontoxic double perovskite scintillators, *Light: Sci. Appl.*, 2020, **9**(1), 1–10, DOI: 10.1038/s41377-020-00353-0.

58 S. Cheng, A. Beitlerova, R. Kucerkova, M. Nikl, G. Ren and Y. Wu, Zero-Dimensional $Cs_3Cu_2I_5$ Perovskite Single Crystal as Sensitive X-Ray and γ-Ray Scintillator, *Phys. Status Solidi RRL*, 2020, **14**(11), 2000374, DOI: 10.1002/PSSR.202000374.

59 L. J. Xu, X. Lin, Q. He, M. Worku and B. Ma, Highly efficient eco-friendly X-ray scintillators based on an organic manganese halide, *Nat. Commun.*, 2020, **11**(1), 1–7, DOI: 10.1038/s41467-020-18119-y.

60 G. Blasse, Reviews: Scintillator Materials, *Chem. Mater.*, 1994, **6**(9), 1465–1475, DOI: 10.1021/CM00045A002/ASSET/CM00045A002.FP.PNG_V03.

61 A. Xie, *et al.*, Thermal Quenching and Dose Studies of X-ray Luminescence in Single Crystals of Halide Perovskites, *J. Phys. Chem. C*, 2018, **122**(28), 16265–16273, DOI: 10.1021/ACS.JPCC.8B03622/SUPPL_FILE/JP8B03622_SI_002.

62 K. Shibuya, M. Koshimizu, H. Murakami, Y. Muroya, Y. Katsumura and K. Asai, Development of ultra-fast semiconducting scintillators using quantum confinement effect, *Jpn. J. Appl. Phys.*, 2004, **43**(10), L1333, DOI: 10.1143/JJAP.43.L1333.

63 K. Shibuya, M. Koshimizu, K. Asai and H. Shibata, Quantum confinement for large light output from pure semiconducting scintillators, *Appl. Phys. Lett.*, 2004, **84**(22), 4370–4372, DOI: 10.1063/1.1756203.

64 J. M. Hoffman, *et al.*, From 2D to 1D Electronic Dimensionality in Halide Perovskites with Stepped and Flat Layers Using Propylammonium as a Spacer, *J. Am. Chem. Soc.*, 2019, **141**(27), 10661–10676, DOI: 10.1021/JACS.9B02846/SUPPL_FILE/JA9B02846_SI_010.

65 D. Li, Z. Xing, X. Meng, X. Hu, T. Hu and Y. Chen, Selection of Functional Spacer Cations for Efficient 2D/3D Perovskite Solar Cells, *CCS Chem.*, 2023, **5**(4), 71–801, DOI: 10.31635/CCSCHEM.023.202202409.

66 C. C. Stoumpos, *et al.*, Ruddlesden-Popper Hybrid Lead Iodide Perovskite 2D Homologous Semiconductors, *Chem. Mater.*, 2016, **28**(8), 2852–2867, DOI: 10.1021/ACS.CHEMMATER.6B00847/SUPPL_FILE/CM6B00847_SI_003.

67 L. Mao, C. C. Stoumpos and M. G. Kanatzidis, Two-Dimensional Hybrid Halide Perovskites: Principles and Promises, *J. Am. Chem. Soc.*, 2019, **141**(3), 1171–1190, DOI: 10.1021/JACS.8B10851/ASSET/IMAGES/MEDIUM/JA-2018-10851V_0014.

68 L. Stand, M. Zhuravleva, J. Johnson, M. Koschan, E. Lukosi and C. L. Melcher, New high performing scintillators: RbSr2Br5:Eu and RbSr2I5:Eu, *Opt. Mater.*, 2017, **73**, 408–414, DOI: 10.1016/J.OPTMAT.2017.08.013.

69 K. S. Pestovich, L. Stand, C. L. Melcher, E. Van Loef and M. Zhuravleva, Crystal growth of new high light yield halide perovskite scintillator RbSrI3, *J. Cryst. Growth*, 2024, **627**, 127540, DOI: 10.1016/J.JCRYSGRO.2023.127540.

70 D. Rutstrom, L. Stand, M. Koschan, C. L. Melcher and M. Zhuravleva, Europium concentration effects on the scintillation properties of Cs4SrI6:Eu and Cs4CaI6:Eu single crystals for use in gamma spectroscopy, *J. Lumin.*, 2019, **216**, 116740, DOI: 10.1016/J.JLUMIN.2019.116740.

71 A. Lindsey, W. McAlexander, L. Stand, Y. Wu, M. Zhuravleva and C. L. Melcher, Crystal growth and spectroscopic performance of large crystalline boules of CsCaI3:Eu scintillator, *J. Cryst. Growth*, 2015, **427**, 42–47, DOI: 10.1016/J.JCRYSGRO.2015.07.002.

72 K. S. Pestovich, L. Stand, E. Van Loef, C. L. Melcher and M. Zhuravleva, Crystal Growth and Characterization of Europium-Doped Rubidium Calcium Bromide Scintillators, *IEEE Trans. Nucl. Sci.*, 2023, **70**(7), 1370–1377, DOI: 10.1109/TNS.2023.3280733.

73 V. B. Mykhaylyk, H. Kraus and M. Saliba, Bright and fast scintillation of organolead perovskite MAPbBr3 at low temperatures, *Mater. Horiz.*, 2019, **6**(8), 1740–1747, DOI: 10.1039/C9MH00281B.

74 F. P. García de Arquer, D. V. Talapin, V. I. Klimov, Y. Arakawa, M. Bayer and E. H. Sargent, Semiconductor quantum dots: Technological progress and future challenges, *Science*, 2021, **373**(6555), DOI: 10.1126/SCIENCE.AAZ8541/ASSET/C3AC7CAD-9110-4FD1-85BA-03C145F887FC/ASSETS/IMAGES/LARGE/SCIENCE.AAZ8541-F6.

75 V. B. Mykhaylyk, *et al.*, Bright and fast scintillations of an inorganic halide perovskite CsPbBr3 crystal at cryogenic temperatures, *Sci. Rep.*, 2020, **10**(1), 1–11, DOI: 10.1038/s41598-020-65672-z.

76 Q. Xu, *et al.*, A solution-processed zero-dimensional all-inorganic perovskite scintillator for high resolution gamma-ray spectroscopy detection, *Nanoscale*, 2020, **12**(17), 9727–9732, DOI: 10.1039/D0NR00772B.

77 N. Kawano, *et al.*, Scintillating Organic–Inorganic Layered Perovskite-type Compounds and the Gamma-ray Detection Capabilities, *Sci. Rep.*, 2017, **7**(1), 1–8, DOI: 10.1038/s41598-017-15268-x.

78 M. Akatsuka, *et al.*, Development of scintillating 2D quantum confinement materials — $(C_6H_5C_2H_4NH_3)2Pb1-xSr_xBr_4$, *Nucl. Instrum. Methods Phys. Res., Sect. A*, 2020, **954**, 161372, DOI: 10.1016/J.NIMA.2018.10.050.

79 D. Onoda, *et al.*, Evaluation of scintillation properties of organic–inorganic perovskite compounds—$(C_6H_5C_2H_4NH_3)2Pb1-xNi_xBr_4$, *Jpn. J. Appl. Phys.*, 2022, **61**, SB1041, DOI: 10.35848/1347-4065/AC1487.

80 D. Onoda, *et al.*, Scintillation properties of $(C_6H_5C_2H_4NH_3)2Pb1\text{-}xSn_xBr_4$ crystals having two-dimensional quantum-well structures, *Opt. Mater.*, 2021, **114**, 111002, DOI: 10.1016/J.OPTMAT.2021.111002.

81 D. Onoda, *et al.*, Development of $(C_6H_5C_2H_4NH_3)2Pb1\text{-}xCd_xBr_4$ crystal scintillators with two-dimensional quantum-well structures, *J. Lumin.*, 2021, **237**, 118157, DOI: 10.1016/J.JLUMIN.2021.118157.

82 D. Onoda, *et al.*, Photoluminescence and scintillation properties of $(C_6H_5C_2H_4NH_3)2Pb1-xZn_xBr_4$ as a two-dimensional quantum-confined scintillator, *J. Mater. Sci.: Mater. Electron.*, 2020, **31**(23), 20798–20804, DOI: 10.1007/S10854-020-04592-0/METRICS.

83 B. Yang, *et al.*, Lead-Free Halide Rb_2CuBr_3 as Sensitive X-Ray Scintillator, *Adv. Mater.*, 2019, **31**(44), 1904711, DOI: 10.1002/ADMA.201904711.

84 S. Cheng, *et al.*, Non-Hygroscopic, Self-Absorption Free, and Efficient 1D $CsCu_2I_3$Perovskite Single Crystal for Radiation Detection, *ACS Appl. Mater. Interfaces*, 2021, **13**(10), 12198–12202, DOI: 10.1021/ACSAMI.0C22505/SUPPL_FILE/AM0C22505_SI_001.

85 S. Cheng, *et al.*, Ultrabright and Highly Efficient All-Inorganic Zero-Dimensional Perovskite Scintillators, *Adv. Opt. Mater.*, 2021, **9**(13), 2100460, DOI: 10.1002/ADOM.202100460.

86 M. D. Smith and H. I. Karunadasa, White-Light Emission from Layered Halide Perovskites, *Acc. Chem. Res.*, 2018, **51**(3), 619–627, DOI: 10.1021/ACS.ACCOUNTS.7B00433/ASSET/IMAGES/MEDIUM/AR-2017-00433V_0012.GIF.

87 M. D. Smith, A. Jaffe, E. R. Dohner, A. M. Lindenberg and H. I. Karunadasa, Structural origins of broadband emission from layered Pb–Br hybrid perovskites, *Chem. Sci.*, 2017, **8**(6), 4497–4504, DOI: 10.1039/C7SC01590A.

88 C. Zhou, *et al.*, Luminescent zero-dimensional organic metal halide hybrids with near-unity quantum efficiency, *Chem. Sci.*, 2018, **9**(3), 586–593, DOI: 10.1039/C7SC04539E.

89 W. Gao, *et al.*, One-Dimensional All-Inorganic $K_2CuBr_3$with Violet Emission as Efficient X-ray Scintillators, *ACS Appl. Electron. Mater.*, 2020, **2**(7), 2242–2249, DOI: 10.1021/ACSAELM.0C00414/SUPPL_FILE/EL0C00414_SI_001.

90 X. Zhao, *et al.*, All-Inorganic Copper Halide as a Stable and Self-Absorption-Free X-ray Scintillator, *J. Phys. Chem. Lett.*, 2020, **11**(5), 1873–1880, DOI: 10.1021/ACS.JPCLETT.0C00161/SUPPL_FILE/JZ0C00161_SI_001.

91 P. A. Rodnyi, Physical Processes in Inorganic Scintillators, *Physical Processes in Inorganic Scintillators*, 2020, DOI: 10.1201/9780138743352.

92 M.-H. Du, Using DFT Methods to Study Activators in Optical Materials, *ECS J. Solid State Sci. Technol.*, 2016, **5**(1), R3007–R3018, DOI: 10.1149/2.0011601JSS.

93 W. Ma, *et al.*, Highly Resolved and Robust Dynamic X-Ray Imaging Using Perovskite Glass-Ceramic Scintillator with Reduced Light Scattering, *Advanced Science*, 2021, **8**(15), 2003728, DOI: 10.1002/ADVS.202003728.

94 K. A. Dagnall, A. M. Conley, L. U. Yoon, H. S. Rajeev, S. H. Lee and J. J. Choi, Ytterbium-Doped Cesium Lead Chloride Perovskite as an X-ray Scintillator with High Light Yield, *ACS Omega*, 2022, **7**(24), 20968–20974, DOI: 10.1021/ACSOMEGA.2C01712/ASSET/IMAGES/LARGE/AO2C01712_0004.

95 D. Yuan, Air-Stable Bulk Halide Single-Crystal Scintillator $Cs_3Cu_2I_5$ by Melt Growth: Intrinsic and Tl Doped with High Light Yield, *ACS Appl. Mater. Interfaces*, 2020, **12**(34), 38333–38340, DOI: 10.1021/ACSAMI.0C09047/SUPPL_FILE/AM0C09047_SI_001.

96 L. Stand, *et al.*, Crystal growth and scintillation properties of pure and Tl-doped Cs3Cu2I5, *Nucl. Instrum. Methods Phys. Res., Sect. A*, 2021, **991**, 164963, DOI: 10.1016/J.NIMA.2020.164963.

97 C. Rodà, *et al.*, Understanding Thermal and A-Thermal Trapping Processes in Lead Halide Perovskites Towards Effective Radiation Detection Schemes, *Adv. Funct. Mater.*, 2021, **31**(43), 2104879, DOI: 10.1002/ADFM.202104879.

98 M. Nikl, V. V. Laguta and A. Vedda, Complex oxide scintillators: Material defects and scintillation performance, *Phys. Status Solidi B*, 2008, **245**(9), 1701–1722, DOI: 10.1002/PSSB.200844039.

99 P. Lecoq, Development of new scintillators for medical applications, *Nucl. Instrum. Methods Phys. Res., Sect. A*, 2016, **809**, 130–139, DOI: 10.1016/J.NIMA.2015.08.041.

100 G. Bizarri, W. W. Moses, S. A. Payne, and R. T. Williams, *Towards an understanding of nonlinearity in scintillator detector materials*, 2011, vol. 8142, pp. 223–233, DOI: 10.1117/12.896001.

101 W. W. Moses, S. A. Payne, W. S. Choong, G. Hull and B. W. Reutter, Scintillator non-proportionality: Present understanding and future challenges, *IEEE Trans. Nucl. Sci.*, 2008, **55**(3), 1049–1053, DOI: 10.1109/TNS.2008.922802.

102 W. W. Moses, *et al.*, The origins of scintillator non-proportionality, *IEEE Trans. Nucl. Sci.*, 2012, **59**(5), 2038–2044, DOI: 10.1109/TNS.2012.2186463.

103 J. C. Robertson and J. G. Lynch, The luminescent decay of various crystals for particles of different ionization density, *Proc. Phys. Soc.*, 1961, **77**(3), 751–756, DOI: 10.1088/0370-1328/77/3/326.

104 B. D. Rooney and J. D. Valentine, Scintillator light yield nonproportionality: Calculating photon response using measured electron response, *IEEE Trans. Nucl. Sci.*, 1997, **44**(3), 509–516, DOI: 10.1109/23.603702.

105 K. L. Giboni, Limited energy resolution in liquid argon due to δ-ray production, *Nucl. Instrum. Methods Phys. Res., Sect. A*, 1988, **269**(3), 554–559, DOI: 10.1016/0168-9002(88)90133-7.

106 S. A. Payne, Nonproportionality of Scintillator Detectors. IV. Resolution Contribution from Delta-Rays, *IEEE Trans. Nucl. Sci.*, 2015, **62**(1), 372–380, DOI: 10.1109/TNS.2014.2387256.

107 M. Moszyński, Energy resolution and non-proportionality of scintillation detectors – new observations, *Radiat. Meas.*, 2010, **45**(3–6), 372–376, DOI: 10.1016/J.RADMEAS.2009.10.012.

108 M. Balcerzyk, M. Moszyński, M. Kapusta, D. Wolski, T. Pawelke and C. L. Melcher, YSO, LSO, GSO and LGSO. A study of energy resolution and nonproportionality, *IEEE Trans. Nucl. Sci.*, 2000, **47**(4), 1319–1323, DOI: 10.1109/23.872971.

109 D. T. Wakeford, S. R. Torngа, J. C. Adams, O. C. Trautschold and M. P. Hehlen, Improved Scintillation Detector Performance *via* a Method of Enhanced Layered Coatings, *IEEE Trans. Nucl. Sci.*, 2017, **64**(7), 1704–1708, DOI: 10.1109/TNS.2016.2628041.

110 W. Ye, G. Bizarri, M. D. Birowosuto and L. J. Wong, Enhancing Large-Area Scintillator Detection with Photonic Crystal Cavities, *ACS Photonics*, 2022, **9**(12), 3917–3925, DOI: 10.1021/ACSPHOTONICS.2C01235.

111 P. Singh, G. Dosovitskiy and Y. Bekenstein, Bright Innovations: Review of Next-Generation Advances in Scintillator Engineering, *ACS Nano*, 2024, **18**(22), 14029–14049, DOI: 10.1021/ACSNANO.3C12381/ASSET/IMAGES/LARGE/NN3C12381_0004.

112 A. R. Knapitsch, *Photonic Crystals: Enhancing the Light Output of Scintillation Based Detectors*, accessed: Dec. 22, 2024, available: https://cds.cern.ch/record/1528566.

113 B. Singh, *et al.*, Enhanced Scintillation Light Extraction Using Nanoimprinted Photonic Crystals, *IEEE Trans. Nucl. Sci.*, 2018, **65**(4), 1059–1065, DOI: 10.1109/TNS.2018.2811646.

114 M. Moszyński, Inorganic scintillation detectors in γ-ray spectrometry, *Nucl. Instrum. Methods Phys. Res., Sect. A*, 2003, **505**(1–2), 101–110, DOI: 10.1016/S0168-9002(03)01030-1.

115 P. Dorenbos, J. T. D. de Haas and C. W. V. van Eijk, Non-Proportionality in the Scintillation Response and the Energy Resolution Obtainable with Scintillation Crystals, *IEEE Trans. Nucl. Sci.*, 1995, **42**(6), 2190–2202, DOI: 10.1109/23.489415.

116 P. A. Rodnyi, P. Dorenbos and C. W. E. van Eijk, Energy Loss in Inorganic Scintillators, *Phys. Status Solidi B*, 1995, **187**(1), 15–29, DOI: 10.1002/PSSB.2221870102.

117 J. Singh and A. Koblov, Role of nonlinear excitation quenching processes and carrier diffusion on the nonproportionality of light yield in scintillators, *IEEE Trans. Nucl. Sci.*, 2012, **59**, 2045–2051, DOI: 10.1109/TNS.2012.2212284.

118 S. E. Derenzo, M. J. Weber, E. Bourret-Courchesne and M. K. Klintenberg, The quest for the ideal inorganic scintillator, *Nucl. Instrum. Methods Phys. Res., Sect. A*, 2003, **505**(1–2), 111–117, DOI: 10.1016/S0168-9002(03)01031-3.

119 L. Lu, M. Sun, T. Wu, Q. Lu, B. Chen and B. Huang, All-inorganic perovskite nanocrystals: next-generation

scintillation materials for high-resolution X-ray imaging, *Nanoscale Adv.*, 2022, **4**(3), 680–696, DOI: 10.1039/D1NA00815C.

120 Z. Zhang and G. Yang, Recent advancements in using perovskite single crystals for gamma-ray detection, *J. Mater. Sci.: Mater. Electron.*, 2021, **32**(10), 12758–12770, DOI: 10.1007/S10854-020-03519-Z/METRICS.

121 G. Knoll, *Radiation detection and measurement*, 2010.

122 P. Dorenbos, Energy of the first 4f7 → 4f65d transition of Eu2+ in inorganic compounds, *J. Lumin.*, 2003, **104**(4), 239–260, DOI: 10.1016/S0022-2313(03)00078-4.

123 T. Yanagida, G. Okada, T. Kato, D. Nakauchi and S. Yanagida, Fast and high light yield scintillation in the Ga_2O_3 semiconductor material, *Appl. Phys. Express*, 2016, **9**(4), 042601, DOI: 10.7567/APEX.9.042601.

124 T. Yanagida and Y. Fujimoto, Evaluation of scintillation properties of GaN, *J. Surf. Sci. Nanotechnol.*, 2014, **23**, 396–399, DOI: 10.1380/ejssnt.2014.396.

125 T. Yanagida, *et al.*, Optical and scintillation properties of bulk ZnO crystal, *Phys. Status Solidi C*, 2012, **9**(12), 2284–2287, DOI: 10.1002/PSSC.201200176.

126 T. Yanagida, *et al.*, Ce-doped LiF–SrF2 eutectic scintillators for thermal neutron detection produced at different solidification rates, *Opt. Mater.*, 2013, **35**(7), 1449–1454, DOI: 10.1016/j.optmat.2013.02.016.

127 T. Yanagida, *et al.*, Scintillation properties of LiF–SrF2 and LiF–CaF2 eutectic, *J. Lumin.*, 2013, **144**, 212–216, DOI: 10.1016/J.JLUMIN.2013.07.016.

128 V. B. Mikhailik, H. Kraus, J. Imber and D. Wahl, Scintillation properties of pure CaF2, *Nucl. Instrum. Methods Phys. Res., Sect. A*, 2006, **566**(2), 522–525, DOI: 10.1016/J.NIMA.2006.06.063.

129 R. Y. Shendrik, E. A. Radzhabov and A. I. Nepomnyashchikh, Scintillation properties of SrF2 and SrF2-Ce3+ crystals, *Tech. Phys. Lett.*, 2013, **39**(7), 587–590, DOI: 10.1134/S1063785013070109/METRICS.

130 M. Laval, *et al.*, Barium fluoride — Inorganic scintillator for subnanosecond timing, *Nucl. Instrum. Methods Phys. Res.*, 1983, **206**(1–2), 169–176, DOI: 10.1016/0167-5087(83)91254-1.

131 M. Moszyński, R. Allemand, M. Laval, R. Odru and J. Vacher, Recent progress in fast timing with CsF scintillators in application to time-of-flight positron tomography in medicine, *Nucl. Instrum. Methods Phys. Res.*, 1983, **205**(1–2), 239–249, DOI: 10.1016/0167-5087(83)90194-1.

132 N. Yahaba, *et al.*, X-ray detection capability of a Cs2ZnCl4 single-crystal scintillator, *Appl. Phys. Express*, 2014, **7**(6), 062602, DOI: 10.7567/APEX.7.062602.

133 M. Itoh and M. Kamada, *Comparative Study of Auger-Free Luminescence and Valence-Band Photoemission in Wide-Gap Materials*, 2013, vol. 70, pp. 3446–3451, DOI: 10.1143/JPSJ.70.3446.

134 T. Yanagida, Y. Fujimoto, M. Koshimizu and K. Fukuda, Scintillation properties of CdF2 crystal, *J. Lumin.*, 2015, **157**, 293–296, DOI: 10.1016/J.JLUMIN.2014.09.013.

135 P. Schotanus, C. W. E. van Eijk, R. W. Hollander and J. Pijpelink, Temperature dependence of BaF2 scintillation light yield, *Nucl. Instrum. Methods Phys. Res., Sect. A*, 1985, **238**(2–3), 564–565, DOI: 10.1016/0168-9002(85)90503-0.

136 M. J. Weber and R. R. Monchamp, Luminescence of Bi4 Ge3 O12 : spectral and decay properties, *J. Appl. Phys.*, 1973, **44**(12), 5495–5499, DOI: 10.1063/1.1662183.

137 W. Gong, Y. Wu, R. Zhang and M. G.-E.- Calphad, *Phase Equilibrium in Lanthanide Halide Systems: Assessment of CeBr3 and MBr–CeBr3 Systems (M= Li, Na, K, Rb, Cs)*, Elsevier, 2012, vol. 36, pp. 44–51, DOI: 10.1016/j.calphad.2011.11.001.

138 R. Hawrami, E. Ariesanti, H. Wei, J. Finkelstein, J. Glodo and K. S. Shah, Intrinsic scintillators: $TlMgCl_3$ and $TlCaI_3$, *J. Cryst. Growth*, 2017, **475**, 216–219, DOI: 10.1016/J.JCRYSGRO.2017.06.012.

139 Y. Futami, T. Yanagida and Y. Fujimoto, Optical, dosimetric, and scintillation properties of pure sapphire crystals, *Jpn. J. Appl. Phys.*, 2014, **53**(2S), 02BC12, DOI: 10.7567/JJAP.53.02BC12.

140 T. Kato, G. Okada and T. Yanagida, Optical, scintillation and dosimeter properties of MgO transparent ceramic and single crystal, *Ceram. Int.*, 2016, **42**(5), 5617–5622, DOI: 10.1016/J.CERAMINT.2015.12.070.

141 M. Ishida, A. Watanabe, H. Kawamoto, Y. Fujimoto and K. Asai, Tl 2 NaScCl 6 : A New Tl-based Elpasolite Crystalline Scintillator, *Sens. Mater.*, 2025, **37**(2), 607–616, DOI: 10.18494/SAM5482.

142 N. Channappa and B. R. Kerur, Standardization of gamma-ray spectrometry using the NaI (TI) scintillation detector, *J. Radioanal. Nucl. Chem.*, 2025, 1–6, DOI: 10.1007/S10967-024-09648-7/METRICS.

143 Y. Tariwong, *et al.*, Ca co-doped CsI(Tl) crystal scintillator for γ- and X-ray detecting applications, *Radiat. Phys. Chem.*, 2025, **226**, 112241, DOI: 10.1016/J.RADPHYSCHEM.2024.112241.

144 A. Gonzalez-Montoro, S. Pourashraf, J. W. Cates and C. S. Levin, Cherenkov Radiation-Based Coincidence Time Resolution Measurements in BGO Scintillators, *Front. Phys.*, 2022, **10**(1), 816384, DOI: 10.3389/fphy.2022.816384.

145 T. Kato, G. Okada and T. Yanagida, Optical, scintillation and dosimeter properties of MgO transparent ceramic doped with Mn2+, *J. Ceram. Soc. Jpn.*, 2016, **124**(5), 559–563, DOI: 10.2109/JCERSJ2.15229.

146 Y. Wang, M. Li, Z. Chai, Y. Wang and S. Wang, Perovskite Scintillators for Improved X-ray Detection and Imaging, *Angew. Chem., Int. Ed.*, 2023, **62**(38), e202304638, DOI: 10.1002/ANIE.202304638.

147 I. Seferis, *et al.*, Light emission efficiency and imaging performance of Lu2O3:Eu nanophosphor under X-ray radiography conditions: Comparison with Gd2O2S:Eu, *J. Lumin.*, 2014, **151**, 229–234, DOI: 10.1016/J.JLUMIN.2014.02.017.

148 Y. Fujimoto, Optical and Near-Infrared Scintillation Properties of Nd3+-Doped YVO4 Crystals, *Sens. Mater.*, 2016, **28**(8), 857–861, DOI: 10.18494/SAM.2016.1352.

149 T. Yanagida, Y. Fujimoto, H. Yagi and T. Yanagitani, Optical and scintillation properties of transparent ceramic Yb:Lu2O3 with different Yb concentrations, *Opt. Mater.*, 2014, **36**(6), 1044–1048, DOI: **10.1016/J.OPTMAT.2014.01.022**.

150 M. M. Moszyński *et al.*, CdWO/sub 4/crystal in gamma-ray spectrometry, *IEEE Symposium Conference Record Nuclear Science 2004*, 2005, vol. 52, 6, DOI: **10.1109/TNS.2005.855704**.

151 S. L. Fritz and L. T. Cook, High resolution digital x ray detector utilizing a discrete array of CdWO4 scintillators and a self scanned photodiode array, *Med. Phys.*, 1987, **14**(2), 244–248, DOI: **10.1118/1.596077**.

152 J. Czochralski, Ein neues Verfahren zur Messung der Kristallisationsgeschwindigkeit der Metalle, *Z. Phys. Chem.*, 1918, **92U**(1), 219–221, DOI: **10.1515/ZPCH-1918-9212**.

153 S. Dagdale, V. Pahurkar and G. Muley, High Temperature Crystal Growth: An Overview, *Macromol. Symp.*, 2016, **362**(1), 139–141, DOI: **10.1002/MASY.201400254**.

154 R. Zheng, L. Wang, Y. Liu, J. Chen, P. Xiao and Q. Xie, Scintillation properties of Cs3Cu2I5:Tl crystals grown by Cz, EFG and Bridgman methods with a multifunctional melt growth furnace, *J. Cryst. Growth*, 2024, **627**, 127512, DOI: **10.1016/J.JCRYSGRO.2023.127512**.

155 V. B. Mykhaylyk, *et al.*, Bright and fast scintillations of an inorganic halide perovskite CsPbBr3 crystal at cryogenic temperatures, *Sci. Rep.*, 2020, **10**(1), 1–11, DOI: **10.1038/s41598-020-65672-z**.

156 Y. Yin, *et al.*, Controllable and directional growth of Er:Lu 2 O 3 single crystals by the edge-defined film-fed technique, *CrystEngComm*, 2020, **22**(39), 6569–6573, DOI: **10.1039/D0CE00855A**.

157 V. V. Kochurikhin, M. A. Ivanov, W. S. Yang, S. J. Suh and D. H. Yoon, Development of edge-defined film-fed growth for the production of YVO4 single crystals with various shapes, *J. Cryst. Growth*, 2001, **229**(1–4), 179–183, DOI: **10.1016/S0022-0248(01)01116-2**.

158 G. Calvert, C. Guguschev, A. Burger, M. Groza, J. J. Derby and R. S. Feigelson, High speed growth of SrI2 scintillator crystals by the EFG process, *J. Cryst. Growth*, 2016, **455**, 143–151, DOI: **10.1016/J.JCRYSGRO.2016.10.024**.

159 K. Ichiba, *et al.*, Evaluation of photoluminescence and scintillation properties of Eu-doped YVO4 single crystals synthesized by optical floating zone method, *J. Lumin.*, 2024, **266**, 120327, DOI: **10.1016/J.JLUMIN.2023.120327**.

160 Y. Liu, A. Magrez, D. Wen, H. Bi and N. Kikugawa, Recent Progress of Floating-Zone Techniques for Bulk Single-Crystal Growth, *Crystals*, 2024, **14**(6), 552, DOI: **10.3390/CRYST14060552**.

161 T. Ito, Y. Tomioka, F. Rackerseder, M. Traub and D. Hoffmann, Growth of β-Ga2O3 crystal with a diameter of 30 mm by laser-diode-heated floating zone (LDFZ) method, *J. Cryst. Growth*, 2024, **634**, 127673, DOI: **10.1016/J.JCRYSGRO.2024.127673**.

162 R. Takahashi, K. Okazaki, D. Nakauchi, T. Kato, N. Kawaguchi and T. Yanagida, Optical and scintillation properties of Tm-doped Ca3TaGa3Si2O14 single crystals, *J. Mater. Sci.: Mater. Electron.*, 2024, **35**(34), 1–9, DOI: **10.1007/S10854-024-13907-4**.

163 Y. Endo, *et al.*, Improvement of scintillation light yield of Tb:CaHfO3 by Mg-substitution, *Opt. Mater.*, 2024, **152**, 115524, DOI: **10.1016/J.OPTMAT.2024.115524**.

164 Y. Endo, *et al.*, Development of Dy-doped CaHfO3 single crystal scintillator for X-ray detectors, *Opt. Mater.*, 2024, **157**, 116276, DOI: **10.1016/J.OPTMAT.2024.116276**.

165 W. Yuan, *et al.*, In Situ Regulating the Order–Disorder Phase Transition in Cs2AgBiBr6 Single Crystal toward the Application in an X-Ray Detector, *Adv. Funct. Mater.*, 2019, **29**(20), 1900234, DOI: **10.1002/ADFM.201900234**.

166 W. Guo, *et al.*, Room-Temperature Ferroelectric Material Composed of a Two-Dimensional Metal Halide Double Perovskite for X-ray Detection, *Angew. Chem., Int. Ed.*, 2020, **59**(33), 13879–13884, DOI: **10.1002/ANIE.202004235**.

167 H. Wei, *et al.*, Sensitive X-ray detectors made of methylammonium lead tribromide perovskite single crystals, *Nat. Photonics*, 2016, **10**(5), 333–339, DOI: **10.1038/nphoton.2016.41**.

168 C. C. Stoumpos, *et al.*, Crystal growth of the perovskite semiconductor CsPbBr3: a new material for high-energy radiation detection, *Cryst. Growth Des.*, 2013, **13**(7), 2722–2727, DOI: **10.1021/CG400645T**.

169 R. Hofstadter, Alkali Halide Scintillation Counters, *Phys. Rev.*, 1948, **74**(1), 100–101, DOI: **10.1103/PhysRev.74.100**.

170 R. Hawrami, E. Ariesanti, A. Farsoni, D. Szydel and H. Sabet, Growth and Evaluation of Improved CsI:Tl and NaI:Tl Scintillators, *Crystals 2022*, 2022, **12**(11), 1517, DOI: **10.3390/CRYST12111517**.

171 E. M. Becker and A. T. Farsoni, Wireless, low-cost, FPGA-based miniature gamma ray spectrometer, *Nucl. Instrum. Methods Phys. Res., Sect. A*, 2014, **761**, 99–104, DOI: **10.1016/J.NIMA.2014.05.096**.

172 M. Gascón, H. Álvarez-Pol, J. Benlliure, E. Casarejos, D. Cortina-Gil and I. Durán, Optimization of energy resolution obtained with CsI(Tl) crystals for the R3B calorimeter, *IEEE Trans. Nucl. Sci.*, 2008, **55**(3), 1259–1262, DOI: **10.1109/TNS.2008.922808**.

173 E. Sakai, Recent measurements on scintillator-photodetector systems, *IEEE Trans. Nucl. Sci.*, 1987, **34**(1), 418–422, DOI: **10.1109/TNS.1987.4337375**.

174 K. Yang and P. R. Menge, Improving γ-ray energy resolution, non-proportionality, and decay time of NaI:Tl+ with Sr^{2+} and Ca^{2+} co-doping, *J. Appl. Phys.*, 2015, **118**(21), 213106, DOI: **10.1063/1.4937126**.

175 M. Sonu, K. Tyagi, A. K. Singh, N. S. Rawat and P. S. Sarkar, Improvement of Performance Characteristics for LiI:Ag Single-Crystal Scintillators by Defect Structure Tailoring Using Sr Codopant, *Phys. Status Solidi A*, 2021, **219**(1), 1–8, DOI: **10.1002/PSSA.202100465**.

176 K. Miyazaki, D. Nakauchi, T. Kato, N. Kawaguchi and T. Yanagida, Development of Tl-doped KI single crystal scintillators, *Radiat. Phys. Chem.*, 2023, **207**(6), 110820, DOI: **10.1016/J.RADPHYSCHEM.2023.110820**.

177 K. Miyazaki, D. Nakauchi, T. Kato, N. Kawaguchi and T. Yanagida, Scintillation Properties of Eu-doped KI Single Crystals, *Sens. Mater.*, 2024, **36**(2), 515–522, DOI: 10.18494/SAM4756.

178 P. R. Beck, *et al.*, Strontium iodide instrument development for gamma spectroscopy and radioisotope identification, *Optics & Photonics – Optical Engineering Applications*, 2014, vol. 9213, p. 92130N, DOI: 10.1117/12.2063056.

179 C. M. Wilson *et al.*, *Strontium Iodide Scintillators for High Energy Resolution Gamma Ray Spectroscopy*, vol. 7079, pp. 334–340, 2008, DOI: 10.1117/12.806291.

180 N. Cherepy, *et al.*, Prospects for High Energy Resolution Gamma Ray Spectroscopy with Europium-Doped Strontium Iodide, *MRS Proc.*, 2009, **1164**, 179–184, DOI: 10.1557/PROC-1164-L11-04.

181 U. Shirwadkar, R. Hawrami, J. Glodo, E. V. D. Van Loef and K. S. Shah, Promising alkaline earth halide scintillators for gamma-ray spectroscopy, *IEEE Trans. Nucl. Sci.*, 2013, **60**(2), 1011–1015, DOI: 10.1109/TNS.2013.2240696.

182 T. Iida, K. Kamada, M. Yoshino, K. J. Kim, K. Ichimura and A. Yoshikawa, High-light-yield calcium iodide (CaI_2) scintillator for astroparticle physics, *Nucl. Instrum. Methods Phys. Res., Sect. A*, 2019, **958**(4), 162629, DOI: 10.1016/J.NIMA.2019.162629.

183 N. J. Cherepy *et al.*, Barium iodide single-crystal scintillator detectors, *SPIE Optical Engineering Applications*, 2007, vol. 6706, p. 670616, DOI: 10.1117/12.738973.

184 V. Vasylkovskyi, I. Bespalova, M. Slipchenko, O. Slipchenko, Y. Zholudov and B. Chichkov, Review: Electrochemiluminescence of Perovskite-Related Nanostructures, *Crystals*, 2023, **13**(3), 455, DOI: 10.3390/CRYST13030455.

185 J. Shamsi, A. S. Urban, M. Imran, L. De Trizio and L. Manna, Metal Halide Perovskite Nanocrystals: Synthesis, Post-Synthesis Modifications, and Their Optical Properties, *Chem. Rev.*, 2019, **119**(5), 3296–3348, DOI: 10.1021/ACS.CHEMREV.8B00644/ASSET/IMAGES/MEDIUM/CR-2018-00644B_0057.

186 M. A. K. Sheikh, *et al.*, Solution-Processable A2XY4 (A = PEA, BA; X = Pb, Sn, Cu, Mn; Y = Cl, Br, I) Crystals for High Light Yield and Ultrafast Scintillators, *IEEE Trans. Nucl. Sci.*, 2023, **70**(7), 1384–1391, DOI: 10.1109/TNS.2023.3267636.

187 S. González-Carrero, R. E. Galian and J. Pérez-Prieto, Organometal Halide Perovskites: Bulk Low-Dimension Materials and Nanoparticles, *Part. Part. Syst. Charact.*, 2015, **32**(7), 709–720, DOI: 10.1002/PPSC.201400214.

188 N. V. Rebrova, *et al.*, Effects of europium concentration on luminescent and scintillation performance of Cs0.2Rb0.8Ca1−xEuxBr3 ($0 \leq x \leq 0.08$) crystals, *J. Rare Earths*, 2022, **40**(1), 29–33, DOI: 10.1016/J.JRE.2020.08.012.

189 A. C. Lindsey, M. Zhuravleva, L. Stand, Y. Wu and C. L. Melcher, Crystal growth and characterization of europium doped KCaI3, a high light yield scintillator, *Opt. Mater.*, 2015, **48**, 1–6, DOI: 10.1016/J.OPTMAT.2015.07.017.

190 Y. Wu, *et al.*, Scintillation properties of a 2-inch diameter KCa0.8Sr0.2I3:Eu^{2+} single crystal, *Nucl. Instrum. Methods Phys. Res., Sect. A*, 2017, **866**, 13–17, DOI: 10.1016/J.NIMA.2017.05.053.

191 K. S. Pestovich, *et al.*, Intrinsic scintillation performance & europium concentration effects in $RbSr_2I_5$ and $RbSr_2Br_5$ scintillators, *J. Cryst. Growth*, 2025, **649**, 127924, DOI: 10.1016/J.JCRYSGRO.2024.127924.

192 L. Soundara-Pandian, R. Hawrami, J. Glodo, E. Ariesanti, E. V. Van Loef and K. Shah, Lithium Alkaline Halides - Next Generation of Dual Mode Scintillators, *IEEE Trans. Nucl. Sci.*, 2016, **63**(2), 490–496, DOI: 10.1109/TNS.2016.2535355.

193 L. Stand, M. Zhuravleva, H. Wei and C. L. Melcher, Crystal growth and scintillation properties of potassium strontium bromide, *Opt. Mater.*, 2015, **46**, 59–63, DOI: 10.1016/J.OPTMAT.2015.04.002.

194 L. Stand, *et al.*, Exploring growth conditions and Eu^{2+} concentration effects for KSr2I5:Eu scintillator crystals II: Ø 25 mm crystals, *J. Cryst. Growth*, 2018, **483**, 301–307, DOI: 10.1016/J.JCRYSGRO.2017.11.010.

195 X. Wen, *et al.*, Scintillator-oriented near-infrared emitting Cs4SrI6:Yb^{2+}, Sm^{2+} single crystals *via* sensitization strategy, *J. Am. Ceram. Soc.*, 2023, **106**(11), 6762–6768, DOI: 10.1111/JACE.19302.

196 D. Rutstrom, L. Stand, B. Dryzhakov, M. Koschan, C. L. Melcher and M. Zhuravleva, Crystal growth and scintillation properties of new ytterbium-activated scintillators Cs4CaI6:Yb and Cs4SrI6:Yb, *Opt. Mater.*, 2020, **110**, 110536, DOI: 10.1016/J.OPTMAT.2020.110536.

197 Y. Wu, *et al.*, Zero-dimensional Cs4EuX6 (X = Br, I) all-inorganic perovskite single crystals for gamma-ray spectroscopy, *J. Mater. Chem. C*, 2018, **6**(25), 6647–6655, DOI: 10.1039/C8TC01458B.

198 L. Stand, M. Zhuravleva, B. Chakoumakos, J. Johnson, A. Lindsey and C. Melcher, Scintillation properties of Eu2+-doped KBa2I5 and K2BaI4, *J. Lumin.*, 2016, **169**, 301–307, DOI: 10.1016/J.JLUMIN.2015.09.013.

199 F. Moretti, D. Onken, D. Perrodin and E. Bourret, Investigation of the competition between Tl^+ and Ce^{3+} scintillation in Tl2LiYCl6:Ce, an elpasolite scintillator, *J. Lumin.*, 2022, **241**, 118549, DOI: 10.1016/J.JLUMIN.2021.118549.

200 R. Hawrami, E. Ariesanti, A. Burger and P. Sellin, Latest growth of large diameter Tl-based elpasolite scintillation crystals, *Opt. Mater.*, 2022, **128**, 112324, DOI: 10.1016/J.OPTMAT.2022.112324.

201 Q. Ou, *et al.*, Band structure engineering in metal halide perovskite nanostructures for optoelectronic applications, *Nano Mater. Sci.*, 2019, **1**(4), 268–287, DOI: 10.1016/J.NANOMS.2019.10.004.

202 J. M. Hoffman, *et al.*, From 2D to 1D Electronic Dimensionality in Halide Perovskites with Stepped and Flat Layers Using Propylammonium as a Spacer, *J. Am. Chem. Soc.*, 2019, **141**(27), 10661–10676, DOI: 10.1021/JACS.9B02846.

203 R. F. Kahwagi, S. T. Thornton, B. Smith and G. I. Koleilat, Dimensionality engineering of metal halide perovskites, *Front. Optoelectron.*, 2020, **13**(3), 196–224, DOI: 10.1007/S12200-020-1039-6/METRICS.

204 K. Yang, M. Zhuravleva and C. L. Melcher, Crystal growth and characterization of CsSr1–xEux I3 high light yield scintillators, *Phys. Status Solidi RRL*, 2011, **5**(1), 43–45, DOI: 10.1002/PSSR.201004434.

205 K. Mizoi, Y. Fujimoto, D. Nakauchi, M. Koshimizu, T. Yanagida and K. Asai, Evaluation of photoluminescence and scintillation properties of Yb^{2+}-doped CsMX3 (M = Ca, Sr; X = Cl, Br) crystals, *J. Lumin.*, 2022, **245**, 118797, DOI: 10.1016/J.JLUMIN.2022.118797.

206 L. Stand, *et al.*, Characterization of mixed halide scintillators: CsSrBrI2:Eu, CsCaBrI2:Eu and CsSrClBr2:Eu, *J. Lumin.*, 2019, **207**, 70–77, DOI: 10.1016/J.JLUMIN.2018.10.108.

207 K. Yang, M. Zhuravleva, H. Rothfuss, and C. L. Melcher, *Optical and Scintillation Properties of Single Crystal CsSr 1xEuxI3*, IEEE Nuclear Science Symposium Conference Record, 2010, pp. 1603–1606, DOI: 10.1109/NSSMIC.2010.5874046.

208 Y. Wu, *et al.*, Toward High Energy Resolution in $CsSrI_3/Eu^{2+}$ Scintillating Crystals: Effects of Off-Stoichiometry and Eu^{2+} Concentration, *Cryst. Growth Des.*, 2016, **16**(12), 7186–7193, DOI: 10.1021/ACS.CGD.6B01375/ASSET/IMAGES/MEDIUM/CG-2016-01375N_0014.

209 U. Shirwadkar, E. V. D. Van Loef, R. Hawrami, S. Mukhopadhyay, J. Glodo and K. S. Shah, *New Promising Scintillators for Gamma-Ray Spectroscopy: Cs(Ba,Sr)(Br,I)3*, IEEE Nuclear Science Symposium Conference Record, 2011, pp. 1583–1585, DOI: 10.1109/NSSMIC.2011.6154636.

210 M. Zhuravleva, *et al.*, *High Energy Resolution Scintillators for Nuclear Nonproliferation Applications*, 2014, vol. 9213, pp. 7–18, DOI: 10.1117/12.2064191.

211 M. Loyd, *et al.*, Growth of large size (≥38 mm diameter) KCaI3:Eu scintillator crystals, *Nucl. Instrum. Methods Phys. Res., Sect. A*, 2019, **914**, 8–14, DOI: 10.1016/J.NIMA.2018.10.105.

212 S. S. Gokhale, L. Stand, A. Lindsey, M. Koschan, M. Zhuravleva and C. L. Melcher, Improvement in the optical quality and energy resolution of CsSrBr3: Eu scintillator crystals, *J. Cryst. Growth*, 2016, **445**, 1–8, DOI: 10.1016/J.JCRYSGRO.2016.04.006.

213 S. S. Gokhale, *et al.*, Investigation of the unique degradation phenomenon observed in CsSrBr3: Eu 5% scintillator crystals, *J. Cryst. Growth*, 2016, **452**, 89–94, DOI: 10.1016/J.JCRYSGRO.2016.03.003.

214 Y. Fujimoto, K. Saeki, D. Nakauchi, T. Yanagida, M. Koshimizu and K. Asai, Characterization of CsSrCl3:Ce crystalline scintillator, *Sens. Mater.*, 2017, **29**(10), 1425–1430, DOI: 10.18494/SAM.2017.1622.

215 Y. Wu, *et al.*, Quaternary Iodide $K(Ca,Sr)I3:Eu^{2+}$ Single-Crystal Scintillators for Radiation Detection: Crystal Structure, Electronic Structure, and Optical and Scintillation Properties, *Adv. Opt. Mater.*, 2016, **4**(10), 1518–1532, DOI: 10.1002/ADOM.201600239.

216 Q. Xu, *et al.*, Bulk Organic–Inorganic Methylammonium Lead Halide Perovskite Single Crystals for Indirect Gamma Ray Detection, *ACS Appl. Mater. Interfaces*, 2019, **11**(50), 47485–47490, DOI: 10.1021/ACSAMI.9B10367/ASSET/IMAGES/MEDIUM/AM9B10367_0005.

217 Y. Fujimoto, M. Koshimizu, T. Yanagida, G. Okada, K. Saeki and K. Asai, Thallium magnesium chloride: a high light yield, large effective atomic number, intrinsically activated crystalline scintillator for X-ray and gamma-ray detection, *Jpn. J. Appl. Phys.*, 2016, **55**(9), 090301, DOI: 10.7567/JJAP.55.090301/XML.

218 A. Khan, G. Rooh, H. J. Kim, H. Park and S. Kim, Intrinsically activated TlCaCl3: a new halide scintillator for radiation detection, *Radiat. Meas.*, 2017, **107**, 115–118, DOI: 10.1016/J.RADMEAS.2017.09.003.

219 G. Bizarri, E. D. Bourret-Courchesne, Z. Yan and S. E. Derenzo, Scintillation and optical properties of BaBrI: Eu^{2+} and CsBa 2I 5: Eu^{2+}, *IEEE Trans. Nucl. Sci.*, 2011, **58**(6), 3403–3410, DOI: 10.1109/TNS.2011.2166999.

220 M. Arai, Y. Fujimoto, M. Koshimizu, T. Yanagida and K. Asai, Scintillation and photoluminescence properties of (Tl1−xAx)MgCl3 (where A = alkali metal), *J. Alloys Compd.*, 2020, **823**, 153871, DOI: 10.1016/J.JALLCOM.2020.153871.

221 W. Wolszczak, K. W. Krämer and P. Dorenbos, $CsBa2I5:Eu^{2+},Sm^{2+}$—The First High-Energy Resolution Black Scintillator for γ-Ray Spectroscopy, *Phys. Status Solidi RRL*, 2019, **13**(9), 1900158, DOI: 10.1002/PSSR.201900158.

222 L. Stand, M. Zhuravleva, A. Lindsey and C. L. Melcher, Growth and characterization of potassium strontium iodide: a new high light yield scintillator with 2.4% energy resolution, *Nucl. Instrum. Methods Phys. Res., Sect. A*, 2015, **780**, 40–44, DOI: 10.1016/J.NIMA.2015.01.052.

223 N. V. Rebrova, A. Y. Grippa, R. Calà, L. Martinazzoli, E. Auffray and I. A. Boiaryntseva, Growth and luminescent properties of new Eu^{2+} doped RbBa2I5 scintillator, *Nucl. Instrum. Methods Phys. Res., Sect. A*, 2020, **978**, 164463, DOI: 10.1016/J.NIMA.2020.164463.

224 A. Raja, *et al.*, Growth difficulties and growth of crack free Eu2+ activated KSr2I5 scintillator single crystal by vertical bridgman-stockbarger technique for radiation detection applications, *Results Chem.*, 2024, **7**, 101346, DOI: 10.1016/J.RECHEM.2024.101346.

225 R. Borade, E. Bourret-Courchesne and S. Derenzo, Scintillation properties of $CsBa2Br5:Eu^{2+}$, *Nucl. Instrum. Methods Phys. Res., Sect. A*, 2011, **652**(1), 260–263, DOI: 10.1016/J.NIMA.2010.08.093.

226 G. Bizarri, E. D. Bourret-Courchesne, Z. Yan and S. E. Derenzo, Scintillation and optical properties of BaBrI: Eu^{2+} and CsBa 2I 5: Eu^{2+}, *IEEE Trans. Nucl. Sci.*, 2011, **58**(6), 3403–3410, DOI: 10.1109/TNS.2011.2166999.

227 L. Stand, *et al.*, Crystal Growth and Scintillation Properties of Eu^{2+} doped Cs4CaI6 and Cs4SrI6, *J. Cryst. Growth*, 2018, **486**, 162–168, DOI: 10.1016/J.JCRYSGRO.2018.01.017.

228 L. Stand, M. Zhuravleva, B. Chakoumakos, J. Johnson, A. Lindsey and C. Melcher, Scintillation properties of

Eu^{2+}-doped KBa2I5 and K2BaI4, *J. Lumin.*, 2016, **169**, 301–307, DOI: 10.1016/J.JLUMIN.2015.09.013.

229 J. Glodo, E. V. D. Van Loef, W. M. Higgins and K. S. Shah, Scintillation properties of Cs2NaLaI6:Ce, *IEEE Nucl. Sci. Symp. Conf. Rec.*, 2006, **2**, 1208–1211, DOI: 10.1109/NSSMIC.2006.356061.

230 H. J. Kim, G. Rooh, H. Park and S. Kim, Luminescence and scintillation properties of the new Ce-doped Tl2LiGdCl6 single crystals, *J. Lumin.*, 2015, **164**, 86–89, DOI: 10.1016/J.JLUMIN.2015.03.026.

231 H. J. Kim, G. Rooh, H. Park and S. Kim, Investigations of scintillation characterization of Ce-activated Tl2LiGdBr6 single crystal, *Radiat. Meas.*, 2016, **90**, 279–281, DOI: 10.1016/J.RADMEAS.2015.12.021.

232 R. Hawrami, E. Ariesanti, L. Soundara-Pandian, J. Glodo and K. S. Shah, Tl2LiYCl6:Ce: A New Elpasolite Scintillator, *IEEE Trans. Nucl. Sci.*, 2016, **63**(6), 2838–2841, DOI: 10.1109/TNS.2016.2627523.

233 M. Ishida, A. Watanabe, H. Kawamoto, Y. Fujimoto and K. Asai, Tl2NaScCl6: A New Tl-based Elpasolite Crystalline Scintillator, *Sens. Mater.*, 2025, **37**(2), 607, DOI: 10.18494/SAM5482.

234 M. Arai, *et al.*, Tl2NaYCl6: a new self-activated scintillator possessing an elpasolite structure, *J. Mater. Sci.: Mater. Electron.*, 2021, **32**(6), 7906–7912, DOI: 10.1007/S10854-021-05514-4/METRICS.

235 M. J. Kim, H. J. Kim, J. Y. Cho, A. Khan, D. J. Daniel and G. Rooh, Characterizations of a New Tl-based Elpasolite Scintillator: Tl2LiScCl6, *J. Korean Phys. Soc.*, 2020, **76**(8), 706–709, DOI: 10.3938/JKPS.76.706/METRICS.

236 J. Jang, G. Rooh, S. Kim and H. J. Kim, Scintillation characterization of the pure Tl2LiGdBr6 single crystal, *Jpn. J. Appl. Phys.*, 2018, **57**(5), 052601, DOI: 10.7567/JJAP.57.052601.

237 H. J. Kim, G. Rooh, H. Park and S. Kim, Tl2LiYCl6 (Ce^{3+}): New Tl-based Elpasolite Scintillation Material, *IEEE Trans. Nucl. Sci.*, 2016, **63**(2), 439–442, DOI: 10.1109/TNS.2016.2530822.

238 Md. J. Hossen, *et al.*, Recent progress on the efficiency and stability of lead-free Cs2AgBiBr6 double halide perovskite solar cells, *Phys. Scr.*, 2024, **100**(1), 012005, DOI: 10.1088/1402-4896/AD9B59.

239 X. Zhang, *et al.*, Recent progress on the efficiency and stability of lead-free Cs2AgBiBr6 double halide perovskite solar cells, *Phys. Scr.*, 2024, **100**(1), 012005, DOI: 10.1088/1402-4896/AD9B59.

240 I. N. Flerov, M. V. Gorev, K. S. Aleksandrov, A. Tressaud, J. Grannec and M. Couzi, Phase transitions in elpasolites (ordered perovskites), *Mater. Sci. Eng., R*, 1998, **24**(3), 81–151, DOI: 10.1016/S0927-796X(98)00015-1.

241 Q. Zhou, W. Li, J. Xiao, A. Li and X. Han, Low-Dimensional Metal Halide for High Performance Scintillators, *Adv. Funct. Mater.*, 2024, **34**(38), 2402902, DOI: 10.1002/ADFM.202402902.

242 L. Wang, H. Liu, Y. Zhang and O. F. Mohammed, Photoluminescence Origin of Zero-Dimensional Cs4PbBr6 Perovskite, *ACS Energy Lett.*, 2020, **5**(1), 87–99, DOI: 10.1021/ACSENERGYLETT.9B02275/ASSET/IMAGES/MEDIUM/NZ9B02275_0008.

243 Q. Zhou, W. Li, J. Xiao, A. Li and X. Han, Low-Dimensional Metal Halide for High Performance Scintillators, *Adv. Funct. Mater.*, 2024, **34**(38), 2402902, DOI: 10.1002/ADFM.202402902.

244 D. Rutstrom, L. Stand, M. Koschan, C. L. Melcher and M. Zhuravleva, Europium concentration effects on the scintillation properties of Cs4SrI6:Eu and Cs4CaI6:Eu single crystals for use in gamma spectroscopy, *J. Lumin.*, 2019, **216**, 116740, DOI: 10.1016/J.JLUMIN.2019.116740.

245 K. S. Pestovich, L. Stand, E. Van Loef, C. L. Melcher and M. Zhuravleva, Crystal Growth and Characterization of Europium-Doped Rubidium Calcium Bromide Scintillators, *IEEE Trans. Nucl. Sci.*, 2023, **70**(7), 1370–1377, DOI: 10.1109/TNS.2023.3280733.

246 Y. Wu, *et al.*, Quaternary Iodide K(Ca,Sr)I3:Eu2+ Single-Crystal Scintillators for Radiation Detection: Crystal Structure, Electronic Structure, and Optical and Scintillation Properties, *Adv. Opt. Mater.*, 2016, **4**(10), 1518–1532, DOI: 10.1002/ADOM.201600239;PAGEGROUP:STRING:PUBLICATION.

247 H. Wei, M. Zhuravleva, K. Yang, B. Blalock and C. L. Melcher, Effect of Ba substitution in CsSrI3:Eu^{2+}, *J. Cryst. Growth*, 2013, **384**, 27–32, DOI: 10.1016/J.JCRYSGRO.2013.09.007.

248 M. Lowdon, *et al.*, Evaluation of Scintillator Detection Materials for Application within Airborne Environmental Radiation Monitoring, *Sensors*, 2019, **19**(18), 3828, DOI: 10.3390/S19183828.

249 A. Syntfeld-Kazuch, *et al.*, *Performance of CsI(Na) Scintillators in γ-ray Spectrometry*, IEEE Nuclear Science Symposium Conference Record, 2009, pp. 1474–1479, DOI: 10.1109/NSSMIC.2009.5402295.

250 C. Wanarak, W. Chewpraditkul and A. Phunpueok, Light yield non-proportionality and energy resolution of $Lu_{1.95}Y_{0.05}SiO_5$:Ce and Lu_2SiO_5:Ce scintillation crystals, *Procedia Eng.*, 2012, **32**, 765–771, DOI: 10.1016/J.PROENG.2012.02.010.

251 L. Stand, M. Zhuravleva, A. Lindsey and C. L. Melcher, Growth and characterization of potassium strontium iodide: a new high light yield scintillator with 2.4% energy resolution, *Nucl. Instrum. Methods Phys. Res., Sect. A*, 2015, **780**, 40–44, DOI: 10.1016/J.NIMA.2015.01.052.

252 M. Moszyński, R. Allemand, M. Laval, R. Odru and J. Vacher, Recent progress in fast timing with CsF scintillators in application to time-of-flight positron tomography in medicine, *Nucl. Instrum. Methods Phys. Res.*, 1983, **205**(1–2), 239–249, DOI: 10.1016/0167-5087(83)90194-1.

253 M. Moszyński, *et al.*, Characterization of CaWO4 scintillator at room and liquid nitrogen temperatures, *Nucl. Instrum. Methods Phys. Res., Sect. A*, 2005, **553**(3), 578–591, DOI: 10.1016/J.NIMA.2005.07.052.

254 D. R. Kinloch, W. Novak, P. Raby and I. Toepke, New Developments in Cadmium Tungstate, *IEEE Trans. Nucl. Sci.*, 1994, **41**(4), 752–754, DOI: 10.1109/23.322800.

255 M. Zhuravleva, B. Blalock, K. Yang, M. Koschan and C. L. Melcher, New single crystal scintillators: CsCaCl3:Eu and CsCaI3:Eu, *J. Cryst. Growth*, 2012, **352**(1), 115–119, DOI: **10.1016/J.JCRYSGRO.2012.02.025**.

256 Y. He, *et al.*, CsPbBr3 perovskite detectors with 1.4% energy resolution for high-energy γ-rays, *Nat. Photonics*, 2020, **15**(1), 36–42, DOI: **10.1038/s41566-020-00727-1**.

257 B. A. VanDevender, *et al.*, High-purity germanium spectroscopy at rates in excess of 106 events/s, *IEEE Trans. Nucl. Sci.*, 2014, **61**(5), 2619–2627, DOI: **10.1109/TNS.2014.2357059**.

258 S. E. Létant and T. F. Wang, Semiconductor Quantum Dot Scintillation under γ-Ray Irradiation, *Nano Lett.*, 2006, **6**(12), 2877–2880, DOI: **10.1021/NL0620942**.

259 M. Makowski, *et al.*, Scaling Up Purcell-Enhanced Self-Assembled Nanoplasmonic Perovskite Scintillators into the Bulk Regime, *Adv. Mater.*, 2025, **37**(30), 2417874, DOI: **10.1002/ADMA.202417874**.